Planetary Atmospheres: Probing Structure through Millimeterwave Observations of Carbon Monoxide

Thesis by

Mark Andrew Gurwell

In Partial Fulfillment of the Requirements

for the Degree of

Doctor of Philosophy

California Institute of Technology

Pasadena, California

1996

(Defended July 21, 1995)

to Shannon, with all my love

Acknowledgments

As a senior astronomy major at the University of Washington, I signed up for a course in radio astronomy. The class was in hindsight not so difficult, but at the time I found myself incapable of understanding even the basic theory of interferometry. I disliked the topic so much that I dropped the class like a hot potato after six weeks, even though I needed the credits and would have to make them up through a High Energy Astrophysics course. Thus I was fated to become a planetary radio astronomer, using interferometry to gather the data that forms the basis of this thesis.

I have only my advisor, Professor Dewey Muhleman, to blame. I came to Caltech under the mistaken impression that I might look at pretty pictures of the surface of Mars and somehow make science out of it. Dewey informed me that I would instead look at pretty line to continuum CO spectra from the mesosphere of Venus and somehow make science out of it. In a hurry.

After it became clear that I would actually be doing this for my thesis, Dewey took me under his wing. Despite repeated pleas (at times only half-joking) for me to do something sensible and sell shoes (or lamps, or ANYTHING), he miscalculated and managed to infuse in me a tremendous urge to learn more about the planets, to learn as much as I could using the rapidly improving technology of millimeter astronomy. From him I learned that Muhleman is even rarer than Gurwell as a name, that the Athenaeum has good chowder on Fridays, and that should shooting rubber bands at hornets in the Millimeter Array control building ever become an Olympic sport, Dewey would be a two-time gold medal winner.

I will forever treasure working with him while a graduate student at Caltech. He taught me a lot about being a good scientist, but more about being a good person.

As for the rest of the Motley Crew, I would like to thank Professor Yuk Yung for providing me a haven from radio astronomy through our work on the D/H ratio on Venus. Special thanks to Andy Ingersoll and Peter Goldreich for participating in the morning basketball games, despite the horrid attrition rate due to injury (my back included). On the subject of basketball, thanks to the Seattle Supersonics for losing in the first round of the playoffs this year, allowing me ample time during the late spring to finish my thesis. World Championships can be so time-consuming.

I extend many thanks to the staff of the Owens Valley Radio Observatory for

all the help they have provided throughout the years. They were particularly helpful during the observations of Mars which required three moves of the array in 7 days. A monumental task that worked out well. I also express my gratitude to Dave Koerner who operated the array during that week and helped me to learn how to use it myself, and to Glenn Berge for his dry humor that made the worst parts bearable.

Big huge cross-the-sky thank yous to Kay Campbell and Irma Betters for their help in any and all matters. They make the option work, and work well. Add thank yous in large proportion to Mike "Silver and" Black, who never missed an opportunity to jab me about the most recent Seahawk or Sonic loss to an L.A. team, for his excellence in keeping the computer system running at full bore.

To previous graduate students who have stepped into the great wide world ahead of me, I wish to express my gratitude for the help and support you have given me. This list includes (but is not limited to) Todd Clancy, Arie Grossman, Kathy Pierce Shah, Mark Hofstadter, Don Banfield, Julie Moses, Michelle Santee, Rich Dissly, Kim Tryka, Steve Leroy, Bryan Butler, and The Stuarts.

To my current classmates, I will miss the interesting discussions of science and math and my poor taste in movies with Eric Weisstein, and the talks about comedy, the mysterious beauty of Hualālai, and our good taste in movies (i.e., The Blue Iguana and Army of Darkness) with Hari "Groovy" Nair. Special thanks to Jim Lyons for making the last two DPS meetings really fun to attend and for sharing my love for good beer, good football, and cheesy movies. To everyone else I extend thanks for the numerous discussions I've had with you all, in hallways and offices, that make Caltech a wonderful place to pursue a Ph.D.

Above all, I express my deep appreciation and love for Shannon McCord. It has been an emotional, stressful period in both our lives, but she has always been there for me. It has been her faith in me that has sustained me many times, her patience that has brought me back to earth when I felt lost, her humor that penetrates my darkest moods, her love that protects me and binds me to her.

This work was supported by NSF grant AST 9321602 and NASA grant NAGW–1448 to the California Institute of Technology.

Abstract

This thesis consists of inteferometric observations of carbon monoxide from three planetary atmospheres. The observations address specific questions about the state and structure of each atmosphere. The analysis and results for each planetary body are contained within individual chapters of the thesis, and the abstract for each is reproduced below.

Titan: Evidence for a Well-Mixed Vertical Profile

We report on new millimeter heterodyne observations of the ^{12}CO $J(1-0)$ rotational transition from the stratosphere of Titan made in October 1994 with the Owens Valley Radio Observatory Millimeter Array. The spectrum obtained clearly exhibits a strong emission core over the ~600 MHz bandwidth of the upper sideband spectrometer. The lineshape, referenced to the flat spectrum simultaneously observed in the lower sideband, was inverted to determine a best fit CO mixing ratio profile consistent with the observations. The best fit profile is a constant mixing ratio of $5 \pm 1 \times 10^{-5}$ over the altitude range of 60–200 km. Combined with IR observations of tropospheric CO ($f_{CO} = 6 \times 10^{-5}$, Lutz *et al.* 1983) this provides strong evidence that CO is well mixed from the surface to at least 200 km in Titan's atmosphere.

Mars: Thermal Structure from 0–70 km

Millimeter-wave heterodyne observations of the ^{12}CO $J(1-0)$ rotational transition from the atmosphere of Mars were made on three dates in February 1993 with the Owens Valley Radio Observatory Millimeter Array. These observations yielded high-quality spectra with a spatial resolution of 4.2″ on a 12.5″ diameter Mars. The spectra were numerically inverted for profiles of the local atmospheric temperature from 0 to 70 km, assuming a constant CO mixing ratio for the atmosphere. The derived average low latitude atmospheric temperature profile is approximately 20 K cooler than reference temperature profiles compiled during the Viking era. This new temperature profile is well-matched by cooler profiles determined from whole disk CO measurements, suggesting very little dust loading of the atmosphere at the time of the observations (Clancy *et al.* 1990). In addition, the revealed thermal structure shows variation with latitude, and these temperature profiles compare well with profiles derived from Mariner 9 IRIS observations (Leovy 1982, Santee and Crisp 1993)

and calculated thermal structure from the Mars General Circulation Model (Haberle *et al.* 1993). The temperature profiles were averaged in local time and the resulting cross-section of temperature as a function of pressure and latitude used to infer the mean zonal circulation of the atmosphere. These wind results are somewhat compromised by the relatively low spatial resolution of the observations but do qualitatively match both inferred zonal winds from the Mariner 9 IRIS observations and Mars GCM calculations. These initial observations point toward the desirability of further interferometric measurements.

Venus: Temporal Variations of the Mesosphere

Millimeter-wave heterodyne observations of the ^{12}CO $J(1-0)$ rotational transition from the mesosphere of Venus were made in early November and early December 1994 with the Owens Valley Radio Observatory Millimeter Array. The spatial resolution for each day was about 1000 km at the sub-earth point. The high quality CO spectra were numerically inverted for profiles of the local CO mixing ratio from 80 to 105 km, assuming a Pioneer Venus mean temperature profile for the atmosphere. For each day the revealed CO distribution shows a nightside maximum centered at low latitudes and shifted from the anti-solar point toward the morning terminator. Both days show a clear latitudinal falloff in the CO abundance. In November the maximum was centered at roughly 2^h local time at 100 km, while in December the maximum was at roughly $4 - 4.5^h$ local time at 100 km. In addition, CO abundances were slightly higher in November. The changes in the CO distribution are examined in the context of the mesospheric circulation model of Clancy and Muhleman (1985b). The increased shift away from the anti-solar point and decreased CO abundance for the December observations both point toward increased zonal and/or decreased sub-solar to anti-solar circulation within the mesosphere during the month between observations.

Table of Contents

List of Figures

List of Tables

Chapter 1

Introduction.

The last two decades have witnessed an ever increasing use of millimeter-wave spectroscopy to study a variety of molecular species. Applications range from detection of species in the Earth's stratosphere to measuring the gas content and kinematics of distant galaxies.

Millimeter spectroscopy of planetary atmospheres (other than the Earth's) began with the detection of the CO $J(1-0)$ line on Venus, the first observation of a millimeter-wave transition from a planet (Kakar *et al.* 1975). Since then a handful of spectral lines have been detected and measured at millimeter wavelengths: CO (Venus, Mars, Titan, Neptune), HCN (Titan, Neptune), HC_3N (Titan), and PH_3 (Jupiter, Saturn). The majority of these detections have been made only in the last 5 years.

By far, the most abundant and useful of these measurements have been of CO rotational lines. On Venus and Mars in particular, the CO $J(1-0)$ line (at 115.27 GHz or 2.6 mm) and the CO $J(2-1)$ line (at 230.54 GHz or 1.3 mm) form strong, well-resolved spectral features easily detected from the Earth's surface, and have therefore been studied far longer than any other transitions. In contrast, CO on Titan and Neptune has been much harder to observe, mostly due to the greater distances resulting in much lower fluxes for these objects.

Spectral lines can be used to derive the structure of a planetary atmosphere through a process known as line inversion. The strength and shape of a spectral line is intimately related to the temperature-pressure profile of the atmosphere and the abundance profile of the absorbing species. By making some basic, well-justified assumptions about the atmosphere, it is possible to derive either or both of these profiles. Hence a spectral line can be utilized as a probe of the atmosphere. For

example, this technique has been used to measure the global average CO abundance and temperature of the atmospheres of Venus and Mars (Clancy *et al.* 1990, Clancy and Muhleman 1991, Lellouch *et al.* 1991, Lellouch *et al.* 1994).

One of the most significant advances made within the last decade in millimeter astronomy has been the development of interferometers capable of achieving a spatial resolution of a few arcseconds or better. Until recently, nearly all millimeter observations were made with single antennas, where the spatial resolution is limited by the physical size of the dish. Interferometers offer much higher spatial resolution which is dependent upon the separation of antennas comprising the interferometer.

This thesis presents observations of three planetary atmospheres that use interferometric spectroscopy, allowing measurement of CO spectra with high spatial resolution. Using radiative transfer models of these atmospheres, line inversion algorithms were developed to retrieve basic parameters of atmospheric structure. These data sets represent some of the most detailed interferometric observations of planetary spectral lines ever achieved. The analysis of the spectral features include a firm constraint on the abundance of CO in the stratosphere of Titan, the derivation of the vertical and horizontal temperature structure of the atmosphere of Mars, and monitoring of the time-evolution of the CO distribution in the Venus mesosphere.

Millimeter interferometric spectroscopy of CO offers unique and important ways to measure many characteristics of planetary atmospheres. While emphasizing the direct results of the observations of each planet, it is hoped that this thesis also gives an impression of the power of millimeter interferometric spectroscopy and the techniques of line inversion for studying planetary atmospheres. Millimeter spectroscopy will continue to grow as the opportunity for higher resolution and better system performance at high frequencies is developed and improved at the millimeter facilities around the world.

1.1. Overview

This thesis is divided into several chapters and appendices. Chapter 1 presents a brief introduction to the facility (the Owens Valley Radio Observatory Millimeter Array) used to make the observations described in later chapters, and an introduction to the concepts of interferometry and the reduction of interferometric data.

The next three chapters each present an analysis of observations of carbon monoxide from a planetary atmosphere. Chapter 2 details observations made in October 1994 in order to determine the abundance of CO in the stratosphere of Titan, Saturn's largest moon. Chapter 3 discusses spatially resolved observations made in February 1993 in order to study the thermal structure of the atmosphere of Mars from 0 to 70 km. This structure is useful for constraining thermal-dynamical models of the the Martian atmosphere. Chapter 4 presents spatially resolved observations of carbon monoxide on Venus made in November and December 1994. These observations were sensitive to the distribution of CO in the mesosphere of Venus. The distribution of CO is tied to global circulation in the mesosphere, and variations indicate changes in mesospheric winds. Finally, the summary Chapter 5 reviews the main conclusions of the analyses for each set of observations, and presents a look to the future.

The appendices detail many of the aspects of the analyses used in each chapter. These include a development of radiative transfer at millimeter wavelengths, spatial and spectral convolution, formulations for the opacity of an atmospheric layer, and an overview of an iterative line inversion algorithm dependent on an analytic partial derivative of the radiative transfer equation.

1.2. The OVRO Millimeter Array

The Owens Valley Radio Observatory Millimeter Array is located near Big Pine, California at latitude +37.25° and 1236 m altitude. It is situated in the Owens Valley at the eastern edge of the Sierra Nevada range, whose rain shadow provides

a relatively dry atmospheric environment helpful for radio observations. The Millimeter Array is an interferometer consisting of several 10.4-m diameter radio antennas operational in two "windows," frequency bands of relatively low opacity in the Earth's atmosphere. For the three planetary projects discussed in this text (Titan, Mars, and Venus) observations were made of the ^{12}CO $J(1-0)$ rotational transition at 115.271204 GHz ($\sim$2.6 mm). This line lies near the high frequency edge of the OVRO 3mm band which spans roughly from 80 to 116 GHz.

Over the course of the two years during which the observing runs detailed in this thesis were made the OVRO array has expanded from four to six antennas, and maximum baseline lengths have increased from 172 to 242 meters. In 1992, OVRO switched from a filterbank spectrometer system to a flexible digital cross-correlator spectrometer, allowing for a variety of spectroscopic observations to be made simultaneously with the same system. The observations described here benefited greatly from the continued expansion and improvement of the Millimeter Array, and from the dedication and hard work of the Owens Valley Radio Observatory staff.

Of particular interest for observing extended sources is the size of an antenna primary beam. The primary beam determines the field of view of the interferometer by limiting the sensitivity of each antenna to a small region in the direction the array is pointing. The primary beam of a typical OVRO antenna is roughly gaussian (near the beam center) with a mean FWHM of $69 \pm 3''$ at 100 GHz. This translates to a mean FWHM of $60 \pm 3''$ at the CO transition frequency of 115.27 GHz. As will be discussed in later chapters, this size has important implications for the reduction and analysis of planetary data.

1.3. An Introduction to Interferometry

The basic measurement of an interferometer such as the OVRO Millimeter Array is the cross-correlation, or visibility V, of the electromagnetic signals received

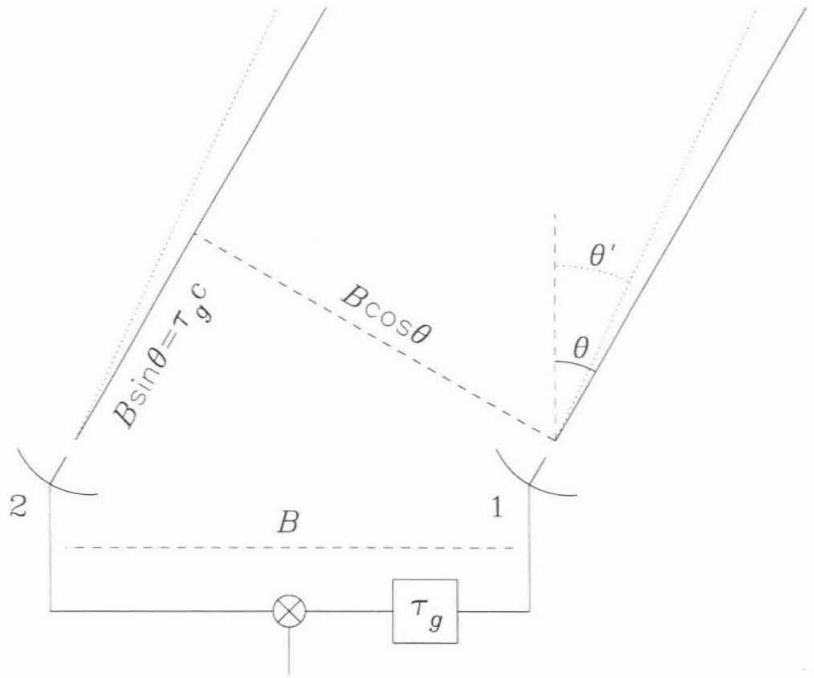

Figure 1.1. The geometry of a simple interferometer observing a source at angle θ from zenith. The signal at antenna 1 is delayed by τ_g so that the correlation will occur for the same wavefront. For a source at θ' the applied geometric delay is incorrect, resulting in a phase difference.

by each possible pair of antennas. Visibilities are complex quantities measured as flux density and often given in units of Janskys (Jy), where 1 Jy $= 10^{-26}$W m^{-2} Hz^{-1}. Consider the simple two element interferometer depicted in Fig. 1.1 observing a point source at angle θ from zenith. Assume that the source is so distant that the signals travel as plane waves by the time they reach Earth. The goal is to correlate the signals received at each antenna on the same wavefront. Obviously, element 2 will measure a wavefront from the source a time $\tau_g = B\sin\theta/c$ later than element 1 (where c is the speed of light). To correlate the same wavefront the signal received at element 1 is delayed by the *geometric delay* τ_g.

A simple example will help illustrate the concept of phase, which will be important for understanding interferometry data and its reduction. Let the point source emit a monochromatic signal at $\omega = 2\pi\nu$. At antenna 1, the signal measured is

$$E_1(t) = E_0 \cos(\omega t + \phi_1), \tag{1.1}$$

where ϕ_1 is the phase of the wave as it reaches antenna 1. Note that this phase is affected by the atmosphere through which the wave passes. The signal at antenna 2 is

$$E_2(t) = E_0 \cos(\omega t + \phi_2) = E_0 \cos\left(\omega(t - \tau_g) + \phi_1\right). \tag{1.2}$$

Delaying the signal measured at antenna 1 by the geometrical delay before multiplying with the signal measured at antenna 2, and filtering out high frequency components leaves

$$\begin{aligned} E_1(t - \tau_g) \times E_2(t) &= E_0^2 \cos^2\left(\omega(t - \tau_g) + \phi_1\right) \\ &= \frac{1}{2} E_0^2 \left[\cos(0) + \cos\left(2\left(\omega(t - \tau_g) + \phi_1\right)\right)\right] \\ &= \frac{1}{2} E_0^2 \qquad \text{(after filtering)}. \end{aligned} \tag{1.3}$$

Hence correcting for the geometric delay leaves a time invariant signal in this simple example.

Now consider that the simple point source is at θ'. The delay of the wave arriving at antenna 2 relative to antenna 1 is τ_g'. We proceed as above:

$$\begin{aligned} E_1'(t - \tau_g) \times E_2'(t) &= E_0^2 \cos\left(\omega(t - \tau_g) + \phi_1\right) \cos\left(\omega(t - \tau_g') + \phi_1\right) \\ &= \frac{1}{2} E_0^2 \left[\cos(\omega(\tau_g' - \tau_g)) + \text{high frequency terms}\right] \\ &= \frac{1}{2} E_0^2 \cos(\phi) \qquad \text{(after filtering)}, \end{aligned} \tag{1.4}$$

where ϕ is the visibility phase, which is time and baseline dependent. The result of Eq. 1.4 is the real part of a complex number, and hence we arrive at the concept of

the complex visibility

$$V_{ij} = < E_i(t - \tau_g) \times E_j(t) > = |V| e^{i\phi}. \quad (1.5)$$

The imaginary component of the visibility is measured along with the real part to determine the complex visibility amplitude and phase (see Thompson *et al.* 1986). The above simplified treatment shows that the interferometer responds to the location of the source, and in this sense phase can be thought of as containing *positional* information.

The apparent separation, or projected baseline, of each antenna pair viewed in the direction of the source ($B \cos\theta$ in Fig. 1.1) is measured in spatial frequency coordinates u (east) and v (north). The main principal upon which interferometry is based is described in the Van Cittert-Zernike theorem, which relates the sky brightness distribution of the source $I(x, y)$ to the visibility function $V(u, v)$, by showing that (in appropriate limits) they comprise a Fourier transform pair (see Thompson *et al.* 1986):

$$V(u, v) = \int_{-\infty}^{\infty} \int_{-\infty}^{\infty} I(x, y)\, e^{-2\pi i(ux+vy)}\, dx\, dy. \quad (1.6)$$

Given complete, noiseless sampling of the source visibility in (u, v) space, the sky brightness distribution of the source is given exactly by the inverse Fourier transform of $V(u, v)$. The objective of observational interferometry is to estimate $I(x, y)$ from a limited, noisy sampling of the source visibility.

Observations are usually carried out over a period of several hours during which the source rises, transits, and sets. During this period the apparent positions of the antennas as viewed from the source change due to Earth rotation, and the projected baselines between antennas change as a function of time. This allows the measurement of $V(u, v)$ at an expanded range of (u, v) locations and is often referred to as Earth rotation synthesis. In addition, the physical location of the antennas

can be rearranged and additional observations made to further improve the (u, v) coverage.

1.4. Basic Interferometric Data Reduction

Despite the use of Earth rotation synthesis and different array configurations, measurements of $V(u, v)$ are usually made at a highly non-uniform set of discrete (u, v) points. We can think of the measured visibilities as the product of a sampling function and the true visibility function (neglecting for clarity the effects of measurement errors):

$$V_M(u, v) = S(u, v)V(u, v), \tag{1.7}$$

where $S(u, v)$ is zero everywhere except where a measurement is made. The direct Fourier transform of $V_M(u, v)$ is usually not a good estimate of the source brightness distribution because the effects of the sampling function are also included.

This effect can be explored through use of the Convolution Theorem (see Bracewell 1965). The Convolution Theorem states that the Fourier transform of the convolution of two functions is equal to the product of the Fourier transform of each function. Hence, the inverse transform of $V_M(u, v)$ is the convolution of $I(x, y)$ and the inverse transform of $S(u, v)$. The latter term is generally referred to as the synthesized beam (or *dirty beam*) $B^D(x, y)$. Note that the dirty beam is essentially the response of the interferometer to a point source of unit flux density. Mathematically,

$$I^D(x, y) = B^D(x, y) \otimes I(x, y) = \int_{-\infty}^{\infty} \int_{-\infty}^{\infty} S(u, v)V(u, v)\, e^{+2\pi i(ux+vy)}\, du\, dv, \tag{1.8}$$

where $I^D(x, y)$ is the *dirty map* and the symbol $\otimes$ denotes convolution. The dirty beam often has irregular sidelobes which redistribute the source flux around the map, distorting (usually strongly) the estimated source brightness distribution.

The spatial resolution of interferometric observations is dependent on the particular sampling of (u, v) space obtained since this defines the dirty beam. However,

the central lobe of the dirty beam is often fairly gaussian in shape, with a FWHM that is roughly inversely proportional to the maximum (u, v) distances for which the visibility function was measured. Just as the spatial resolution of a single antenna (or optical telescope) is inversely proportional to the dish aperture, the synthesized resolution is inversely proportional to the size of the synthesized aperture. This increase in spatial resolution can be very significant. For example, at OVRO the primary antenna beam is roughly 60″ at FWHM at 115 GHz, while the maximum spacing of 240 m could yield about 2.2″ resolution.

The effects of the sampling function (or equivalently the effects of the dirty beam) are typically mitigated through a deconvolution process. The deconvolution and mapping method used here is the CLEAN process, available in the National Radio Astronomy Observatory's software package AIPS (Astronomical Image Processing System). CLEAN takes advantage of the fact that we know in detail the shape of the dirty beam. Consider a single point source at sky coordinates (x_i, y_i) with flux density f_i. The dirty map is simply the dirty beam centered at that point and multiplied by the flux density of the point source, or

$$I^D(x, y) = f_i B^D(x - x_i, y - y_i). \tag{1.9}$$

Since convolution is a linear operation, the dirty map of m point sources is simply

$$I^D(x, y) = \sum_{i=1}^{m} f_i B^D(x - x_i, y - y_i). \tag{1.10}$$

CLEAN uses the assumption that the true source sky brightness can be approximated as the sum of a (possibly large) set of point sources. Although planets are not a collection of point sources, a set can approximate the source sky brightness as long as the separation between points is small compared with the dirty beam FWHM. In other words, convolution of a true continuum disk cannot be distinguished from the convolution of a set of point sources if the points are close enough together.

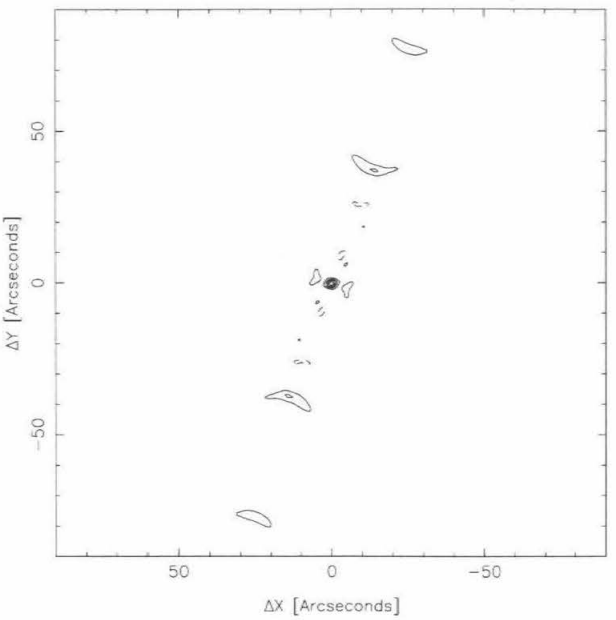

Figure 1.2. A dirty beam B^D from the December 1994 observations of Venus.

CLEAN attempts to perform the "inverse" of Eq. 1.10 and find a set of point sources which will match the data. Essentially, CLEAN starts with $I^D(x, y)$ and locates the highest point in the map. It subtracts from the dirty map a scaled dirty beam centered at that point. The scaling factor and its position (called a *clean component*) are stored, and the process is iterated until the dirty map has been reduced to residual noise. The set of stored clean components are a best fit to the observed sky brightness *in visibility space*. Since the point sources are only a good representation of the true sky brightness when "smoothed" in image space, the clean components are convolved with a restoring (or *clean*) beam, a smooth 2-D gaussian with a FWHM equal to the dirty beam FWHM. Finally, the residual noise map is added back to the map of convolved clean components, and this result is termed the *clean map* I^C.

The result of CLEAN is a map of the sky brightness at the appropriate resolu-

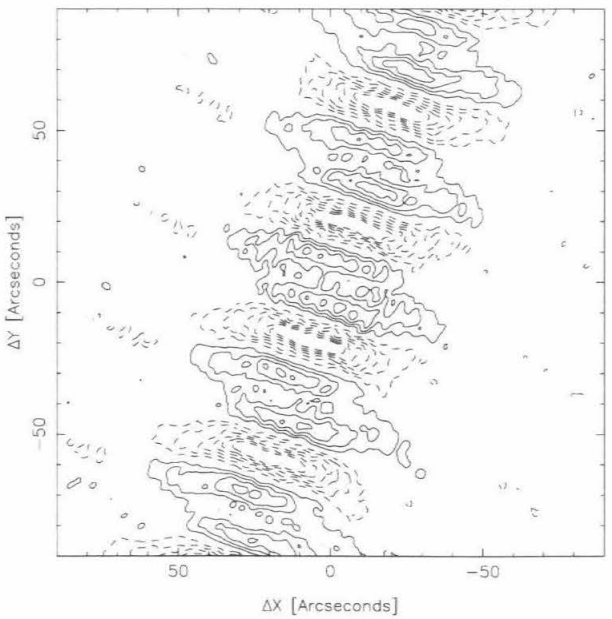

Figure 1.3. A dirty map I^D from the December 1994 observations of Venus.

tion but with the majority of the distortions introduced by the dirty beam removed. This process was originally designed for point sources, but can be applied successfully to resolved sources with smooth features. Planets have sharp edges which are difficult to deconvolve successfully. However, an initial model of the source can be used very effectively with the CLEAN process. The source model is subtracted from the observed visibilities, leaving a residual visibility set which can be handled by CLEAN. For planets a good model is a uniform brightness disk of the planet's radius and position. As well as providing the base extended source structure, the initial model introduces the total flux (the "zero-spacing" flux) which is not measured with an interferometer because observations at (u, v) spacings smaller than the antenna diameters are not possible.

To illustrate the effects of mapping and deconvolution, examples of a dirty beam B^D, a dirty map I^D, and a clean map I^C are given in Figs. 1.2–1.4. These

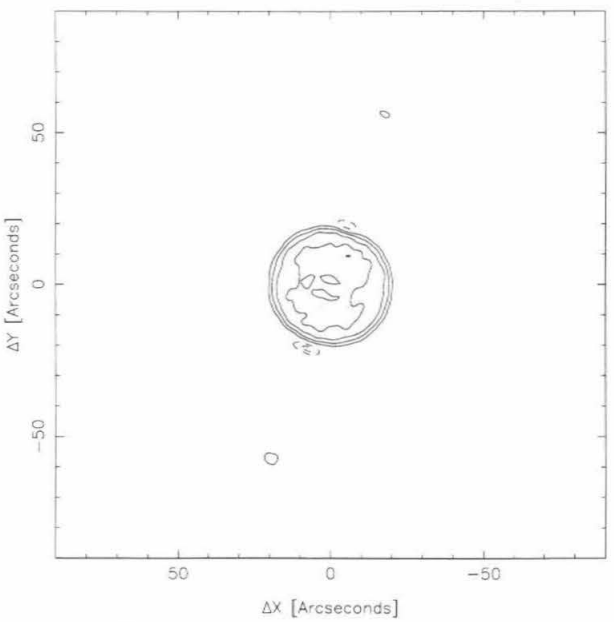

Figure 1.4. A clean map I^C from the December 1994 observations of Venus. For this map and the two previous maps the contours are spaced in increments of 20% of the peak value in that map. Dashed lines represent negative contours.

images, produced during the data reduction of the Venus observations discussed in Chapter 4, show the dramatic improvement that CLEAN can have in producing maps of the estimated sky brightness.

The last interferometry development I will discuss here is phase self-calibration. As shown above, measurement of phase is related to measuring position. However, the above treatment assumed that the delay of the wavefront due to the atmosphere was exactly the same above each antenna. This is generally not the case, and in the millimeter and submillimeter can be very important sources of phase error. In the neutral atmosphere there are two important sources of propagation delay: induced dipole moments of N_2 and O_2 and the permanent dipole moment of H_2O. The first term is stable at roughly 2.3 m of delay in the zenith direction at sea level. The delay due to water vapor, although much smaller, is highly variable because of the high variations in its abundance, both spatially and in time (for more information on the

physics of radio-path delay see Elgered 1993).

This is important because if the characteristics of the atmosphere are different over one antenna relative to another within the array, it will manifest itself as a (positive or negative) delay in the wave at that antenna in addition to any geometric delay. As shown above, delays differing from the geometric delay are interpreted in terms of positional offsets from the center of the map (i.e., from the direction θ in Fig. 1.1). Hence variations in the atmospheric delay between antennas will cause the measured visibility phases to deviate from their "true" values. The net effect will be to distort the estimated source brightness distribution, in effect "moving" flux around in the CLEANed map.

Since this error is antenna-based (i.e., all baselines with antenna 1 are affected if the atmosphere over antenna 1 produces a differential delay with respect to other antennas) we can think of the effects of non-uniform atmospheric delay as introducing a time variable phase gain for each antenna. The measured visibility phase can then be expressed as:

$$\phi_{ij,Meas}(t) = \phi_{ij,True}(t) + \psi_i(t) - \psi_j(t) + \delta_{ij}, \tag{1.11}$$

where $\psi_i(t)$ is the phase gain for antenna i as a function of time and δ is the phase measurement noise on that baseline. It was recognized fairly early in the development of radio interferometry that the sum of the visibility phases around a closed loop of baselines is unaffected by antenna phase gain errors. This property is termed phase closure and is described by

$$\begin{aligned} C_{ijk,Meas} =& \phi_{ij,Meas} + \phi_{jk,Meas} + \phi_{ki,Meas} \\ =& \phi_{ij,True} + \psi_i - \psi_j + \phi_{jk,True} + \psi_j - \psi_k + \phi_{ki,True} + \psi_k - \psi_i + \sum \delta \\ =& C_{ijk,True} + \sum \delta, \end{aligned} \tag{1.12}$$

For an N element array there are N antenna gains (for each time t) and $N(N-1)/2$

visibility phases recorded. If there are enough antennas, the situation is overdetermined and it is possible to solve for the phase gains of each antenna at each time. This process requires that the source be strong (so that the δ's do not contribute significantly to the phase measurement) and that *a priori* knowledge of the source structure exists. The source structure must be modeled in order to provide a working template of the expected values of C_{ijk}. Fortunately, planets are generally strong sources and can be modeled as disks of the appropriate size and flux in the map. The image improvement gained by application of phase self-calibration can be significant. Although an example is not provided here, comparison maps are presented in Chapter 3 (for observations of Mars).

Gain solutions are generally obtained from either a continuum channel or from an average of spectrometer channels uncontaminated by spectral features. This method is used for two reasons. First, the signal-to-noise is usually much greater in a continuum channel (or average of spectrometer channels) due to the larger bandwidth. In addition, the spatial distribution of the spectral feature is usually less well known than that of the background continuum. Using spectral channels contaminated by the lineshape will ultimately distort the derived maps of the spectral feature. After the phase gains are determined from the continuum channel, they are applied to the spectrometer channels.

The above sections have provided a brief but I hope useful introduction to interferometry and the reduction of interferometric data, which can be difficult to grasp upon first exposure. For further details on general interferometry I suggest Thompson *et al.* (1986). A good reference book for the finer details of reducing interferometric data is the NRAO handbook on synthesis imaging edited by Perley *et al.* (1989). The concepts and applications of self-calibration are presented concisely in Cornwell (1989) and a thorough treatment is provided by Pearson and Readhead

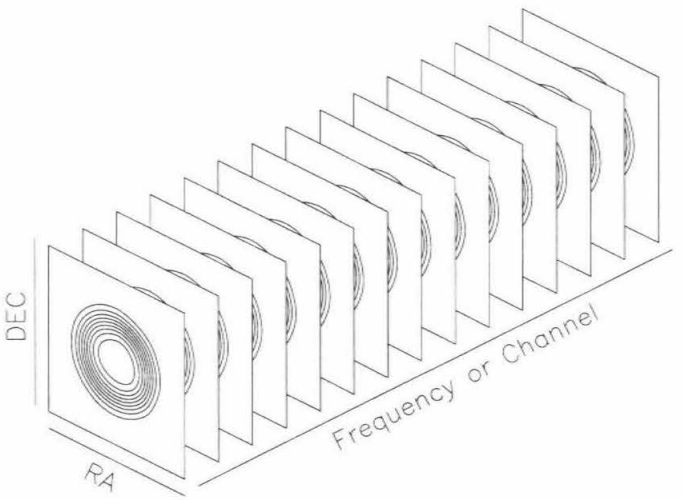

Figure 1.5. A cartoon of a spectral image cube, representing the entire calibrated and mapped data set from spectroscopic measurements.

(1984). Finally, many special adaptations for imaging planets have been developed in the last 15 years, especially with respect to CLEAN and self-calibration; please see Schloerb *et al.* (1979), Rudy *et al.* (1987), Berge *et al.* (1988), and Grossman (1989).

1.5. The Spectral Image Cube

I present one final concept in this section which I hope will improve understanding of spectral line observations. If spectroscopic observations of a source are made, the output data from the interferometer will be a set of measured visibility points for each channel or frequency bin of the spectral observing system (be it a filterbank, digital spectrometer, etc.). The visibilities in each channel therefore represent a measurement of the spatial brightness distribution of the source averaged

over the channel.

The measured visibilities in each channel can be mapped and the dirty beam deconvolved, resulting in a suite of maps of the sky brightness, one map per channel. The full spectroscopic data set can be represented as a *spectral image cube*, as shown in Fig. 1.5, where the axes of the cube are two spatial dimensions (e.g., RA and DEC) and a frequency or channel dimension. The local spectral feature of a particular spot on the mapped source is therefore given by the measured sky brightness at the pixel in each map, creating a spectrum. In this way an interferometer can be used to measure a spectral feature in localized (i.e., beam-sized) regions of a mapped source.

Chapter 2

Titan: Evidence for a Well-Mixed Vertical Profile.

Our understanding of the distribution of carbon monoxide on Titan has come full circle in the past decade, as this chapter details. Initial results suggested that the abundance of CO in the Titan stratosphere was the same as that in the troposphere, as would be expected in a well-mixed atmosphere. However, later measurements at the IRAM facility in Spain were interpreted as showing a dramatic difference, by about a factor of 30, between CO in the stratosphere and troposphere, which was nearly impossible to explain either dynamically or photochemically. Recent improvements to the OVRO Millimeter Array have allowed us to measure a very accurate spectrum of CO, from which we derive an abundance which is very compatible with the original detection, providing very strong evidence that CO is well-mixed up to at least 200 km in the Titan atmosphere. The results presented here were originally published in Icarus as "CO on Titan: Evidence for a Well-Mixed Vertical Profile" (Gurwell and Muhleman 1995, copyright).

ABSTRACT–We report on new millimeter heterodyne observations of the ^{12}CO $J(1-0)$ rotational transition from the stratosphere of Titan made in October 1994 with the Owens Valley Radio Observatory Millimeter Array. The spectrum obtained clearly exhibits a strong emission core over the ~600 MHz bandwidth of the upper sideband spectrometer. The lineshape, referenced to the flat spectrum simultaneously observed in the lower sideband, was inverted to determine a best fit CO mixing ratio profile consistent with the observations. The best fit profile is a constant mixing ratio of $5 \pm 1 \times 10^{-5}$ over the altitude range of 60–200 km. Combined with IR observations of tropospheric CO ($f_{CO} = 6 \times 10^{-5}$, Lutz *et al.* 1983) this provides strong evidence that CO is well mixed from the surface to at least 200 km in Titan's atmosphere.

2.1. Introduction

The complexity of the Titan atmosphere has been appreciated only in the period since the Voyager 1 encounter. One of the most interesting Voyager observations was the detection of CO_2 (Samuelson *et al.* 1983), surprising because the atmosphere of Titan is strongly reducing. The cold temperatures of the lower stratosphere and the troposphere imply that CO_2 condenses out of the lower atmosphere and is continuously deposited on the surface. To sustain the carbon dioxide abundance a source of oxygen is needed, and it is generally assumed to be supplied in the form of water from meteoritic bombardment of the upper atmosphere. An alternate hypothesis is that oxygen is provided by a primordial reservoir of CO, left over from the intial formation of the atmosphere (Samuelson *et al.* 1983, Lutz *et al.* 1983).

The detection of CO_2 suggested that CO was also present as a precursor (Lutz *et al.* 1983). A detailed photochemical model of Titan's atmosphere was developed by Yung *et al.* (1984) in an effort to explain all the Voyager spectroscopic observations and to develop a consistent picture of the important chemical processes in the stratosphere, mesosphere and thermosphere. In the model CO_2 is postulated as the net product of meteoritic water and CO reactions. In a similar manner, CO itself is a net product of meteoritic water and methane reactions. A model dependent mixing ratio for uniformly mixed CO of 1.8×10^{-4} was found to explain the measured CO_2 abundance.

Carbon monoxide was first detected on Titan in near-infrared observations from Earth (Lutz *et al.* 1983). Several absorption features were identified as the *P*- and *R*-branches of the 3–0 rotation-vibration band of CO. Using a reflecting layer model, the authors concluded that they were sensitive to the lower Titan troposphere and that a best-fit mixing ratio for uniformly mixed CO was 6×10^{-5} to within a factor of three. The photochemical lifetime of CO in the atmosphere of Titan is

estimated to be very long, on the order of 10^9 years (Yung *et al.* 1984, Chassefière and Cabane 1991). Coupled with the facts that the molecular weight of CO is the same as for the dominant N_2 gas and that the atmosphere is never cold enough to condense CO, this strongly suggests that carbon monoxide should be uniformly mixed throughout Titan's atmosphere.

Shortly after the infrared detection, millimeter heterodyne measurements of CO were obtained with a two-element interferometer by Muhleman *et al.* (1984). Titan was simultaneously observed in two relatively broad frequency bands (the upper and lower sidebands) with widths of $\sim$ 200 MHz and a separation of 2.6 GHz. The receiving apparatus was tuned such that the upper sideband was centered on the ^{12}CO $J(1-0)$ rotational transition near 115.27 GHz ($\lambda = 2.6$ mm). Collisional broadening of the lineshape due to high pressures in the troposphere and lower stratosphere cause the CO line on Titan to exhibit very broad wings. As a consequence, the lower sideband at –2.6 GHz from the line center measured the far wings of the line. In heterodyne measurements, conversion from the observation frequency to a much lower intermediate frequency (IF) combines the two sidebands into one signal, which can be extremely difficult to calibrate accurately. Fortunately, an interferometer allows isolation of the signals from the two sidebands during observation (see Thompson *et al.* 1986).

The basic measurement of the millimeter observations was the ratio of the flux density in the upper sideband to that in the lower sideband, a powerful technique because this ratio removes nearly all instrumental and weather effects, which impact each sideband in a similar manner. Unlike the infrared measurement, the millimeter observations were sensitive mainly to the stratosphere (roughly 60–300 km). Due to the broadband nature of the observations, the authors were forced to assume a constant mixing ratio over that region. Their best–fit estimate of the stratospheric

CO mixing ratio was $6 \pm 4 \times 10^{-5}$, confirming the IR detection and suggesting that CO is indeed well mixed throughout the troposphere and stratosphere.

However, this interpretation was challenged by more recent millimeter observations of CO reported by Marten *et al.* (1988). Using the IRAM 30–meter antenna near Pico–Veleta, Spain, the group measured a ^{12}CO $J(1-0)$ spectrum in a 500 MHz band around the line center which appears to be far too weak to be consistent with a uniformly mixed CO distribution. This spectrum was used to determine a best fit stratospheric CO mixing ratio of $2 \pm 2 \times 10^{-6}$, roughly a factor of 30 less than the value found for the troposphere. Such a dramatic reduction in the CO mixing ratio with altitude is exceedingly difficult to understand. If CO is derived from water of meteoritic origin, it will be produced high in the upper atmosphere, near 650 km (Yung *et al.* 1984, Chassefière and Cabane 1991). Diffusion arguments alone demand that the stratospheric CO mixing ratio must be at least as great as that in the troposphere in this case. Even if CO were primordial and the source was outgassing, the long chemical lifetime is persuasive evidence for little depletion of the mixing ratio with altitude. Chassefière and Cabane (1991) speculated that such a reduction could be accomplished if CO is adsorbed onto methane ice particles in the region of methane condensation (near the tropopause) which then fall into the troposphere, releasing CO at low altitudes and creating an enhanced tropospheric abundance relative to the stratosphere. A rigorous mechanism, however, has not been advanced to date. We note that this single dish IRAM measurement is complicated by the combining of the sideband signals, which could not be avoided, making accurate calibration of the spectrum very difficult.

Furthermore, the 1988 measurement is incompatible with several measurements of the ^{12}CO $J(2-1)$ and ^{12}CO $J(3-2)$ rotational lines obtained with the Caltech Submillimeter Observatory on Mauna Kea, Hawaii (Muhleman and Clancy,

1993). Due to the increase in line strength with frequency these lines are even broader than the CO $J(1-0)$ line. These spectra clearly show the CO lines and appear consistent with the initial measurements of uniformly mixed CO. Unfortunately, the spectra cannot be reliably calibrated because of the same combined-sideband problem noted for the IRAM measurement.

It is clear that an accurate measurement of the CO mixing ratio within the stratosphere is best made with an interferometer, which has several advantages over single dish measurements. By far the most important is the ability to isolate and independently calibrate the two sidebands. The initial millimeter measurement by Muhleman *et al.* (1984) was made using an interferometer, but owing to the poor spectral resolution of that experiment the Marten *et al.* (1988) result has been more widely accepted. We report here on new interferometric observations of ^{12}CO $J(1-0)$ line that were made in an attempt to resolve the central question of the distribution of CO in Titan's atmosphere. The results of this study have important implications for our understanding of the oxygen budget and photochemistry of the stratosphere of Titan.

2.2. Millimeter Observations

Observations of CO millimeter lines on Titan are complicated by the extreme width of the spectral features, making the design of the experiment crucial to its success. The pressure line-broadening coefficient for CO in a nitrogen atmosphere at 95 K is about 6.5 GHz bar^{-1} (Colmont and Monnanteuil 1986). The surface pressure on Titan is about 1.5 bar and therefore the opacity due to CO is spread over several GHz on either side of the line center. Figure 2.1 illustrates this problem, where model CO $J(1-0)$ spectra are plotted for three different CO distributions: no CO (providing the continuum baseline), a constant mixing ratio of 6×10^{-5} from 0 to 500 km (corresponding to the measurements of Lutz *et al.* 1983 and Muhleman *et al.*

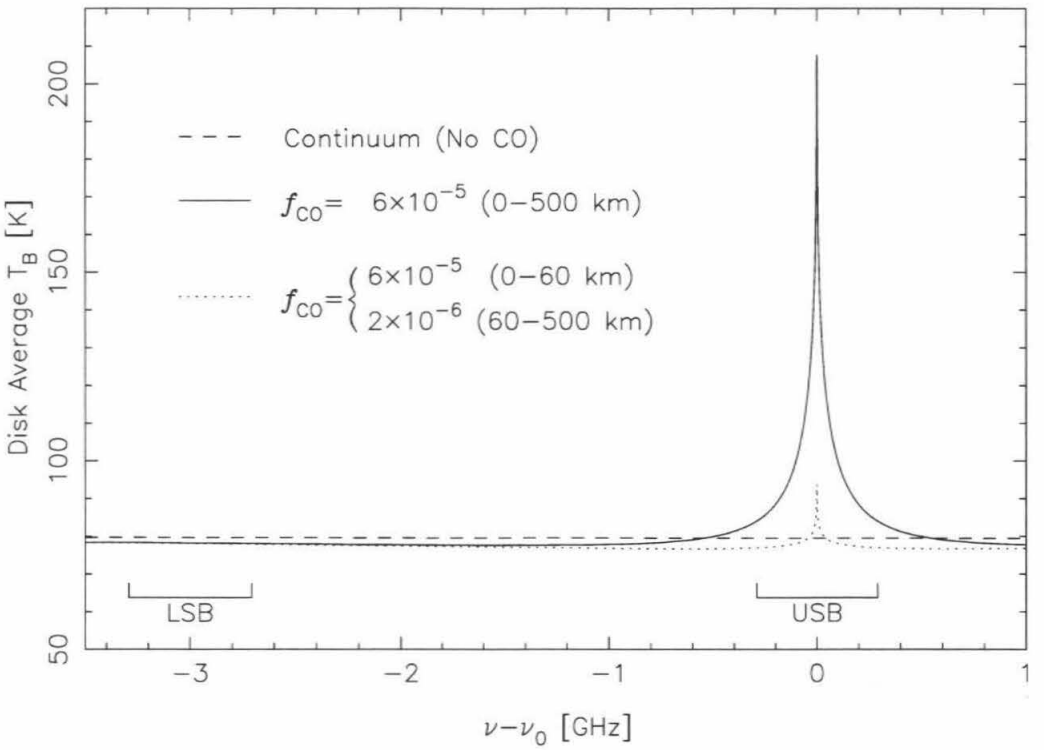

Figure 2.1. Model spectra of the CO $J(1-0)$ rotational transition on Titan.

1984), and constant mixing ratios of 6×10^{-5} for the troposphere (0-60 km) and 2×10^{-6} for the stratosphere (60-500 km, Marten *et al.* 1988). The CO line on Titan exhibits a complex structure, with a strong emission core resting on an extremely broad and shallow absorption line. The strength of the emission core is directly related to the stratospheric abundance of CO, exhibited by the great difference in the model spectra between ±1 GHz from the line center. Current state-of-the-art heterodyne spectrometers have a total bandwidth no larger than 1 GHz, leading to obvious difficulties; it is thus far not possible to achieve sufficient bandwidth to separate the line from the continuum within a single sideband.

The best current method for mitigating this problem is to make double-

sideband observations, with one sideband sampling the line center while the other samples the far wings of the line. This method is difficult for single dish observations, which cannot easily isolate the two sidebands from each other. Calibration in that case relies on an accurate measurement of the sideband ratio, an indicator of the sensitivity of one sideband relative to the other. Interferometers, on the other hand, can isolate the sidebands and therefore can be used to measure the spectral feature in the upper and lower sidebands nearly independently. The ratio of the sidebands then gives a very accurate measure of the spectral lineshape.

Observations of the ^{12}CO $J(1-0)$ line on Titan were made on October 18-20, 1994 with the Owens Valley Radio Observatory Millimeter Array, located near Big Pine, California. The OVRO interferometer is comprised of six 10.4–m diameter antennas. Tracking of Titan for the antennas and for determination of the array phase reference was done by computer control using a high-precision ephemeris provided by E. M. Standish of the Jet Propulsion Laboratory, Pasadena, CA. For the three observing dates Titan was near western elongation, varying between roughly 150–180 arcsec from Saturn. At 2.6 mm, the half-power beam width of an antenna is roughly 60 arcsec, and confusion with Saturn was a concern. However, Saturn was moving relatively rapidly in the phase reference frame centered on Titan, and hence any coherent contribution from Saturn should be minimized, although it must affect the observations as a nearly random noise source.

The interferometer was aligned in a fairly compact configuration, resulting in a synthesized beam of roughly $4'' \times 6''$ full-with-at-half-maximum (FWHM) at Titan's declination of $-11°$. At an apparent diameter of $0.79''$ Titan was therefore completely unresolved. For each night's observations (about 7 hours) the majority of time was spent integrating on Titan. A single measurement on each baseline consisted of a three minute integration during which the complex visibility of the source was recorded.

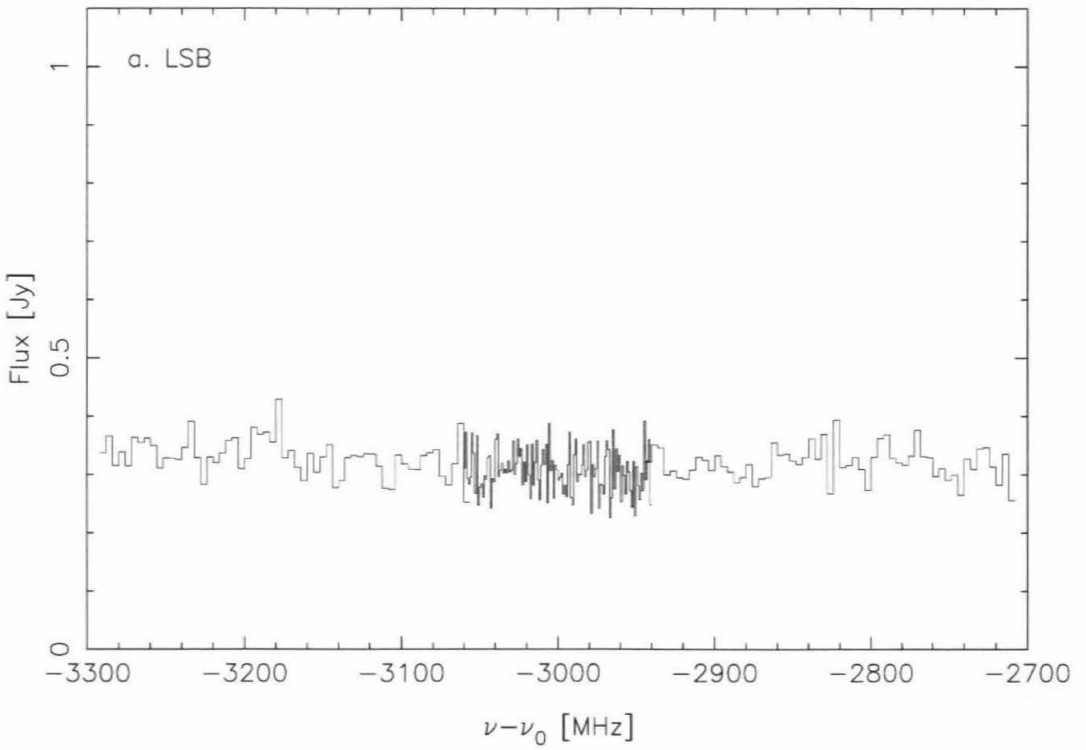

Figure 2.2a. The lower sideband spectrum from the October 18-20 observations of Titan.

Amplitude and phase gain time variations were monitored through observations of a calibrator, quasi-stellar source 2227-088, approximately every half-hour. The flux scale was calibrated independently in each sideband using interleaved observations of Uranus and the calibrator at similar elevations. Previous measurements of the flux of Uranus at the observation wavelength (Muhleman and Berge 1991) were used to determine the flux density of 2227–088 as 2.51±0.05 Jy in each sideband.

The signal was received by a superconductor-insulator-superconductor (SIS) receiver at each antenna which is sensitive in the 80–116 GHz range, and detected for each antenna pair in two correlator systems: a wideband analog cross correlator (~1 GHz bandwidth) and a digital cross correlator. For observation of CO on Titan, the

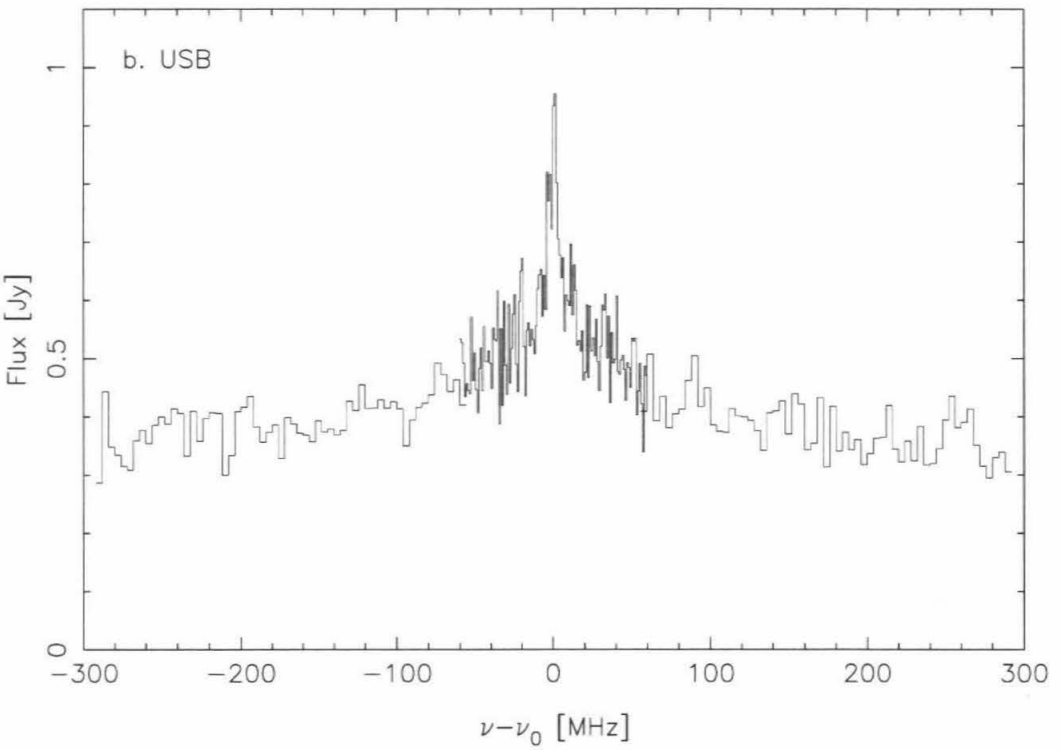

Figure 2.2b. The upper sideband spectrum from the October 18-20 observations of Titan.

upper sideband was centered on the ^{12}CO $J(1-0)$ transition frequency of 115.2712 GHz, dictating that the lower sideband be centered at 112.2712 GHz. The reference was maintained in the Titan frame by computer control of the local oscillator (LO) frequency. The sideband signals were isolated to approximately 20 dB using a phase-switching cycle (see Padin *et al.* 1991 for further information on the OVRO array).

The digital spectrometer was utilized in two secondary LO tunings, allowing us to ultimately measure ±(56–292) MHz of the center frequency of each sideband at 4 MHz resolution, and ±60 MHz at 1 MHz resolution. This spectral coverage is shown in Fig. 2.1 by bars representing the frequency range of the digital spectrometer in each sideband. The upper sideband (USB) spectral data were used to measure the

emission core, while the lower sideband (LSB) spectral data were used to measure the far wing of the line, close to the continuum level. For each integration on each baseline, an USB and LSB amplitude and phase were measured by the continuum correlator and for each channel in the digital correlator. Calibration of the digital correlator passband was done through observations of 3C454.3 and 3C84, which are expected to exhibit flat spectra in the region of interest.

Initial inspection of the continuum correlator data for Titan revealed anomalous phase and amplitude variations on the shortest baseline (15 meters E-W). These variations were most probably the result of confusion with Saturn and/or its rings, to which a short E-W baseline would be most susceptible. Due to this corruption, we did not use the data from the shortest baseline in the following analysis. No other baselines exhibited any noticeable variations, and we feel confident that the rest of the data set is free from any important confusion with Saturn.

After calibration, the spectrometer data for all three days were vector averaged. The results, spectra of the ^{12}CO $J(1-0)$ line on Titan in the upper and lower sidebands, are shown in Figs. 2.2a and 2.2b. The units are calibrated Jy as determined during data reduction. The USB spectrum clearly shows a strong resolved emission line, centered at the transition frequency for CO $J(1-0)$. The LSB spectrum is essentially flat, with no indication of any obvious absorption or emission features. The latter is particularly important because it shows that the sideband isolation procedure was effective to well below the noise level of the spectrum. Although not reproduced here, average spectra for each day of observation clearly show the CO feature as well, but with lower SNR. The noise levels for all three days were roughly comparable.

2.3. Spectrum Modeling

To analyze the spectra, a radiative transfer model of the Titan atmosphere at

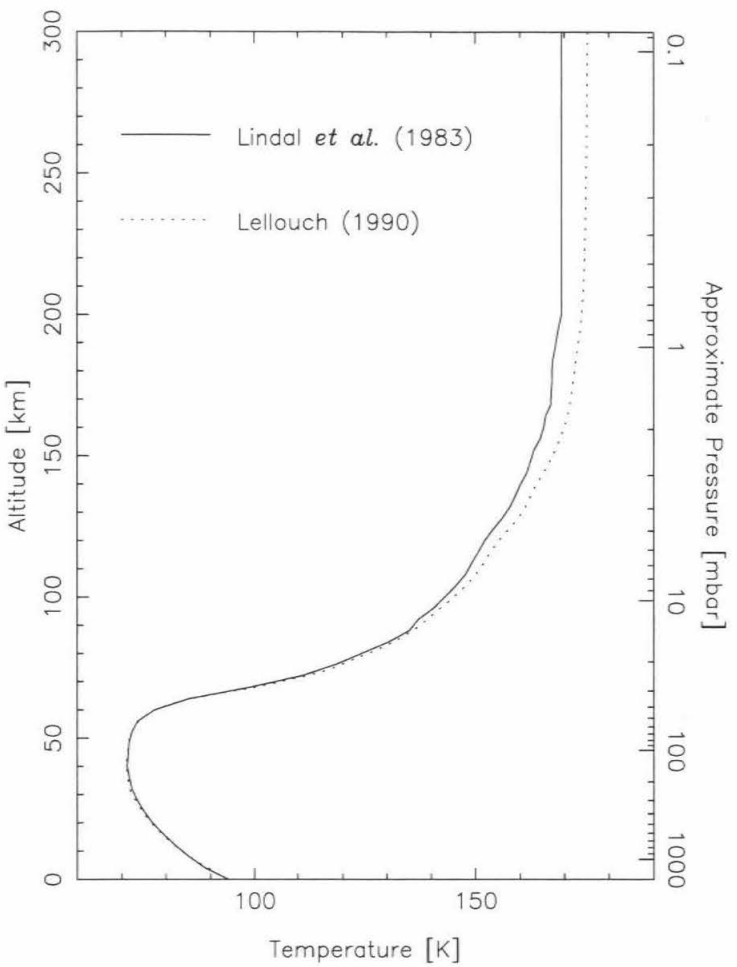

Figure 2.3. Published atmospheric temperature profiles for Titan.

millimeter wavelengths was developed, based upon existing models (Muhleman *et al.* 1984, Muhleman and Clancy 1993). The basic parameters of the atmosphere were taken from the Voyager 1 radio occultation results (Lindal *et al.* 1983), including an atmospheric base at 2575 km from the center of Titan with a surface pressure of 1496 millibar and a surface temperature of 94 K. A reanalysis of the radio occultation data has resulted in the temperature profile presented by Lellouch (1990). Figure 2.3 presents the thermal profiles of Lindal *et al.* (1983) and Lellouch (1990). The Lindal profile has been extended assuming the atmosphere is isothermal above 200 km.

The millimeter continuum opacity on Titan is dominated by $N_2 - N_2$, N_2–Ar and $N_2 - CH_4$ pressure-induced absorptions. The absorption coefficient for each species pair scales with the product of their mixing ratios (i.e., $k \propto f_{N_2}^2$, etc.). Three data sets of the $N_2 - N_2$ absorption were investigated (Dagg *et al.* 1975, Courtin 1988, G. Birnbaum, personal communication, 1984) and one each for the N_2–Ar and N_2–CH_4 absorptions (Courtin, 1988). No important differences between the nitrogen absorption data sets were found in radiative transfer tests. Following Courtin, the N_2–Ar absorption coefficient was taken to be essentially the same as for $N_2 - N_2$, while in the wavelength and temperature range of interest the $N_2 - CH_4$ absorption coefficient is approximately four times that of $N_2 - N_2$. The total continuum opacity was scaled from the $N_2 - N_2$ absorption coefficient for a pure nitrogen atmosphere by the formula

$$k = k_{N_2-N_2} \times (f_{N_2}^2 + f_{N_2} f_{Ar} + 4 f_{N_2} f_{CH_4}) = k_{N_2-N_2} \times f_{N_2}(1 + 3 f_{CH_4}), \qquad (2.1)$$

where we have made the reasonable approximation that $f_{N_2} + f_{Ar} + f_{CH_4} \approx 1$. The continuum brightness temperature is somewhat sensitive to the mixing ratios of N_2 and CH_4 used; model values and error analysis are discussed below.

Opacity due to carbon monoxide was modeled using the spectroscopic parameters of Pickett, Poynter and Cohen (1992). The CO–N_2 collisional broadening coefficient for the CO $J(1-0)$ line was taken to be 2.45 GHz bar^{-1} at 300 K, with a temperature dependence of $T^{-0.86}$ (Colmont and Monnanteuil 1986). The CO opacity for each model frequency and atmospheric layer was found by integrating the CO absorption coefficient times the Voigt lineshape (convolution of Doppler and collisional broadening) over the layer, as discussed in Clancy *et al.* (1983); a review is presented in Appendix C.

The radiative transfer model utilizes a spherical atmosphere extending to 500 km above the surface, with layers of 1–10 km thickness. Using the input apparent

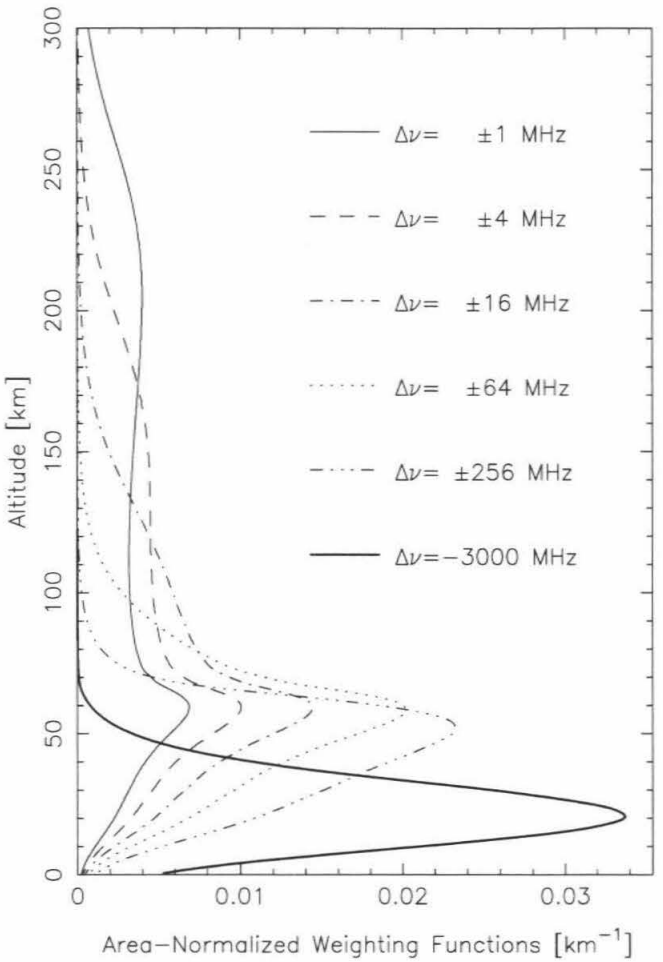

Figure 2.4. Weighting Functions for the CO $J(1-0)$ line on Titan.

diameter of Titan, the intensity is integrated along many paths, including limb geometries, and the results are interpolated and integrated to give the spectrum in units of flux density. The surface is taken to be a perfect sphere of radius 2575 km and dielectric constant of 2.25, although in practice this is rather unimportant as the continuum opacity strongly attenuates radiation from below ~20 km.

Figure 2.4 presents area-normalized nadir weighting functions for several frequency offsets from the CO line center, calculated assuming a constant mixing ratio of 6×10^{-5}. The $\Delta\nu = -3000$ MHz weighting function corresponds to the lower side-

band observations and shows clearly the strong absorption of radiation from the lower atmosphere and the surface by the continuum opacity sources. The other weighting functions are representative of the frequency range of the upper sideband observations. The vertical structures of these weighting functions are strongly dependent upon frequency, allowing us to probe the stratosphere. Note that the contribution from altitudes above ~200 km is very small except for roughly ±4 MHz from the linecenter. In addition, all the USB weighting functions exhibit a maximum near 50–60 km, which is a result of the rapid change in the density gradient just above the tropopause which limits the amount of radiation transmitted from below approximately 60 km. These two altitudes roughly bound the region of maximum sensitivity for our observations.

2.4. Analysis and Conclusions

To analyze the observed spectrum, we first compared the observed lower sideband flux to our model output. The model LSB flux depends on the tropospheric mixing ratios of N_2, Ar and CH_4 (as in Eq. 2.1) and on the tropospheric CO mixing ratio. We assumed mixing ratios of 0.95, 0.01 and 0.04 for nitrogen, argon and methane, respectively. Varying these values throughout their possible ranges (discussed in Lellouch 1990 and Strobel *et al.* 1993) varied the LSB flux by roughly ±0.6%. The tropospheric CO mixing ratio is uncertain by a factor of three (Lutz *et al.* 1993) and this allowed range varied the LSB flux by roughly ±2%, and was therefore a much more significant error source than the continuum opacity sources. Using the best-fit mixing ratio determined by Lutz *et al.* (1983) of $f_{CO} = 6 \times 10^{-5}$ for the troposphere our model calculates the whole disk Planck brightness temperature at 112.3 GHz, equivalent to our LSB measurements, to be T_B =78.4 K (referenced to the surface radius).

In comparison, the average LSB flux from our observations gives a brightness

temperature of 74 K, or about 6% less than the nominal model would suggest. In an effort to match the LSB observations, the Titan model was run multiple times with increasing tropospheric CO mixing ratios. The minimum model T_B obtainable was 77 K, achieved with a mixing ratio of 1.6×10^{-4}. We note that it is not unreasonable that such a discrepancy could exist between our model and the data. Recall that the flux scale was determined from observations of the calibrator 2227-088 interleaved with observations of Uranus. Noise on these observations placed the formal error on the flux of the calibrator at about 2%, but this does not take into account bias which would be introduced by errors in our model of the flux of Uranus. An estimated error of ~5% between observed and expected fluxes is typical at millimeter wavelengths, so it is not unexpected that our LSB data does not exactly match the model.

One of the great advantages of using the interferometer is that the *ratio* of the observations in the two sidebands is very insensitive to errors in the absolute flux calibration, or to any source of errors which would affect both sidebands in a similar manner (such as moderate phase variations not completely removed during calibration, primary antenna pointing errors, or errors in the Titan ephemeris). This is essentially a measurement of the line to continuum ratio, and we expect that the ratio of the USB to LSB observations is a far more accurate measure of the CO lineshape than the calibrated USB spectrum alone. The observed spectrum is shown in this manner in Fig. 2.5, along with several model spectra for comparison. The three solid line spectra correspond, from weakest to strongest, to constant CO mixing ratios of 2, 6, and 10×10^{-5} for the entire atmosphere. These cover the maximum range for the stratospheric CO mixing ratio found by Muhleman *et al.* (1984) and are within the reported errors for the tropospheric mixing ratio (Lutz *et al.* 1983). The dashed line is a model spectrum calculated assuming the results of Marten *et al.* (1988) of 6×10^{-5} (0–60 km) and 2×10^{-6} (60-500 km). Clearly, the CO distribution

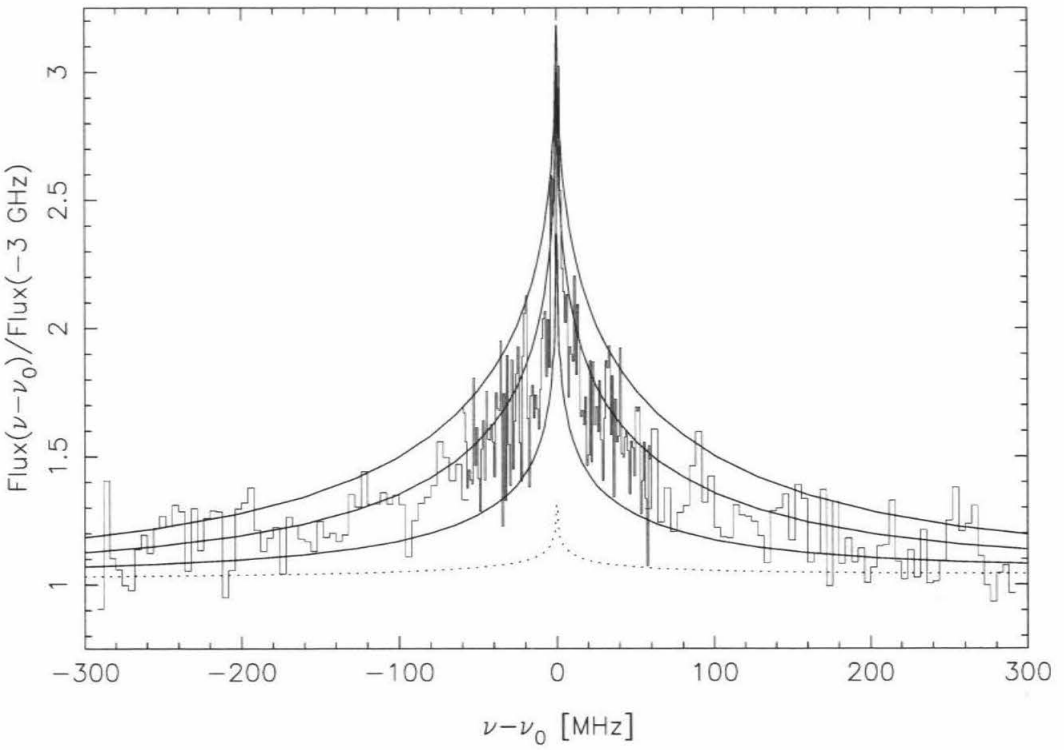

Figure 2.5. Model and observed CO $J(1-0)$ line ratio spectra.

proposed by Marten *et al.* is very inconsistent with our spectral observations, while the spectrum for well-mixed CO at 6×10^{-5} is a reasonably good fit.

We utilized a least-squares line inversion algorithm to quantify the mixing ratio profile that best fits the observed spectrum. Details of the least-squares inversion technique we employed and its application to millimeter CO spectroscopy may be found in Gurwell *et al.* (1995) and an overview is presented in Appendix F. In summary, to determine the best-fit CO profile for a given spectrum we first calculate a model spectrum given an initial estimate of the CO profile. We also calculate the analytic partial derivative of the spectral flux with respect to changes in the CO profile for each frequency. The differences between the observed and calculated spectrum

are used along with the partial derivatives to estimate changes in the profile that will allow for a better fit. The radiative transfer equation is nonlinear, and it is therefore necessary to iterate until a stable solution is reached.

For Titan, we have modeled the CO mixing ratio profile with the functional form $f_{CO} = 10^{P(z)}$ where $P(z)$ was a constant or a first order polynomial with respect to altitude. The objective was to determine the best-fit CO mixing ratio within the stratosphere, and to detect any vertical gradient of the CO profile if it exists. Using the temperature profile of Lellouch (1990), we find that the best-fit CO mixing ratio is $4.9 \pm 0.5 \times 10^{-5}$ (formal error estimate) with essentially no vertical gradient. The best-fit model spectrum for a constant mixing ratio of 4.9×10^{-5} is shown in Fig. 2.6 along with the observed spectrum. The model spectrum provides an excellent fit to all portions of the spectrum.

This solution is extremely insensitive to the CO mixing ratio assumed for the troposphere (0–50 km) for tropospheric mixing ratios less than about 1.2×10^{-4}. Even for the very high tropospheric mixing ratio of 1.8×10^{-4} (taking the maximum error of the results of Lutz *et al.* 1983) the best-fit stratospheric CO mixing ratio drops only marginally to 4.1×10^{-5}.

When determining a best-fit profile assuming a constant mixing ratio with altitude, the solution is insensitive to the temperature profile of the middle and upper stratosphere. Solutions for constant profiles obtained using the Lellouch (1990) and the Lindal *et al.* (1983) temperature profiles shown in Fig. 2.3 are indistinguishable. These temperature profiles are essentially the same below $\sim$ 90 km and diverge to a maximum difference of about 5 K above approximately 150 km, with the Lellouch profile being warmer.

Best-fit solution profiles found when trying to determine a slope, in contrast to the constant profiles discussed above, do show some sensitivity to the temperature

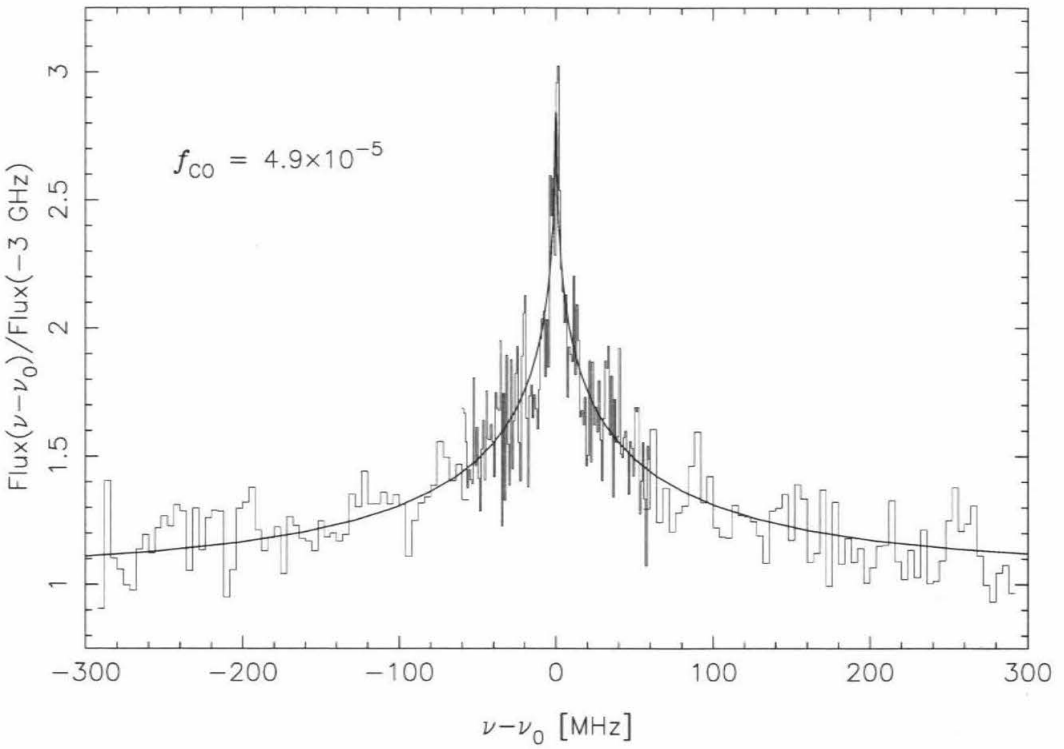

Figure 2.6. The best fit model line ratio spectra along with the observed spectra.

profile in the stratosphere. Figure 2.7 presents first order polynomial solutions found assuming the temperature profile of (a) Lellouch (1990) and (b) Lindal *et al.* (1983). Formal error estimates based upon the covariance matrix determined during the final iteration of the inversion algorithm are also shown. The solution found assuming the Lellouch temperature profile has essentially no vertical gradient to well within the formal errors. The solution found using the Lindal profile, cooler in the stratosphere, does exhibit a marginal positive gradient. To achieve the same spectrum the upper stratospheric CO mixing ratio must increase to offset the lower temperature, as intuitively makes sense. Note that the formal errors on this profile do not exclude the possibility of a constant solution profile. In addition, the formal errors are smallest in

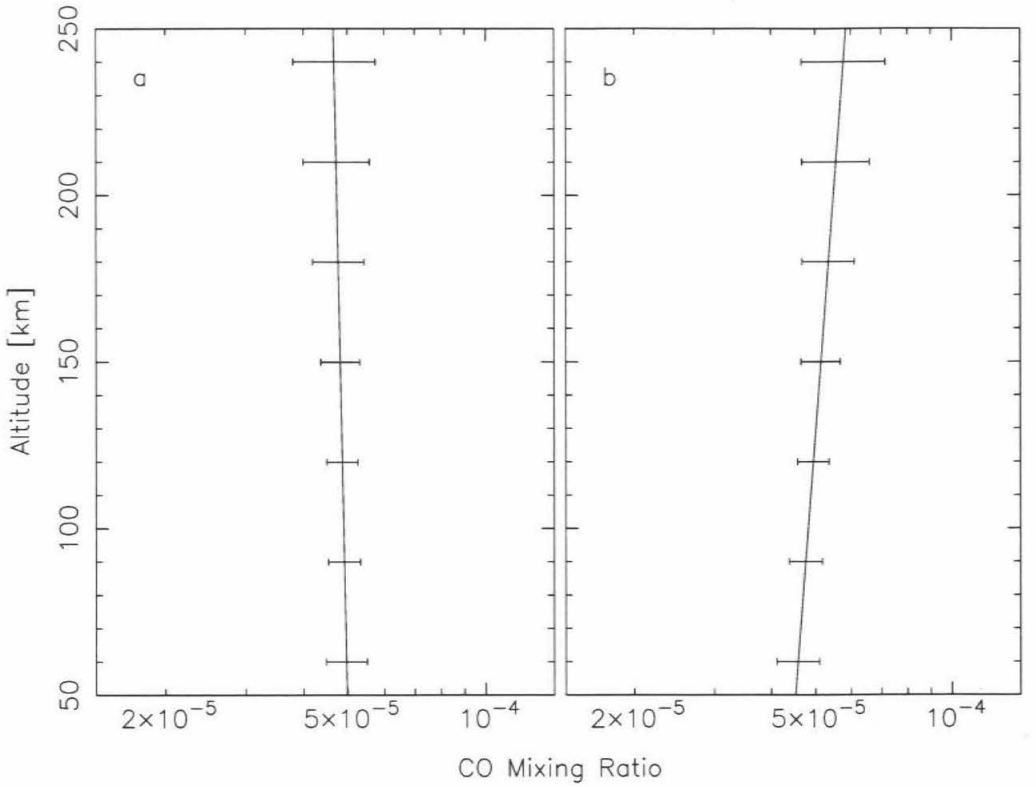

Figure 2.7. Best fit model CO mixing ratio profiles from inversion of the observed spectra. (a) Solution obtained using the Lellouch (1990) temperature profile. (b) Solution obtained using the Lindal *et al.* (1983) temperature profile.

the altitude region of roughly 80-130. In this region note that the mixing ratio solution is essentially the same for either profile shown in Fig. 2.7 and is quite comparable to the constant solution of 4.9×10^{-5}.

Given the uncertainty on the appropriate temperature profile for our observations, we conclude that this new CO spectrum is consistent with a uniformly mixed CO profile throughout at least the 60–200 km region of the atmosphere of Titan. The best-fit mixing ratio found through inversion of the lineshape is $5 \pm 1 \times 10^{-5}$, with the formal error estimates presented above increased to account for uncertainties in the temperature profile. This mixing ratio is very consistent with that found from the original millimeter detection of CO on Titan (Muhleman *et al.* 1984) but is impossi-

ble to reconcile with the results of Marten *et al.* (1988). We suggest that the current observations are the most accurate taken to date, and that our ability to isolate and independently calibrate the spectral data from both sidebands makes these results more credible than the IRAM measurements. In addition, the mixing ratio we determine for the stratosphere is very close to that found for the troposphere from the IR observations of Lutz *et al.* (1983) and is much more tightly constrained. Coupled with the very long chemical lifetime of CO in the atmosphere of Titan, this result is strong evidence that CO is well-mixed throughout the troposphere and stratosphere of Titan with a mixing ratio of 5×10^{-5}.

Chapter 3

Mars: Thermal Structure from 0–70 km.

Mars continues to be a major focus of planetary exploration, and is the objective of several unmanned missions in the next decade, such as Mars 96, Mars Pathfinder, and Mars Global Surveyor. The large cost, infrequency, limited payload, and relative risk of such missions (i.e., Mars Observer) leaves a vital role for ground-based observational programs now and in the future. Of particular interest is measurement of the state of the atmosphere, its temperature structure, circulation, and temporal variability.

Millimeter observations of CO provide a unique and powerful way to monitor the atmosphere of Mars. Single dish observations of CO have had remarkable success in measuring the average thermal structure of Mars atmosphere from 0 to 70 km, culminating (and continuing) with the work of Clancy and Muhleman (e.g., Clancy, Muhleman, and Berge 1990). Such observations, while extremely useful, are limited to examining the average conditions of the atmosphere at low to mid latitudes. The superior spatial resolution of interferometric observations of CO can be used to define variations in the temperature structure with local time and latitude. As discussed in this chapter, resolved measurements of the thermal structure can in turn be used to infer the mean circulation of the atmosphere.

ABSTRACT–Millimeter-wave heterodyne observations of the ^{12}CO $J(1-0)$ rotational transition from the atmosphere of Mars were made on three dates in February 1993 with the Owens Valley Radio Observatory Millimeter Array. These observations yielded high-quality spectra with a spatial resolution of 4.2″ on a 12.5″ diameter Mars. The spectra were numerically inverted for profiles of the local atmospheric temperature from 0 to 70 km, assuming a constant CO mixing ratio for the atmosphere. The

derived average low latitude atmospheric temperature profile is approximately 20 K cooler than reference temperature profiles compiled during the Viking era. This new temperature profile is well-matched by cooler profiles determined from whole disk CO measurements, suggesting very little dust loading of the atmosphere at the time of the observations (Clancy *et al.* 1990). In addition, the revealed thermal structure shows variation with latitude, and these temperature profiles compare well with profiles derived from Mariner 9 IRIS observations (Leovy 1982, Santee and Crisp 1993) and calculated thermal structure from the Mars General Circulation Model (Haberle *et al.* 1993). The temperature profiles were averaged in local time and the resulting cross-section of temperature as a function of pressure and latitude used to infer the mean zonal circulation of the atmosphere. These wind results are somewhat compromised by the relatively low spatial resolution of the observations but do qualitatively match both inferred zonal winds from the Mariner 9 IRIS observations and Mars GCM calculations. These initial observations point toward the desirability of further interferometric measurements.

3.1. Introduction

Millimeter-wave observations of CO in the Martian atmosphere have been ongoing for the last two decades, and there are good reasons for the continued exploration of Mars through CO spectroscopy. CO is relatively abundant on Mars and forms strong, well-resolved spectral features at millimeter wavelengths observable from the Earth's surface. The shape of the CO line contains information about the vertical structure of the atmosphere, including the CO abundance and the pressure-temperature profile. Such information is invaluable for studying the photochemistry, thermal forcing, and dynamics of the Martian atmosphere.

Millimeter spectra of planetary CO lines are composed of essentially two components: an emission-absorption line formed by CO within the planetary atmosphere

and a background or continuum due to thermal radiation from either the lower atmosphere (i.e., Venus) or, as is the case for Mars, from the surface and immediate subsurface (Clancy *et al.* 1990). Since radiative transfer and the formation of rotational absorption lines are relatively straightforward at millimeter wavelengths, it has been possible to use observed CO spectra to infer the vertical, and more recently the spatial, structure from the surface to about 70 km in the atmosphere of Mars.

Previous observations and analyses of millimeter CO spectra from single dish measurements have been presented by Kakar *et al.* (1977), Good and Schloerb (1981), Clancy *et al.* (1983), Lellouch *et al.* (1989, with a reanalysis by Clancy and Muhleman 1990), Clancy *et al.* (1990), Lellouch *et al.* (1991), Lellouch *et al.* (1993), Clancy *et al.* (1993), and Clancy *et al.* (1994). The majority of these are whole-disk spectra and yield average results for the atmosphere. Good and Schloerb proposed a factor of four increase in the CO abundance from 1967 to 1980 based on analysis of CO $J(1-0)$ spectra taken in 1980. However, the analysis of ^{12}CO millimeter spectra has been shown to be extremely sensitive to the assumed contrast between the atmospheric temperature and the brightness temperature of the surface/subsurface (Kakar *et al.* 1977, Clancy *et al.* 1990). Clancy *et al.* (1983) demonstrated that plausible variations in the atmospheric temperature profile of Mars were at least as likely as variations in CO abundance to explain the CO spectra observed by Kakar *et al.* and Good and Schloerb.

Additional evidence against large changes in CO abundance comes from measurements of O_2 in 1971-1972 (Barker 1972, Carlton and Traub 1972) and 1982 (Trauger and Lunine 1983). The O_2 abundances found for these two observations were essentially the same. O_2 and CO abundances are expected to be anticorrelated on such timescales, and the lack of an observed variation in oxygen implies that CO also varied little between the two observing periods (Clancy *et al.* 1990).

More recently, combined observations of the optically thick ^{12}CO and optically thin ^{13}CO lines have been made (Lellouch *et al.* 1989, Clancy *et al.* 1990, Lellouch *et al.* 1991). The dual line observations allow a self-consistent measurement of the CO mixing ratio (assumed constant with altitude) and temperature profile. Although large temperature variations have been noted, the CO mixing ratio has proven to be remarkably consistent among the observations at $8 \pm 2 \times 10^{-4}$. In addition, the observations of Lellouch *et al.* (1991) partially resolved the disk, allowing some measurement of the spatial variability of CO. Their data were consistent with a spatially uniform CO mixing ratio, indicating that meridional mixing is efficient enough to redistribute CO, preferentially produced at temperate latitudes, uniformly over the planet.

Models of Martian atmospheric chemistry (e.g., Moreau *et al.* 1991, Nair *et al.* 1994) have shown that the chemical lifetime for CO on Mars is greater than a year. The spin rate of Mars is much shorter than this timescale, arguing strongly that CO should show essentially no diurnal abundance variation. In addition, meridional wind velocities have been inferred based on measured atmospheric temperature structure from the Mariner 9 IRIS experiment (Santee 1993, Santee and Crisp 1995). They estimate a meridional mixing timescale from the tropics to the polar regions of only 13 days, again much shorter than the chemical loss timescale and strong evidence that CO is well-mixed latitudinally. Finally, estimates of vertical velocities have led to the conclusion that the exchange time between the lower portion of the middle atmosphere (10-40 km) and the upper portion of the middle atmosphere (40-100 km) is just 5–10 days (Barnes 1990). All the above arguments favor a CO distribution on Mars that is uniformly mixed in local time, latitude, and altitude.

Since any temporal and spatial variations of CO are at most relatively small, the primary use of whole-disk CO spectroscopy is in the measurement and monitoring

of the thermal structure of the atmosphere. Radiation at millimeter wavelengths is essentially unaffected by aerosol scattering, making observations of CO well-suited for measuring temperatures in both clear and dusty periods. Clancy *et al.* (1990) have compiled measurements of the mean atmospheric temperature at 0.5 mbar from spacecraft IR measurements and Earth-based CO spectral data. When mapped as a function of L_S the measurements indicate two "states" of the atmosphere: periods of relatively warm temperatures are indicative of the Viking era and parts of the Mariner 9 era, while CO measurements have described both warm and distinctly cooler periods. The Viking era was noted for being relatively dusty; during the mission two major planetary dust storms occurred and a background dust haze was always present. Coupled with the large dust storm observed during the Mariner 9 mission, it appeared that a dusty Martian atmosphere was the rule. However, the CO observations of much colder temperatures at other times implies that the Martian atmosphere undergoes periods with a nearly dust-free atmosphere, which may represent the true background state of the atmosphere.

While indispensable for determining the average conditions of the atmosphere, whole-disk measurements are limited to just that, average conditions at low to mid-latitudes. The development of radio interferometers operational at millimeter wavelengths allows much higher spatial resolution, and therefore the opportunity to determine localized temperature profiles. Such measurements can be used to infer zonal and meridional circulation and to monitor atmospheric conditions at higher latitudes.

This paper presents interferometric observations of the Mars ^{12}CO $J(1-0)$ rotational transition made with the Owens Valley Radio Observatory Millimeter Array. The observations achieved a spatial resolution of 4.2″ when Mars was at a diameter of 12.5″. The resulting data set includes CO spectra from spatially independent regions of the observable disk of Mars. The spectra have been inverted for local atmospheric

temperature profiles from the surface to 70 km. The average temperature structure is approximately 20 K cooler than reference profiles from the Viking era, suggesting very little dust loading of the atmosphere at the time of the observations. However, the latitudinal temperature structure of the atmosphere is similar to both observations and models for the same season. In addition, zonal winds were inferred from the mean temperature structure as a function of latitude using the gradient wind equation.

3.2. Millimeter Observations and Data Reduction

This section offers details of the interferometric observations of CO on Mars, and discusses the reduction of the visibility data into localized spectra of the CO line. In addition, errors in observatory software were discovered in the first year after the data were taken, and a discussion of their impact on this data set is provided.

3.2.1 Millimeter Observations

Observations of Mars in the ^{12}CO $J(1-0)$ rotational transition were obtained with the Owens Valley Radio Observatory Millimeter Array interferometer on February 7, 11, and 13, 1993. At the time of the observations, the OVRO interferometer consisted of four 10.4-m diameter antennas, moveable to a variety of fixed stations along T-shaped railroad tracks. Each days observation consisted of a roughly 11 hour track of Mars, plus further calibration observations at the beginning and end of the track. Very long tracks were allowed by the favorable high declination of Mars (approximately $+27°$), enabling excellent baseline rotation. To further improve the (u, v) coverage and the measurement of the visibility function of Mars, the four antennas were moved into different configurations between successive days of observation. The maximum baseline obtained was 200 m (E-W) and the smallest was 19.7 m (N-S). Figure 3.1 presents the resulting coverage in (u, v) space for all three days. Each

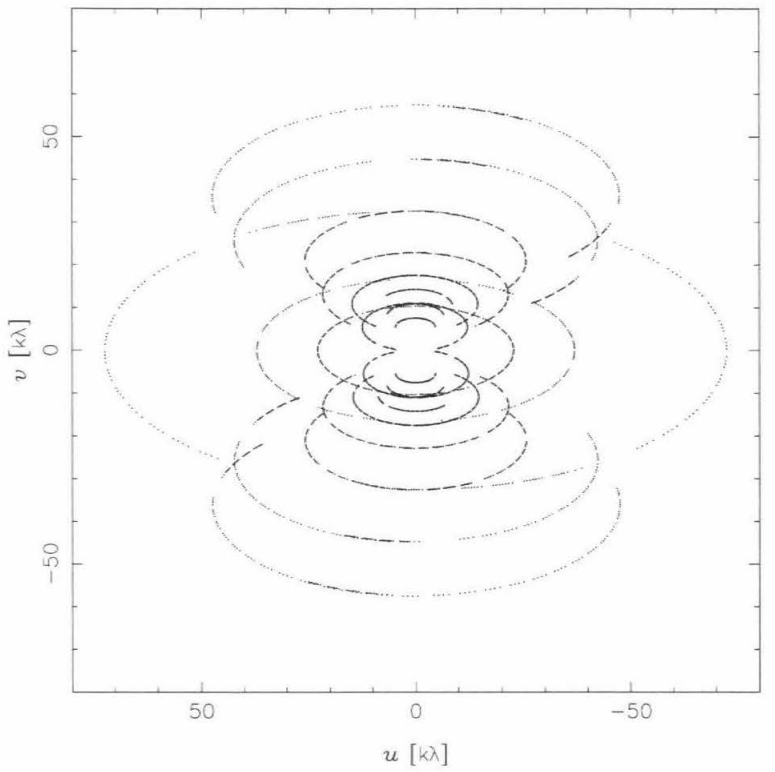

Figure 3.1. A map of the (u, v) coverage obtained for the Mars observations of February 1993. Each point represents one measurement of the complex visibility in the continuum correlator bandpass and in each channel of the digital correlator spectrometer. The baseline u and v components are given in terms of kilowavelengths ($\lambda = 2.6\,\mathrm{mm}$).

point in the figure represents a single measurement of the complex visibility of Mars.

Superconductor-insulator-superconductor (SIS) receivers sensitive in the 80–116 GHz range were used to receive the microwave signal from Mars, detected for each antenna pair in two sidebands. The signals from each sideband were isolated through phase switching of the local oscillator (LO) reference signal. For observation of CO on Mars the upper sideband was centered on the ^{12}CO $J(1-0)$ transition frequency of 115.271204 GHz and receiver gains were optimized to favor this sideband as much as possible to improve signal-to-noise. The transition frequency reference was maintained in the Mars frame by computer control of the LO. The signal in the upper

TABLE 3.1

Parameters for the 1993 Observations of Mars

Reference Date		0^h 7 February
Right Ascension		$6^h\ 41^m$
Declination		26° 58′
Geocentric Distance		0.7492 AU
Apparent Diameter		12.49″
Sub-earth	Latitude	+3.8°
	Local Time	10:40 AM
Sub-solar	Latitude	+14.81°
L_S		36.5
North Pole Position Angle		338.4°
Synthesized beam		4.2″

sideband was detected in two correlator systems: a wideband analog cross-correlator ($\sim$ 350 MHz bandwidth) and a digital cross-correlator spectrometer. The digital spectrometer was configured to measure the CO line at two spectral resolutions: 1 MHz (total effective bandwidth 120 MHz) and 62.5 kHz (total effective bandwidth 7.5 MHz). Each of the two bands were centered on the Mars CO transition frequency. Padin *et al.* (1991) provides further details on the OVRO interferometer and its capabilities.

The CO lineshape extends to roughly 100 MHz on either side of the line center, depending on the local surface brightness temperature. As a result, only the wideband correlator sampled the Mars continuum. The 1 MHz band sampled most of the CO line except for the extended wings. The 62.5 kHz band sampled the inner line core at high resolution. The full complement of the continuum and digital spectrometer data provide a nearly complete characterization of the full CO lineshape. This allows for numerical inversion of the lineshape for atmospheric parameters such as temperature or abundance profiles with altitude.

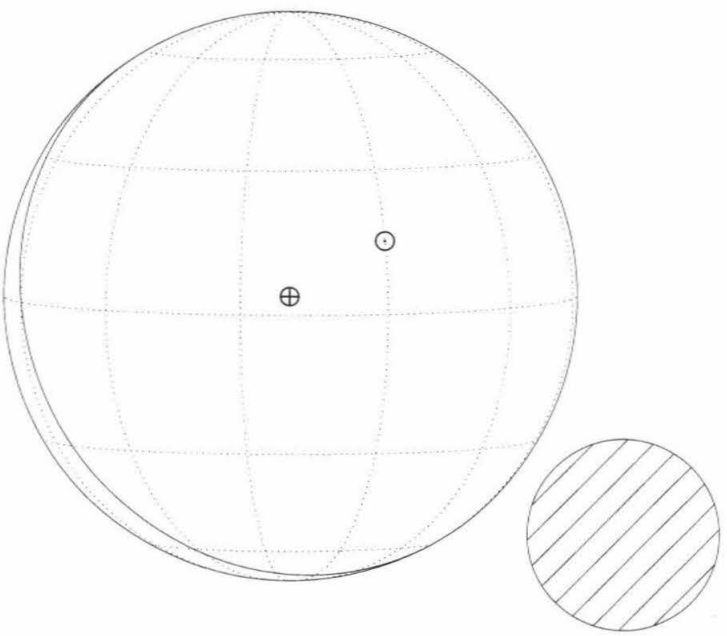

Figure 3.2. The aspect and size of Mars during the February 1993 observations. The north pole position angle has been removed so that Martian north is at the top of the figure. The $\oplus$ and $\odot$ symbols designate the sub-earth and sub-solar points, respectively. The solid line forming a crescent on the lower left marks the morning terminator. The thatched circle in the lower right of the figure shows the size of the synthesized beam at FWHM (4.2″) relative to the diameter of Mars (12.49″).

In order to monitor instrumental and atmospheric variations during observations, it was necessary to calibrate regularly by observing standard sources. Basic parameters such as antenna positions and delays on signal lines between the antennas and the correlators were determined after every change of the antenna configuration. These spectral line observations required careful calibration of the digital spectrometer passband, accomplished through observations of Mercury and 3C273, strong sources with flat spectra, before and after each days track. During each track phase and amplitude gain variations (both instrumental and atmospheric) were monitored through periodic observations of the quasi-stellar sources 0528+134 and 0748+126.

The absolute flux level was calibrated by using Mars itself, for which models of its thermal emission exist; the flux calibration method is discussed below.

At the time of the observations Mars was past opposition and quickly growing smaller in angular extent. Over the ~7 day period during which observations were performed the apparent diameter of Mars dropped from 12.5 to 11.8 arcseconds. It was therefore necessary to normalize the observed values of u, v, and $V(u,v)$ to values appropriate for a reference day, 0^h February 7, 1993. Table 3.1 and Fig. 3.2 detail some of the important parameters of Mars during the observing period. The observations occurred during Martian mid-northern spring. As seen in Fig. 3.2 the sub-earth point was nearly equatorial and centered in the late morning (Martian local time). The observations of Mars occurred over roughly 11 hours for each day, during which Mars rotated about its own axis roughly 165° . In addition, the sub-earth longitude at transit varied by about 55° over the observing week. This caused the data set to be smeared out in longitude (i.e., much more than the synthesized beam size). However, the local time and latitude of the sub-earth point changed very little during the week, such that the data set resolves the disk of Mars to the limit of our beam size in latitude and local time. For each of the three days of observation, a visibility was measured in the continuum channel and in each channel sampled by the digital spectrometer roughly every 5 minutes, with observations of calibrators roughly every 30 minutes.

3.2.2 Calibration and Data Reduction

Initial calibration was performed using MMA, a software package developed for use with data taken with the OVRO millimeter interferometer. This calibration included flagging of obviously spurious visibilities, removal of phase and amplitude drifts with time, setting the flux scale, and calibration of the spectrometer passband. The resulting combined data set for all three days included 1527 complex visibilities

in the continuum and in each spectral channel.

The flux scale was determined by measuring the flux of the calibrator 0528+134 based on comparison with the observations of Mars on short (u, v) spacings. The thermal emission of Mars at centimeter wavelengths has been accurately modeled based on measurements obtained with the Very Large Array (Rudy 1987, Rudy *et al.* 1987). This model was utilized to calibrate the millimeter flux of the OVRO measurements as this technique has been applied successfully to interferometric measurements of Uranus and Neptune (Muhleman and Berge 1991) and to single dish observations of CO on Mars (Clancy *et al.* 1990). For the particular season and sub-Earth geometry, the thermal model calculates a whole disk brightness temperature of 195 ± 5 K, equivalent to a total flux of 226 ± 6 Jy at 115.27 GHz. The short spacing visibility data of Mars were used to determine the flux of 0528+134 as 6.7 ± 0.3 Jy. This flux was then used to calibrate the entire dataset.

The quality of the data set can be assessed by comparing the observed visibilities with a model visibility function. To first order Mars appears as a uniform brightness disk. The Fourier transform of a uniform disk (derived using Eq. 1.6) is proportional to the 1st Lambda function (e.g., Born and Wolf 1980):

$$V(u,v)_{\rm disk} \;=\; I_\nu \pi R^2 \Lambda(2\pi\beta) \;=\; I_\nu \pi R^2 \frac{J_1(2\pi\beta)}{\pi\beta}. \qquad (3.2)$$

Here I_ν is the surface intensity of the disk, R is the disk radius in radians, J_1 is the Bessel function of first order, and $\beta = R\sqrt{u^2+v^2}$. In the limit of $\beta \rightarrow 0$ (i.e., as the projected baseline $\sqrt{u^2+v^2}$ goes to zero) the visibility approaches the full disk flux $I_\nu \pi R^2$. As the baseline length is increased the disk is "resolved" to some extent and the visibility amplitude decreases (or flux is "resolved out").

Figure 3.3 presents the 1527 real components of the continuum channel visibilities as a function of $\sqrt{u^2+v^2}$. Also shown is a best fit model for a uniform brightness

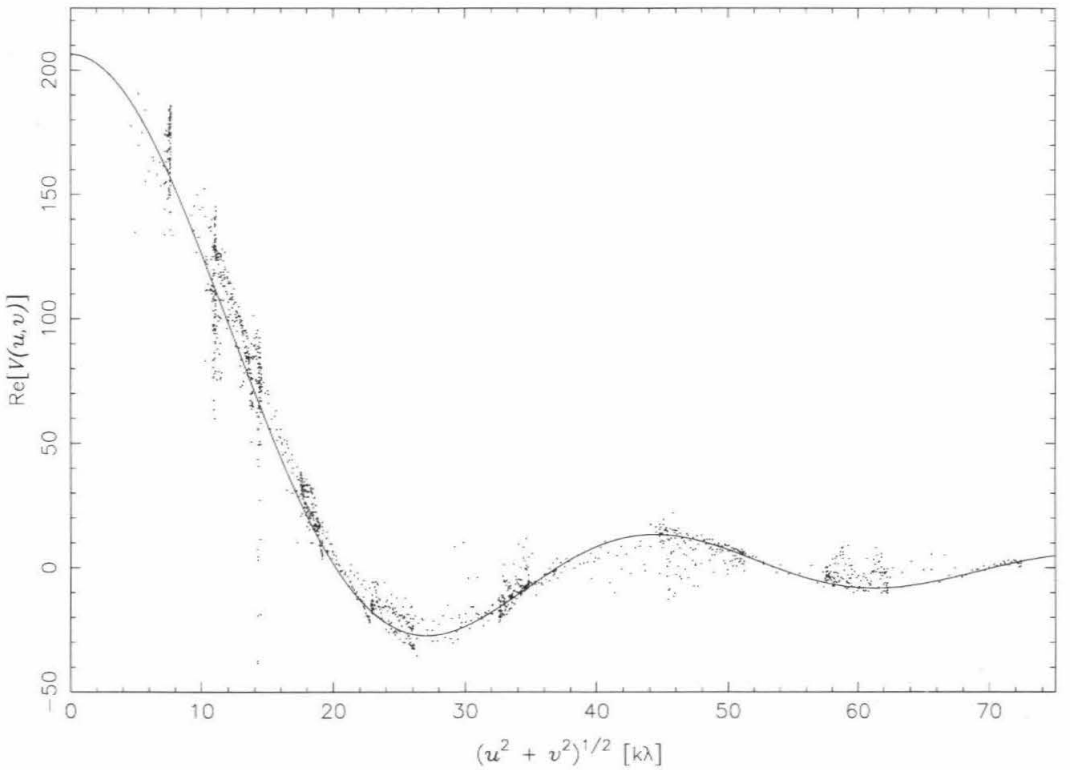

Figure 3.3. The real part of the 1527 continuum visibility points as a function of (u, v) distance. The solid line is a best fit model uniformly bright disk with a radius of 6.25″ and a total flux of 206.5 Jy.

disk at the phase center, with a radius of 6.25″ and a total flux of 206.5 Jy. The general shape of the observed visibilities follows the model to a fair degree, but many points differ by a large margin. These differences, especially for spacings less than 20 kλ, downweight the total flux estimate. Deviations from the model are due to a combination of true differences between the model and the source, calibration phase errors, atmospheric fluctuations, and noise. Here I refer to calibration phase errors as those due to use of a celestial source to calibrate the observations. The calibration source is separated from the main source on the sky and therefore observations will occur through different atmospheric paths. Generally, it is best to use a phase calibrator which is as close as possible to the source, as this will minimize calibration

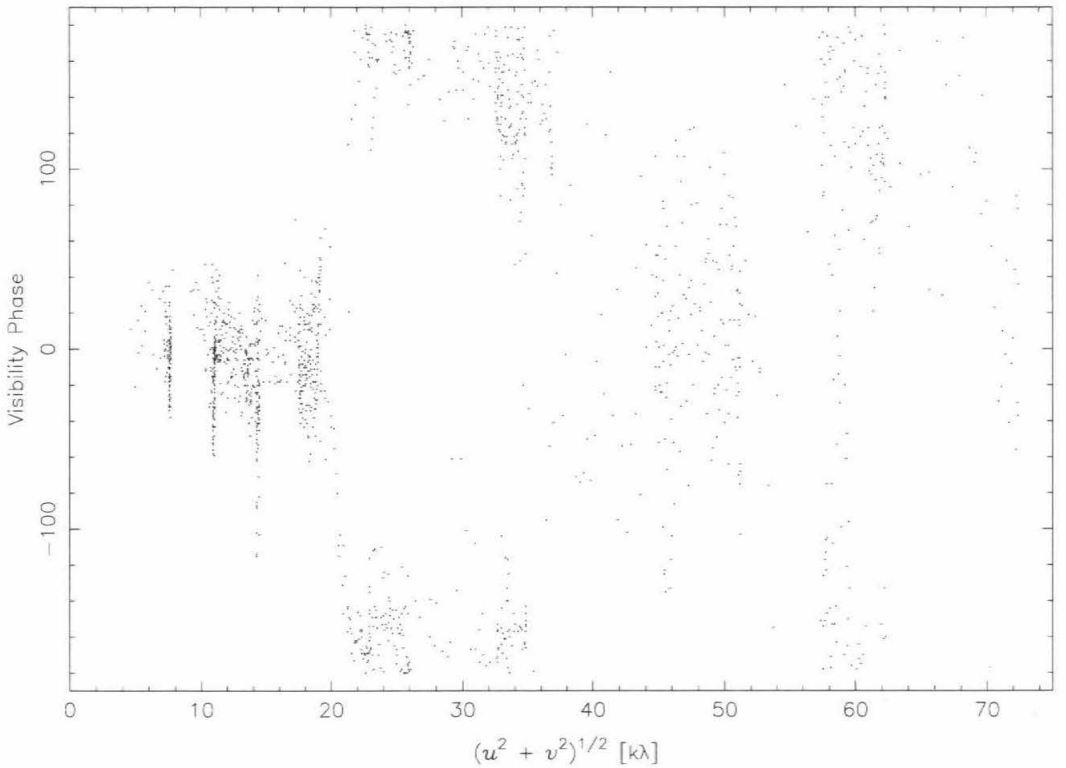

Figure 3.4. The phase of the 1527 continuum visibility points as a function of (u, v) distance. The large scale pattern is indicative of a resolved disk.

phase errors. However, an added consideration is the calibrator flux. Observation of a strong calibrator will minimize thermal noise on the phase measurement and allows shorter integration times. Usually, a balance must be struck between calibrator strength and distance from the source. For these observations 0528+134, nearly 22° away from Mars, was unfortunately the only adequate calibrator in the vicinity.

As discussed in Chapter 1, phase contains positional information. Phase errors will alter the sky brightness distribution estimated from the observations by "shifting" flux in a map away from its correct position. It is very important for this reason to calibrate the phase as best as possible. Figure 3.4 presents the calibrated continuum visibility phase as a function of (u, v) distance. For the model disk discussed earlier

the visibility function is real and the phase can only be 0 or 180° , with phase jumps wherever $V(u,v)$ passes through a null. The observed phases show a large scatter but do show such a trend. Despite the random appearance of the phase scatter, it is probable that most of the scatter was not due to measurement noise because Mars was a strong source and each integration was sufficiently long to measure the phase with good precision. Instead, most of the scatter was likely caused by short term variations in atmospheric phase delay above each antenna. The variations are due to fluctuating amounts of water vapor along the atmospheric path as local weather patterns moved over the OVRO site.

3.2.3 Phase Self-Calibration

An effective way to improve interferometer data is by application of phase self-calibration. Phase self-calibration attempts to correct phase errors introduced by variations in the phase delay of the atmosphere, an antenna based phenomenon. A discussion of phase self-calibration and its application to interferometric observations is provided in Chapter 1. For self-calibration to work effectively the source must be strong (to limit thermal noise contributions to the phase measurement) and its basic structure must be known *a priori*. Fortunately, Mars satisfied both these requirements.

The basic model used for Mars was a circular disk of total flux 226 Jy and radius 6.25″; unlike the uniform disk discussed above this model had higher intensity at the disk center than near the disk edge. The surface of Mars was modeled as a smooth dielectric sphere with the local surface emissivity equal to $1-R$, where R is the average of the Fresnel perpendicular and parallel reflectivities (see Appendix A). At high emission angles the surface emissivity drops, causing the thermal emission from Mars to appear limb-darkened. The model used for phase self-calibration assumed a surface dielectric constant of 2.5 to simulate the expected limb-darkening at high

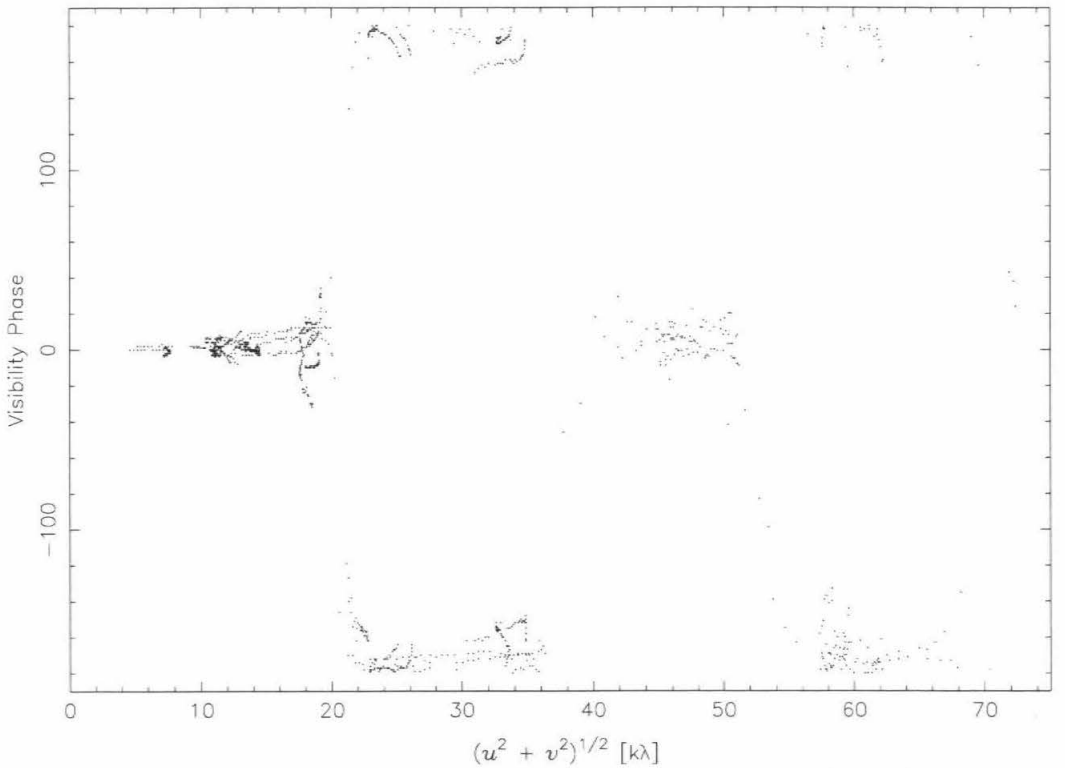

Figure 3.5. The phase of the remaining 1236 continuum visibility points as a function of (u, v) distance after application of self-calibration. The large scale pattern indicative of a resolved disk is much more clearly defined and the large phase scatter of Fig. 3.4 is substantially reduced.

emission angles.

Phase self-calibration uses the *a priori* model and closure relationships to solve for phase gains on each antenna as a function of time. It then removes the effects of these gains, flagging points which exceed set criteria. Phase self-calibration was applied with the resulting self-calibrated data set reduced to 1236 visibilities in the continuum and in each spectral channel, a reduction of roughly 19% in the size of the data set. Figure 3.5 presents the resulting visibility phases for the continuum channel after phase self-calibration. Note that large corrections have been applied, reducing the scatter seen in Fig. 3.4 substantially. The clustering of phase around 0

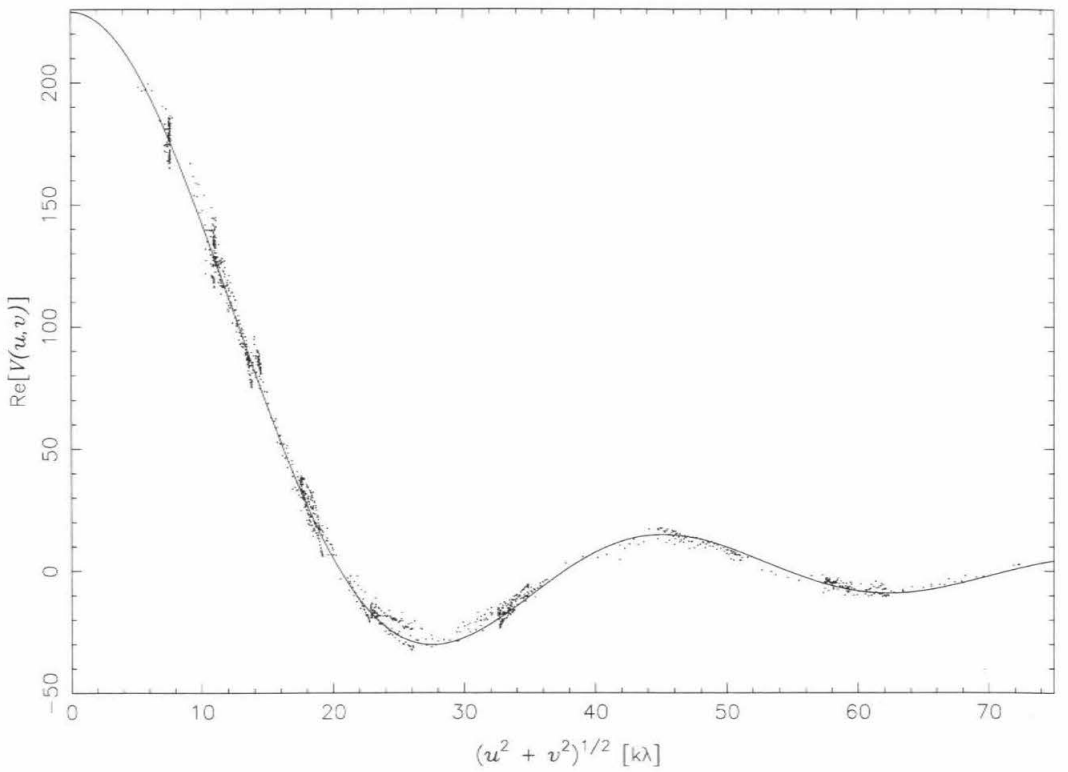

Figure 3.6. The real part of the remaining 1141 continuum visibility points after application of self-calibration and flagging of spurious points. The solid line is a best fit model limb-darkened disk with a radius of 6.25″ and a total flux of 228.5 Jy.

and $\pm 180°$ is now much more clearly defined. The large reduction in scatter vindicates the assumption that most of the phase errors were atmospheric in origin because they were removed so effectively with self-calibration.

After the application of phase gain solutions to the data set, the continuum visibilities were compared visually to a model visibility function, as in Fig. 3.3. The model visibility function was the same as that used for self-calibration: a limb-darkened disk of radius 6.25″ and total flux 226 Jy. There were 95 remaining points which deviated strongly from the model. These visibilities were flagged and removed, and the corresponding visibility points in the spectrometer data for the same baseline and time were also flagged.

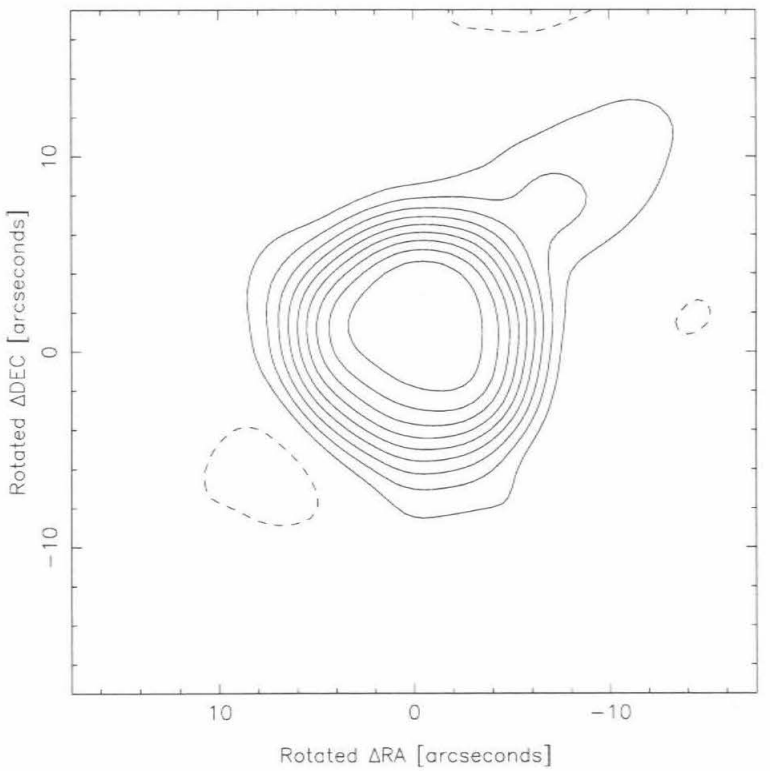

Figure 3.7. The clean map produced from the 1527 original visibility data points. The clean beam was 3.8″ at FWHM.

This final removal of spurious points resulted in a data set which included 1141 complex visibilities in the continuum channel and in each channel of the spectrometer data, or about 75% of the original data. The real component of the continuum visibility points are plotted in Fig. 3.6 as a function of (u, v) distance. Also plotted is a best fit limb-darkened disk visibility function of total flux 228.5 Jy, in good agreement with thermal model results. Comparison with Fig. 3.3 shows that after self-calibration the real visibilities are much more tightly contained and provide a better match to the model visibility function.

Maps of the sky brightness distribution are created through a process of numerical Fourier transformation of the visibility data and subsequent deconvolution

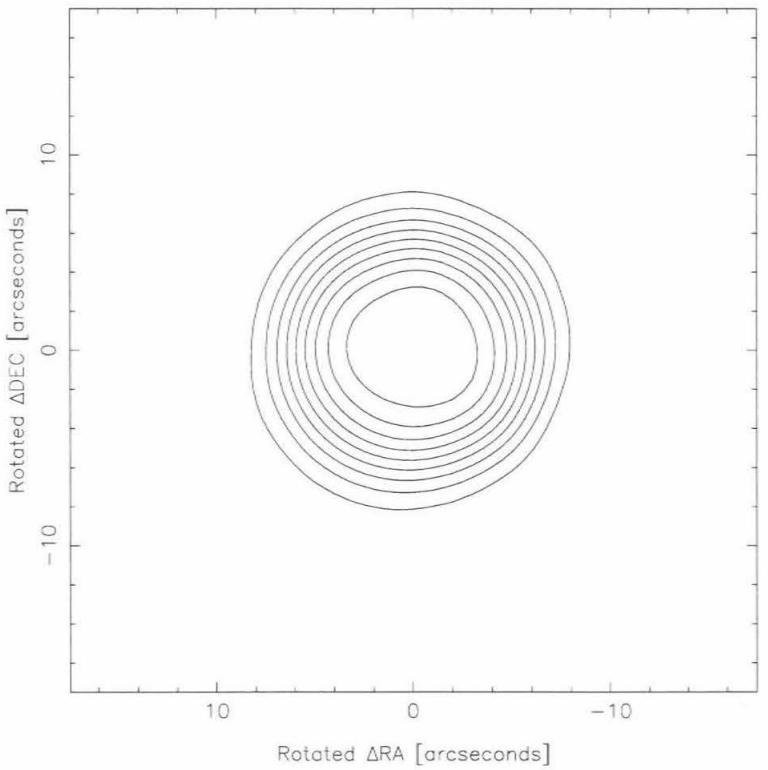

Figure 3.8. The clean map produced from the 1141 visibility data points remaining after self-calibration and flagging. The clean beam was 4.2″ at FWHM.

of the dirty beam. The brightness in the maps are given in units of Jy/beam; the map value at point (x, y) is essentially the flux that would be measured with a single antenna with a beam FWHM equal to the clean beam FWHM centered at that point. A description of the mapping and deconvolution process is given in Chapter 1. The effects of self-calibration on the mapped sky brightness of Mars are quite noticeable in cleaned (deconvolved) maps of the original continuum visibility data set and the self-calibrated visibility data set, shown in Figs. 3.7 and 3.8, respectively. The visibility data were rotated in (u, v) space prior to mapping and deconvolution so that the north pole of Mars is at the top of the figure. In both images the contours are at -10, 10, 20, 30, 40, 50, 60, 70, 80, and 90% of the peak flux in that image.

The improvement in the map of the sky brightness after application of self-calibration phase gain corrections is fairly dramatic in this case. In the image created from the non-self-calibrated data two notable anomalous features are the "tongue" of flux extending out from the disk and on the opposite side a region of *negative* flux. Due to the Fourier relation between sky brightness and visibility, negative flux is mathematically allowed in the image-plane. In this case both the positive and negative flux regions are due to phase errors in the measured visibilities. Both anomalous flux regions have been corrected out of the image obtained from the self-calibrated visibility data. Due to the reduction in the number of visibilities after self-calibration the dirty beam shape was different for each map. The synthesized beam of the self-calibrated map is 4.2″, somewhat larger than the 3.8″ beam of the original data. However, the small degradation in resolution is vastly outweighed by the substantial improvement in the self-calibrated image.

3.2.4 Observatory Software Errors

At the time the observations were made the OVRO interferometer was in the midst of a large upgrade. OVRO had consisted for nearly a decade of three antennas, but by January 1993 a fourth antenna had been installed and was being integrated into the array. Much of the observatory software had been created with a three antenna array explicitly in mind. As a result of the expansion the observatory initiated an overhaul of the systems controlling the array, including a generalization of the software to handle an N antenna array. Unfortunately, several errors in the software were introduced. A brief description of each of the errors is presented below.

Channel Offset. The OVRO digital spectrometers have within each band an even number of channels. By observatory convention spectrometer bands are centered evenly around the requested frequency, i.e., the tracked frequency should be centered between channels $N/2$ and $N/2+1$ of a N channel band, with N even. However, this

data set showed that the tracked frequency was actually centered in channel $N/2+1$ (a half-channel offset), although header information written to the OVRO database indicated that it was centered between channels. The offset was in channel space and therefore in frequency space the offset was dependent on the spectral resolution. Our observations included spectrometer data at 1 MHz and 62.5 kHz. Comparison of the spectra in frequency space using the header information resulted in a relative offset of the CO line center measured in each band of 468.75 kHz, or 7.5 of the high resolution channels! The problem was corrected by resetting the header information before analysis.

Frequency Tracking. All celestial sources exhibit relative (or line-of-sight) velocity to the interferometer. For tracking a particular spectral line this relative motion must be accounted for. The main term of this motion is the velocity of the source relative to the Earth's center. In addition, the motion of the interferometer relative to the Earth's center due to rotation must be accounted for. Our data set showed that the main term was correctly applied, but when observing planets the term for Earth rotation was neglected. The relative velocity of the interferometer due to Earth rotation in the direction of a source is approximately

$$v_{rot} = \frac{2\pi R_{\oplus}}{day}\cos(\Lambda)\cos(DEC)\cos(HA) \tag{3.3}$$

where $R_{\oplus}$ is the radius of the Earth, Λ is the observatory latitude, DEC is the source declination, and HA is the source hour angle (a function of time). For OVRO's latitude (37.25°) and Mars' declination ($DEC = 27°$) v_{rot} is $330\cos(HA)$ m s^{-1}. Figure 3.9 shows the magnitude of the error in frequency as a function of UT date for the observations on February 7. The error had the effect of shifting the position of the line center within the spectrometer band over the course of a track. For the 62.5 kHz resolution band this shift is roughly four channels. The data were corrected by

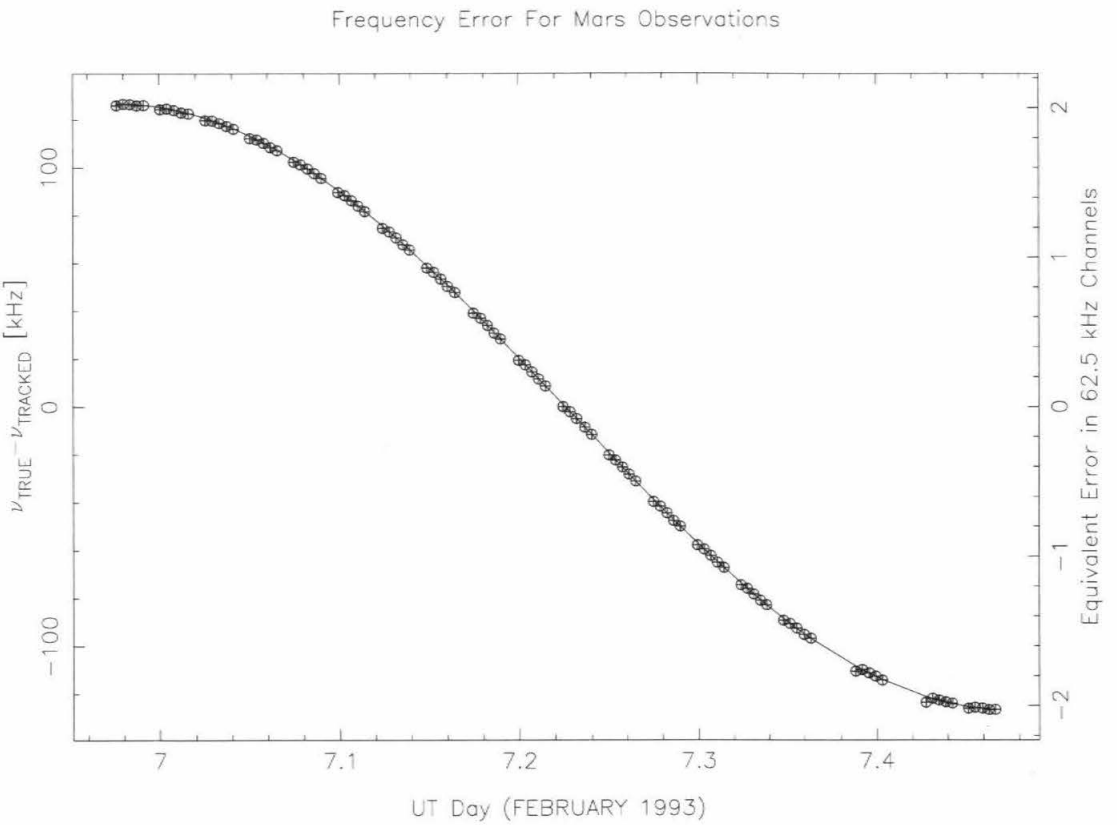

Figure 3.9. A plot of the frequency error introduced by neglecting Earth rotation in tracking the CO line frequency in the Mars reference frame. The $\oplus$ symbols mark the true frequency less the tracked frequency. The right scale gives the equivalent error in channels for the high resolution band.

shifting and interpolating the observed visibility spectra at each time onto a common grid before mapping and deconvolution.

Antenna Pointing. In April 1994 it was discovered that the pointing of the antennas was incorrect for planets. When a planetary source was observed its position was calculated with a 0.5 second error in time. The azimuth and elevation tracked by the antenna primary beams were therefore exactly 0.5 seconds of time in error. Therefore the primary antenna beams were centered $+7.5\cos(DEC)''$ in RA from the planetary disk center. For Mars this was a 6.7″ offset, and since Mars was only 6.25″ in radius the primary beams were pointed off the planet (this error affected only antenna pointing, not determination of the phase center).

The primary beam pattern determines the sensitivity of the array to extended sources–the true sky brightness of the source is weighted by the primary beam sensitivity. It is this weighted distribution that the measured visibilities correspond to. In the nomenclature of Chapter 1 (using $W(x,y)$ to denote the primary beam pattern):

$$V(u,v) = \int_{-\infty}^{\infty}\int_{-\infty}^{\infty} W(x,y)\, I(x,y)\, e^{-2\pi i(ux+vy)}\, dx\, dy. \tag{3.4}$$

The typical OVRO antenna has a primary main beam of $\sim 60''$ FWHM at 115.27 GHz. While the pointing offset was only a small fraction of the beam FWHM, the offset was significant enough to affect the observations. The beam offset weighted one side of the planet more heavily than the other, causing subtle errors in the brightness maps. Corrections are discussed in the sections dealing with inversion of the line shape.

3.2.5 The Spectral Image Cubes

After application of the phase self-calibration gain solutions found from the continuum channel and frequency interpolation to correct for neglected Earth rotation, the visibility data for each channel were rotated in (u,v) space to align the Mars north pole with "up" in map space. The spectrometer visibility data were then mapped and the effects of the dirty beam deconvolved in a manner similar to the continuum data. The total flux of the model disk was varied from channel to channel to match the disk average CO absorption line. The total flux of the model disk was determined from extrapolating the observed visibility function in each channel to a baseline of 0 m, providing an estimate for the "zero-spacing" (or whole disk) flux self-consistent with the data. Each channel was independently mapped and the dirty beam deconvolved, resulting in an image of the sky brightness of Mars in that channel. The resulting data set is composed of two spectral image cubes, one for the 1 MHz resolution data and one for the 62.5 kHz data.

Line to continuum ratio spectra from localized regions on the disk of Mars were created by taking the observed spectrum from a map pixel and dividing by the continuum flux of that pixel. Representative line to continuum spectra are provided in Figs. 3.10 and 3.11. Spectra have been plotted every $2'' \times 2''$, such that adjacent spectra in this image are not completely independent. The size of the clean beam FWHM is given by the thatched circle in the lower right. In each figure, the signal to noise is best near the disk center because the continuum level is highest there. These maps are oriented such that Martian north and south are at the top and bottom of the figures, respectively. The left edge corresponds to pre-dawn morning while the right edge to mid-afternoon Martian local time. The sub-earth point (disk center) is at 10:40 AM local time.

Examination of these figures reveals variation in the CO lineshape from different regions of the planet. In Fig. 3.10 (1 MHz spectra) there are three variations to note. First, the line to continuum spectra for morning hours (left half of the figure) feature broad emission features in the wings of the CO line and a relatively narrow absorption feature at the line center. The wing emission is strongest at the very left edge of the disk (and earliest local time). Spectra from the late morning and afternoon, in contrast, exhibit only absorption. Second, the spectra line centers show monotonically increasing depth from morning to afternoon across the entire disk; however, the linedepth measured relative to the highest point in the spectrum shows less variability. Third, the CO line is much weaker in the high southern latitudes than anywhere else.

Variations are also seen in Fig. 3.11 (62.5 kHz spectra). These spectra are of the CO line core, and therefore correspond to higher altitude emission than the 1 MHz spectra. At a total bandwidth of 7.5 MHz the lines exhibit only absorption. The absorption line appears fairly constant in shape for much of the disk, but the absolute

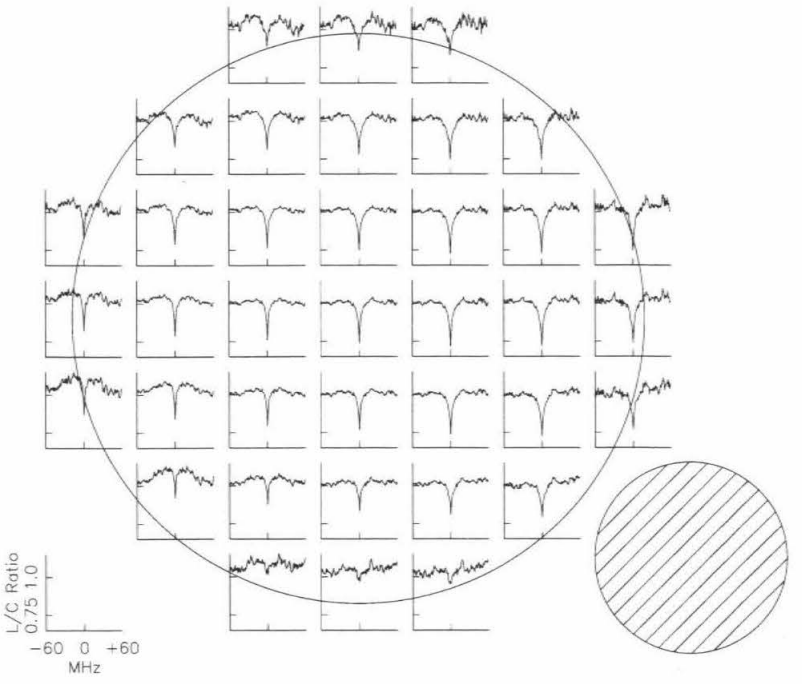

Figure 3.10. Spatially resolved line to continuum spectra at 1 MHz resolution. The thatched circle at the lower right represents the clean beam FWHM of 4.2″. Martian north is at the top of the page.

depth relative to the continuum shows the same monotonic increase from morning to afternoon as the 1 MHz spectra. Notable exceptions occur at northern and southern high latitudes, where the absorption is relatively weak. In particular, near the south pole there appears to be little absorption except in a remarkably narrow central core.

These variations in lineshape contain information on the temperature-pressure profile. Qualitatively, the presence of an absorption feature immediately shows that at least some portion of the atmosphere is colder than the surface brightness temperature. The emission wings seen for early morning hours are indicative of a lower atmosphere that is warmer than the surface brightness temperature. The weak spectral features near the southern pole suggests that the atmosphere is nearly isothermal

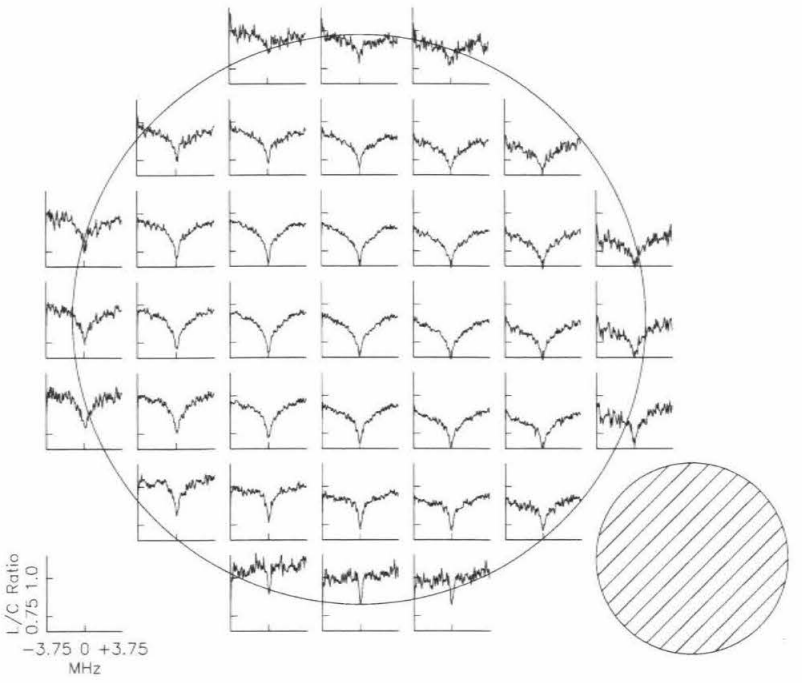

Figure 3.11. Spatially resolved line to continuum spectra at 62.5 kHz resolution. The thatched circle at the lower right represents the clean beam FWHM of 4.2″. Martian north is at the top of the page.

there. These differences in thermal profiles can be quantified through inversion of the CO lineshape. The numerical inversion of the spatially-resolved lineshapes can yield the vertical temperature of the Mars atmosphere from localized regions of the observed disk.

3.3. Modeling and Line Inversion

3.3.1 Radiative Transfer

The modeling of radiative transfer at microwave frequencies is straightforward. The processes involved in spectral line formation within an atmosphere are simple in relation to those at infrared or optical wavelengths. Aerosol scattering is negligible,

the effects of non-local thermodynamic equilibrium (non-LTE) are unimportant, and microwave spectral lines are well separated allowing individual transitions to be easily resolved.

Appendix A provides an overview of radiative transfer at millimeter wavelengths, including a development of numerical methods for the forward calculation of the radiative transfer equation. Of particular interest, the lineshape of a spectral feature can be related directly to the vertical temperature and absorber profiles of an atmosphere. The ^{12}CO $J(1-0)$ rotational transition provides substantial opacity in the Mars atmosphere within ~100 MHz of the rest frequency at 115.271204 GHz. There are no other important sources of opacity at these wavelengths in the Mars atmosphere.

Opacity due to carbon monoxide was modeled using the spectroscopic parameters of Pickett, Poynter and Cohen (1992). The $CO - CO_2$ collisional broadening coefficient for the CO $J(1-0)$ line was taken to be 3.3 GHz bar^{-1} at 300 K, with a temperature dependence of $T^{-0.75}$ (Varanasi 1975). The CO opacity for each model frequency and atmospheric layer was found by integrating the CO absorption coefficient times the Voigt lineshape (convolution of Doppler and collisional broadening) over the layer, as discussed in Clancy *et al.* (1983); a review is given in Appendix C.

The radiative transfer model utilizes a spherical atmosphere extending to 150 km above the surface, with layers of 1-5 km thickness. Free parameters include the temperature profile, surface pressure and temperature, and CO mixing ratio. The surface is taken to be a perfect sphere of radius 3395 km and dielectric constant of 2.5. The algorithm models the integrated flux at each frequency step measured by a gaussian beam of specified size and position on the disk of Mars (see Appendix D). This is accomplished by integrating the intensity along many raypaths ($\approx$ 50), including limb geometries. The actual number of raypaths is dependent upon the

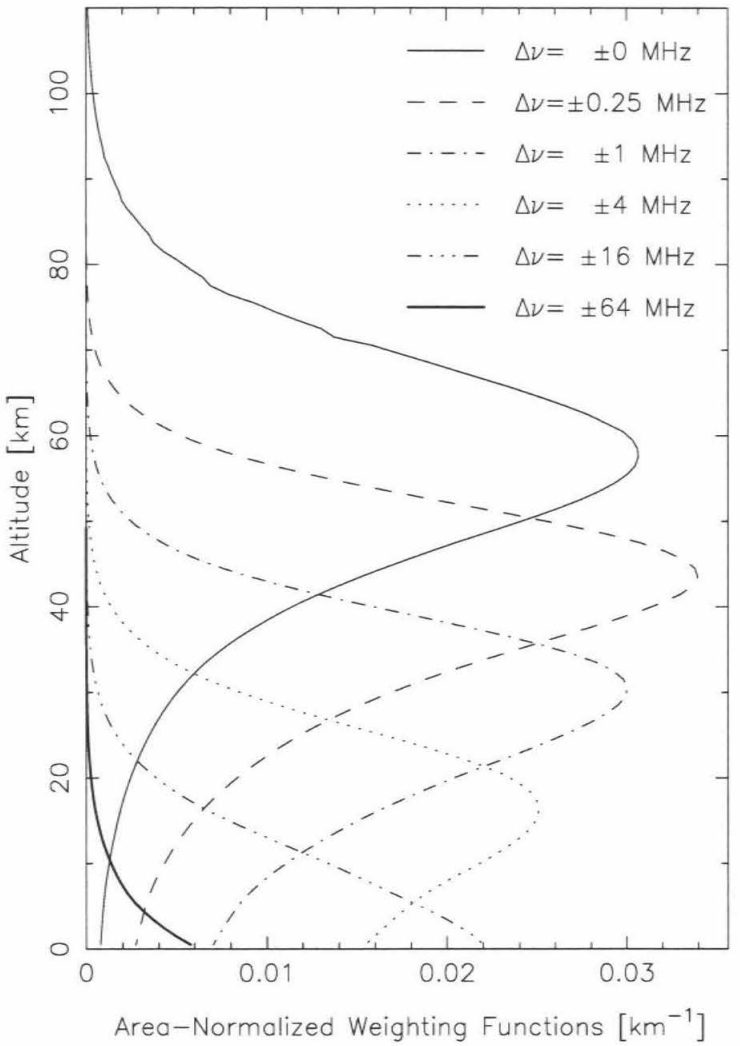

Figure 3.12. Weighting function profiles for the CO $J(1-0)$ line on Mars. Profiles are given as a function of frequency offset $\Delta\nu$ from the line center. Higher opacities closer to the line center lead to weighting functions which peak at higher altitudes.

size of the beam relative to Mars and its location. The results are interpolated and integrated to give the spectrum in units of flux density per beam.

Figure 3.12 provides model area-normalized nadir weighting functions for several frequencies near the CO line center. The weighting functions were determined using a Viking reference profile for temperature (Seiff 1978) and a uniform CO mixing

ratio of 8×10^{-4}. The weighting function peaks span the region from the surface to roughly 60 km. The nadir optical depth at the surface in the line center is 3.95, dropping to ~ 1 at ± 4 MHz from the line center. These weighting functions show that the 2.6 millimeter intensity is dominated by surface emission at frequencies far from the line. For frequency offsets closer to the line center the fraction of the emission originating in the atmosphere increases, until in the line center only the atmosphere effectively contributes to the observed intensity. Although the line center weighting function extends to over 100 km, the main contribution comes from altitudes below $\sim$70 km. The ^{12}CO $J(1-0)$ rotational transition can therefore be used to probe the vertical structure of the Martian atmosphere from 0 to roughly 70 km.

3.3.2 Spectral Line Inversion

The process of line inversion for atmospheric parameters, even at microwave frequencies, is complicated. The radiative transfer equation can be forward modeled explicitly, but the inverse process is generally ill-conditioned, in the sense that there are a variety of temperature and absorber profile combinations which can produce essentially indistinguishable spectra. However, given certain assumptions about atmospheric structure it is possible to numerically invert an observed spectral line for a temperature or absorber abundance profile consistent with the measurements. For observations of a single transition it is only possible to estimate one profile, but observations of two or three transitions (often including those of isotopes) can be used to estimate both profiles (Lellouch *et al.* 1989, Clancy and Muhleman 1990).

From the analyses described in the introduction it is likely that the temporal and spatial variability of CO on Mars is relatively modest. Therefore, in this work a CO mixing ratio of 8×10^{-4}, constant with latitude, local time, and altitude, has been adopted. This assumption allows the observed CO spectra to be inverted for local profiles of atmospheric temperature.

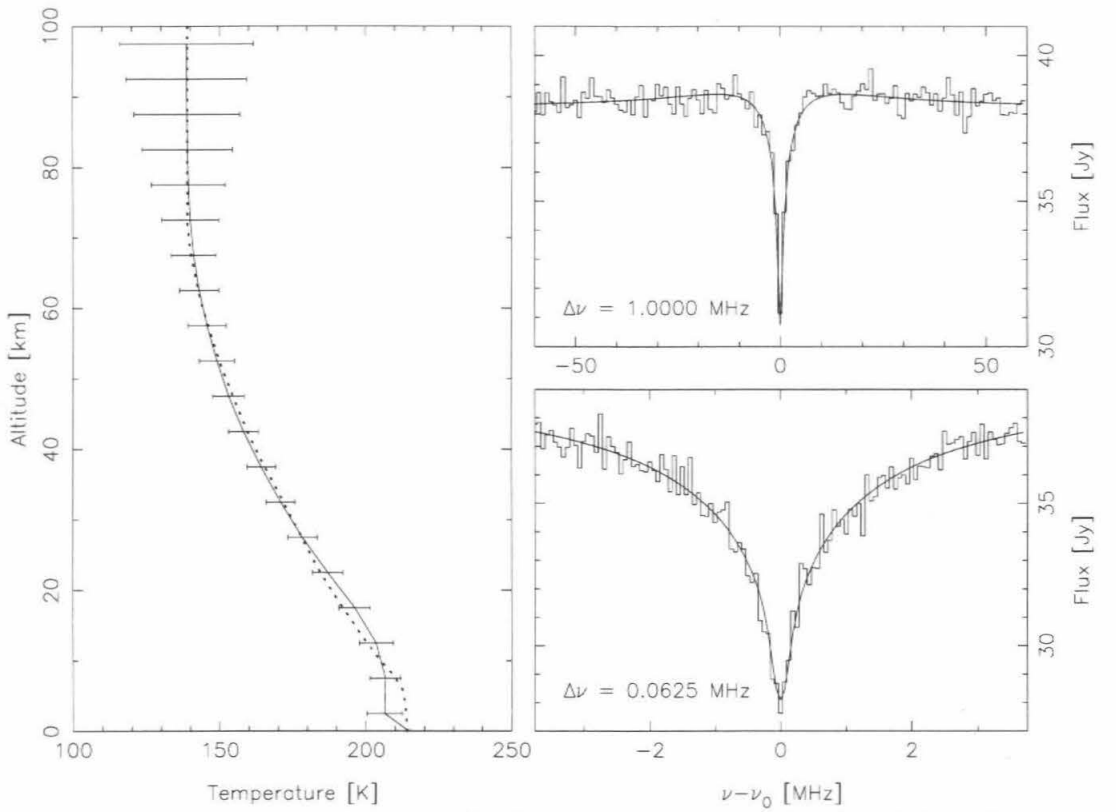

Figure 3.13. Solution temperature profile (solid line with error bars) and best-fit spectra for that profile. Dotted line is the input profile used to create the noisy spectra.

The CO lines obtained from the interferometric observations were inverted using a least-squares line inversion algorithm to quantify the local temperature profiles that best fit the observed spectra. Details of the least-squares inversion technique and its application to millimeter CO spectroscopy are given in Gurwell *et al.* (1995) and an overview is presented in Appendix F. In summary, to determine the best-fit temperature profile for a given spectrum, a model spectrum is first calculated using a reference temperature profile. In addition, the analytic partial derivatives of the spectral flux with respect to changes in the temperature profile (Appendix B) for each frequency channel are also calculated. The differences between the observed and calculated spectrum are used along with the partial derivatives to estimate changes

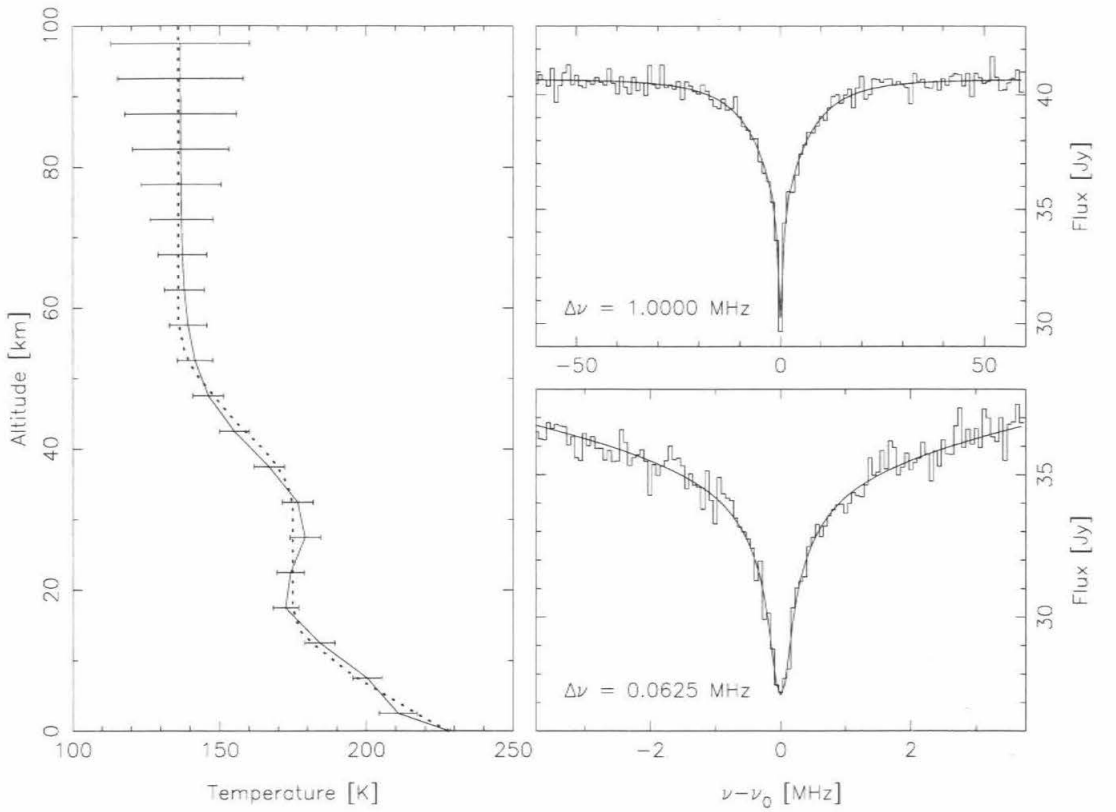

Figure 3.14. Solution temperature profile (solid line with error bars) and best-fit spectra for that profile. Dotted line is the input profile used to create the noisy spectra.

in the temperature profile that will better fit the observations. The radiative transfer equation is nonlinear, and it is necessary to iterate until a stable solution is reached.

Examples of numerical line inversions are given in Figs. 3.13 and 3.14. Model spectra at 1 MHz and 62.5 kHz with added gaussian random noise typical of the observed spectra were inverted; the derived temperature profiles and the true input profiles are plotted, along with the noisy and best fit spectrum in each band. The temperature was determined in 5 km steps from 0 to 100 km; the true resolution of the inversion is roughly one scale height (about 10 km). Error bars represent the formal error on the solution at each altitude determined from the covariance matrix from the final iteration.

The solution profiles provide good matches to the input profiles over most of the atmosphere from 0-100 km. However, as can be seen in the formal errors the sensitivity of the inversions are limited to below $\sim$ 70 km. Above this altitude the error estimates rapidly increase. The one region where solution profiles usually do not provide good fits is near the surface. As has been pointed out by Clancy and Muhleman (1990), the lowest scale height of the atmosphere is very difficult to sense effectively, due to the limited vertical resolution and uncertainties in the radiative properties of the surface.

Millimeter-wave whole-disk CO observations (e.g., Clancy *et al.* 1983, Clancy *et al.* 1990) have typically been analyzed by scaling the line to continuum spectrum by a model whole disk brightness temperature. Clancy *et al.* (1983) showed that for whole-disk measurements of the CO line the large variation in surface temperatures across the disk of Mars can be neglected as long as an accurate average surface brightness temperature is utilized. However, for spatially resolved observations such as those presented here the assumption of a single temperature for the surface will not work since variations in surface temperature are resolved in the measurements, and a more accurate approach is necessary.

One option is to use the absolute flux of each spectrum. However, absolute flux calibration is typically uncertain to at least 5%. A 5% error in the flux translates roughly to a 10–12 K uncertainty in the continuum temperature, which maps directly to a 10–12 K uncertainty in the derived temperature profile. In addition this data set was affected by antenna pointing errors which distort the absolute flux level as a function of position in the map. A rough estimate of this effect led to an estimated additional error of up to 12% for the afternoon edge of the disk, or about 25 K for the continuum temperature.

A better method is to scale the line to continuum spectra by a model of the

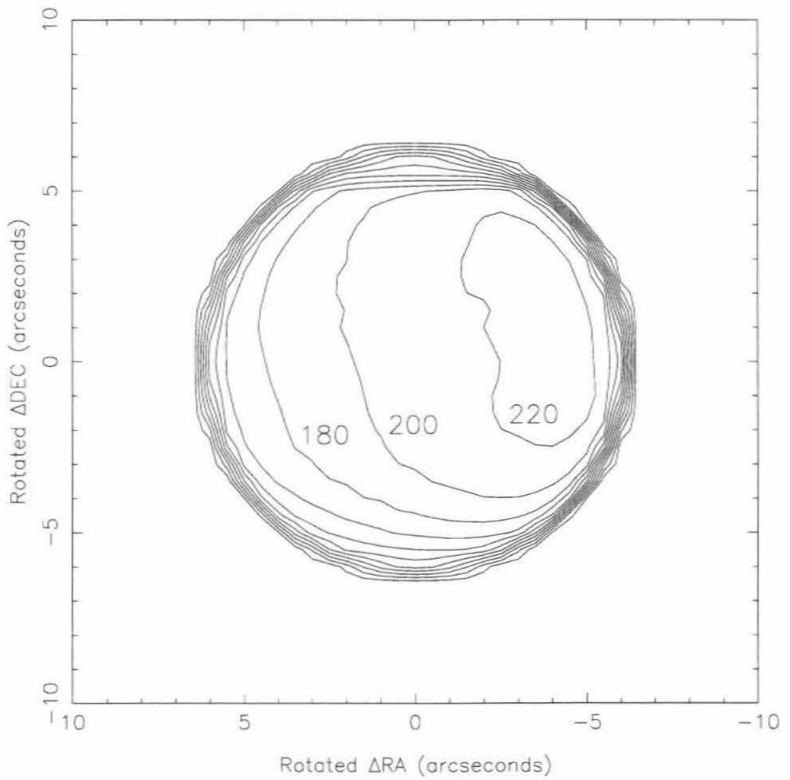

Figure 3.15. A map of model brightness temperatures at 2.6 mm for Mars at $L_S = 37°$; units are Kelvin. Contours are plotted in increments of 20 K. Note the falloff in emissivity at the limb. Martian north is at the top of the figure.

continuum brightness temperature, as for a whole disk spectrum. The model must be fine enough such that variations of the continuum brightness temperature with latitude and local time are resolved. The thermal model described by Rudy *et al.* (1987) fits these criteria. This model was run for $L_S = 37°$ and the appropriate sub-earth and sub-solar data for early February 1993. The dielectric constant of the Martian regolith was taken to be 2.5, and the radiative skindepth to be 10 wavelengths (or 2.6 cm). The result was a map of the equivalent brightness temperature of the Martian disk, shown in Fig. 3.15. Afternoon hours are significantly warmer than morning hours; the contrast from morning to afternoon exceeds 60 K. The North Polar Cap has a significant signature on the modeled millimeter brightness as well.

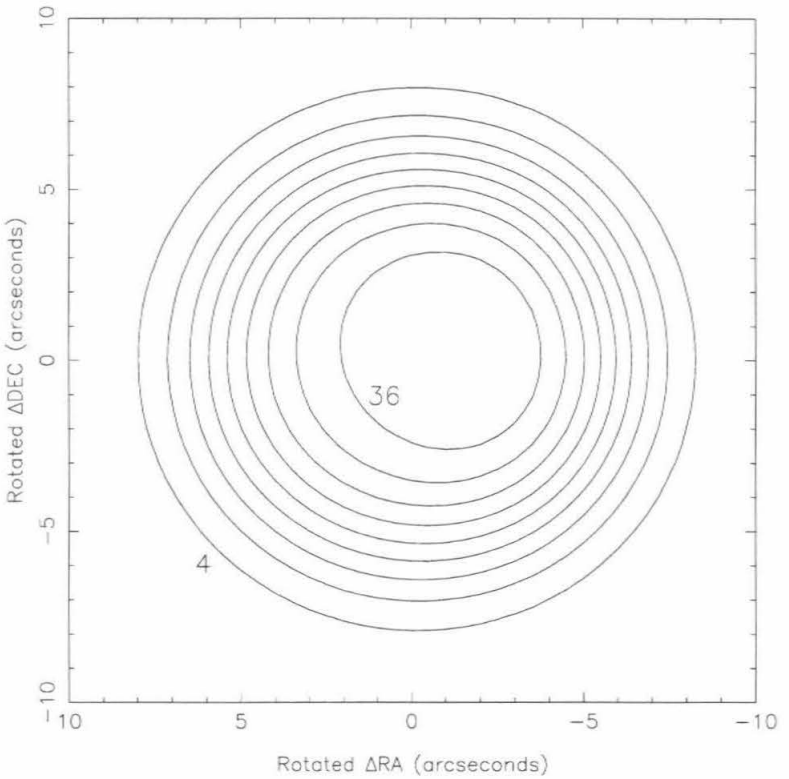

Figure 3.16. A map of model flux at 2.6 mm for Mars at $L_S = 37°$ convolved with a 4.2″ FWHM clean beam; units are Jy/beam. Contours are plotted in increments of 4 Jy/Beam and correspond roughly to increments of 5.2 K in beam averaged brightness temperature.

Note the fall off of brightness temperature around the limb caused by the decrease in surface emissivity at high emission angles.

The model brightness temperature map was convolved with a gaussian beam of 4.2″ FWHM and converted to flux units; results are shown in Fig. 3.16. Convolution vastly reduces the contrast between morning and afternoon, but it is still evident in the peak contours, which are shifted toward the afternoon limb. The signature of the polar cap has been reduced substantially and is evident only as a flattening of the contours in the north. This map was used to scale the observed line to continuum spectra to units of Jy/beam, appropriate for the line inversion algorithm.

In addition to the continuum scaling, each spectrum was assigned a base atmospheric pressure. A map of the expected Martian surface pressure as a function of latitude and longitude was calculated using a reference topography map (data available through the Atmospheres Node of the Planetary Data System archive; based on photogrammetry of Viking Orbiter images and earth-based radar altimetry [Wu 1979]) and the mean surface pressure at the Viking 1 lander site for $L_S = 37°$ (8.2 mbar). This map was averaged over 150° of longitude to account for Martian rotation during the observations. The appropriate surface pressure for each beam was then found by convolving a gaussian beam with the pressure map projected onto a disk representing the Martian geometry at the time of the observations.

3.3.3 Atmospheric Temperature Profile Solutions

Solution profiles of atmospheric temperature were found from the observed line to continuum spectra scaled by the model continuum flux. Stable solutions were usually found within 5 to 6 iterations of the least-squares inversion algorithm. The resulting profiles show remarkable variation with position on the disk of Mars.

Representative atmospheric temperature profile solutions derived from spectra sampled along the Martian equator are presented in Fig. 3.17. For comparison, a Viking reference temperature profile based on Viking 1 and 2 descent profiles is also shown (Seiff and Kirk 1977, Seiff 1978). In addition, a temperature profile based on whole disk millimeter-wave CO measurements made in mid-January 1993 is provided (R. T. Clancy, personal communication, 1995). The Viking reference and January 1993 profiles correspond to average conditions at low to mid-latitudes.

The most striking general feature of the solution profiles is that they are significantly cooler than the Viking reference profile at nearly all altitudes. The solutions are at least 15-20 K cooler than the reference profile from roughly 15 to 50 km. In particular the 5:40 AM solution is roughly 35 K cooler than the reference profile for

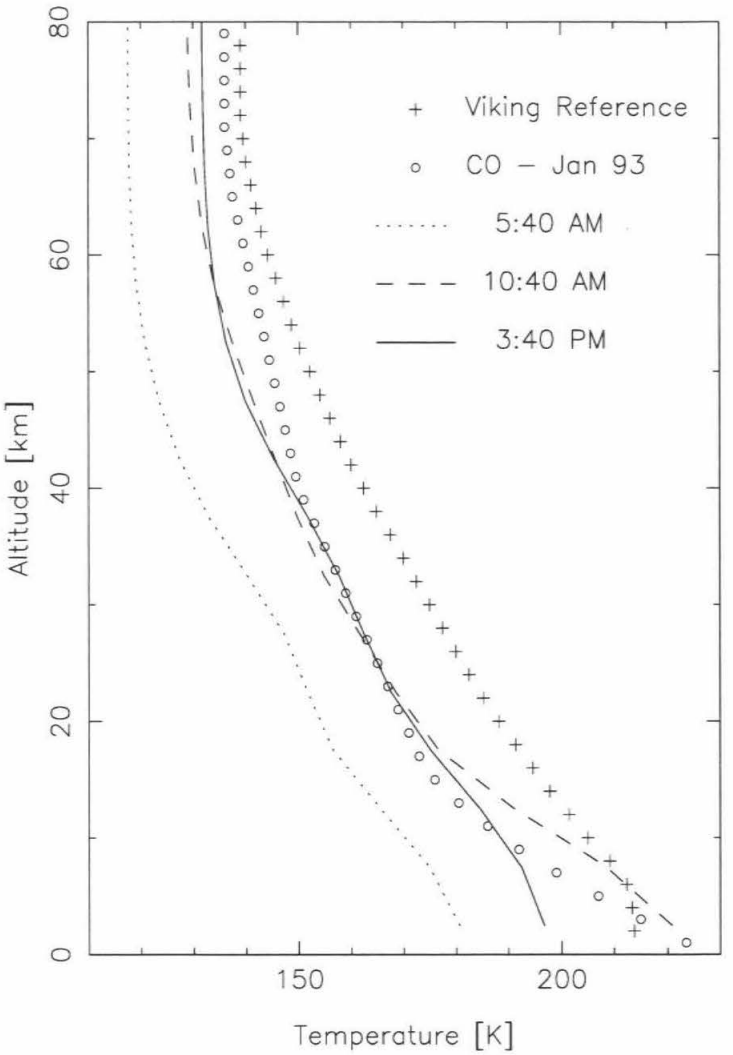

Figure 3.17. Solution profiles of temperature from equatorial spectra centered near the morning limb (5:40 AM), at the disk center (10:40 AM), and near the afternoon limb (3:40 PM). The Viking reference profile (Seiff 1978) is significantly warmer at most altitudes. The 10:40 AM and 3:40 PM solutions compare exceptionally well to the profile based on whole disk millimeter-wave CO measurements from January 1993.

altitudes less than about 50 km.

In the altitude range 0 to 50 km, the solutions at 10:40 AM and 3:40 PM are exceptionally consistent with the temperature profile from January 1993, determined from whole disk CO observations taken approximately 20 days earlier than the in-

terferometric observations. In the altitude range of 20 to 40 km they are virtually identical. The sub-earth point for the January observations was near noon Martian local time, and this measurement was therefore dominated by the average temperature at low to mid-latitudes and between 9 AM and 3 PM local time. The excellent agreement between the late morning and afternoon profiles from February and the average profile from January show that the Martian atmospheric temperature profile was relatively stable between the two observation periods. The interferometric observations do suggest that the atmosphere from 50-60 km may have been 7-10 K cooler in February than in January, but this is only marginally certain given the expected error for the solution profiles.

Clancy and Muhleman (1990) have made periodic, long-term millimeter-wave observations of CO on Mars in order to monitor variations in atmospheric structure (see also Clancy *et al.* 1993, Clancy *et al.* 1994). Generally, the average temperature profiles they find fall into two categories: profiles that are roughly comparable to those measured during the Viking era, and profiles that are distinctly cooler. The cooler profiles are in good agreement with radiative-convective equilibrium calculations of atmospheric temperature (Gierasch and Goody 1968, Pollack *et al.* 1979) below 30-40 km. The radiative-convective equilibrium models are characterized by a lack of aerosol heating; Pollack *et al.* (1979) showed that Viking-era temperature profiles were indicative of substantial heating by aerosols in the 10-50 km region. The implication of the colder temperature profiles of Clancy *et al.* (1990), the January 1993 profile and the solution profiles found in the work is that the Mars atmosphere was nearly dust-free at these times.

The pre-dawn solution profile is approximately 12 K colder than the late morning and afternoon profiles at all altitudes. This is somewhat surprising, as diurnal temperature variations above 5 km altitude are expected to be less than 10 K (Pollack

et al. 1979, Seiff 1978). However, temperature retrievals from Mariner 9 IR observations of CO_2 do show significant diurnal variation. Santee and Crisp (1993) analyzed Mariner 9 IRIS spectra from 1972 during relatively dust-free conditions ($L_S \sim 345°$, well after the major dust storm of the Mariner 9 mission). They showed that diurnal differences at low latitudes were 10-20 K in the 10 to 40 km altitude range at that time, and diurnal differences exceeded 60 K in the lowest scale height. Hence the 12 K variation seen from pre-dawn to late morning in this data set seems plausible. On the other hand, above 15 km all three equatorial solutions seem to be remarkably similar in structure; it could be argued that the 12 K difference is the result of incorrect modeling of the Martian brightness temperature for early to mid-morning local times. However, expected errors in the continuum modeling are roughly 5 K, so much of this difference is probably real and points to warming of the atmosphere from early to mid-morning local time.

The evolution from cold early morning to warmer late morning and afternoon temperature profiles is shown most completely in Fig. 3.18, where the retrieved temperature structure of the equatorial Mars atmosphere is given as a function of local time and altitude. This contour plot was generated from solutions for equatorial spectra sampled every 0.5″, spaced much finer than the clean beam FWHM. The plotted temperatures in some sense represent the true atmospheric temperature structure along the equator convolved with the beamsize. Therefore it is important to be cautious when examining the fine structure in this plot. However, some general observations can be made.

The trend in Fig. 3.18, especially for altitudes above 15 km, is for gradual warming of the entire atmosphere from dawn through the morning hours. Below 15 km the atmosphere appears to also warm from dawn through the morning hours, and then begins to cool. From the figure it appears that maximum temperatures are

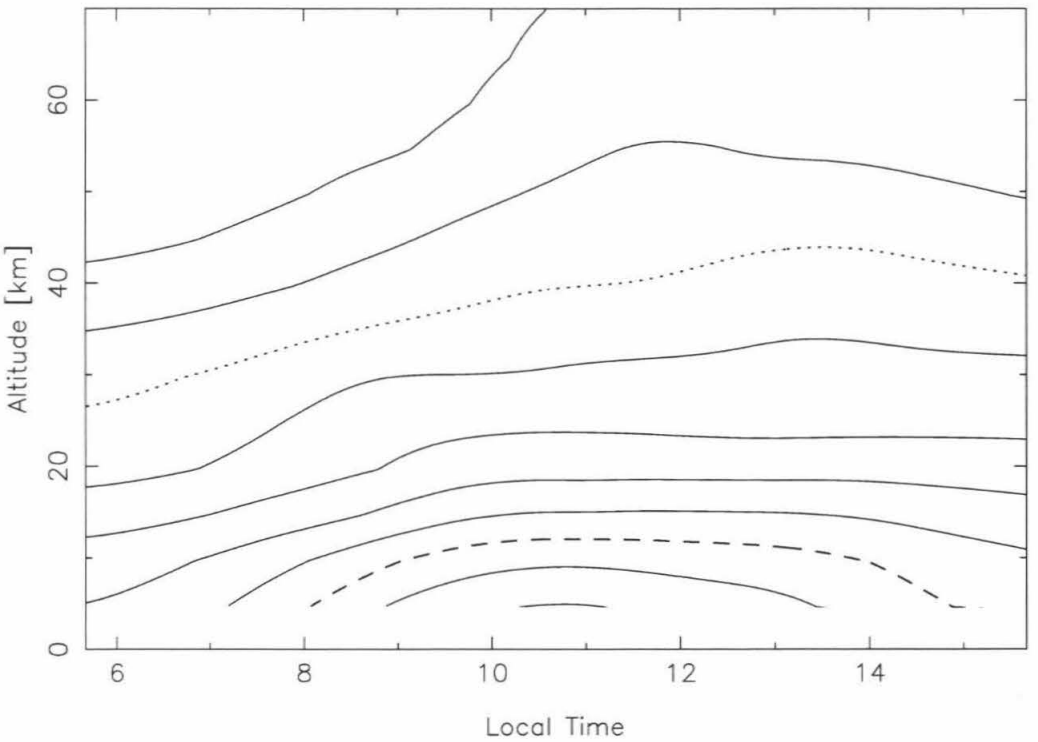

Figure 3.18. A contour plot of the retrieved temperature structure along the equator as a function of local time and altitude. Contours are spaced every 10 K, and the dotted and dashed lines correspond to 150 K and 200 K, respectively. The mean surface altitude relative to the 6.1 mbar reference level (0 km) is approximately 2.1 km along the equator. Solutions have been truncated below ~5 km.

reached *before* local noon, at roughly 11 AM local time. Caution is warranted here, as the temperature in the lowest scale height is usually difficult to properly retrieve. The exact local time of maximum temperatures is therefore uncertain.

While the retrieved temperature profiles show only modest variation with local time, they do show significant variations of structure with latitude. Figure 3.19 presents solution profiles for three spectra centered at the sub-earth local time (10:40 AM) near the south pole, equator, and north pole. The Viking reference profile is also plotted, and again we see that atmospheric temperatures for February 1993 are significantly colder at all altitudes.

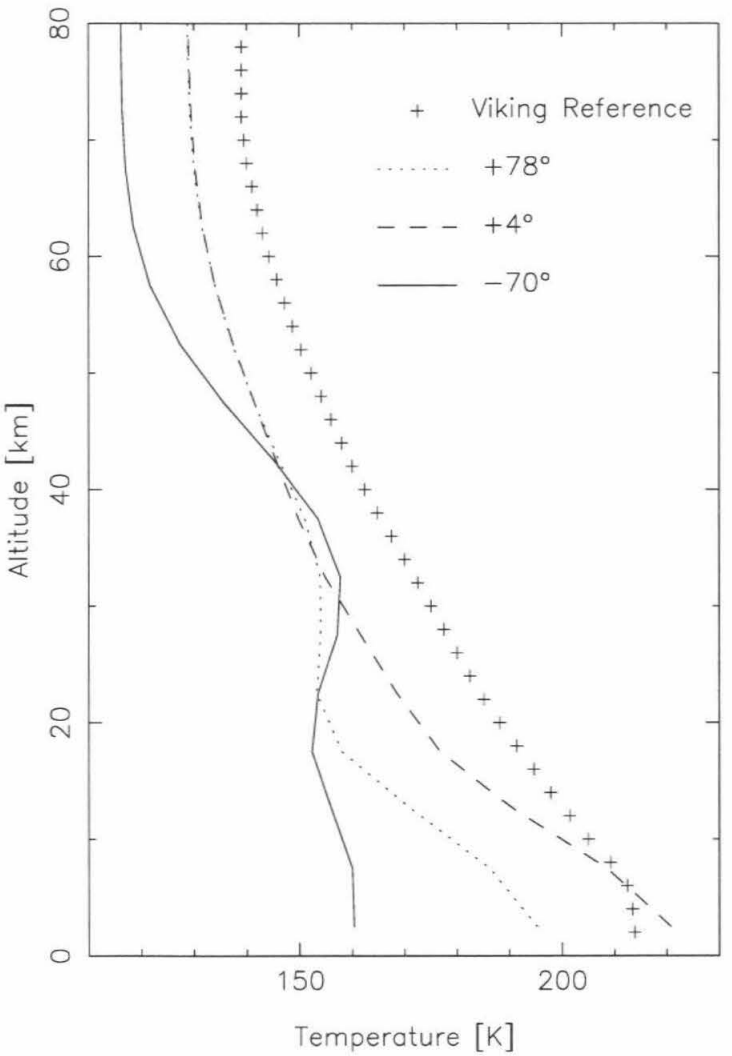

Figure 3.19. Solution profiles of temperature from sub-earth local time (10:40 AM) spectra centered near the south pole (−70°), at the disk center (+4°), and near the north pole (+78°). The high latitude profiles are isothermal over a significant range of altitude.

Relative to the low latitude solution, the profiles at high latitudes are distinctly colder below approximately 30 km. Both high latitude temperature profiles are nearly isothermal for significant altitude ranges. The southern profile in particular exhibits less than 10 K variation from the surface to ~35 km. The northern profiles is isothermal from roughly 20 to 40 km. The effects of the isothermal southern profile can be

easily seen in the line to continuum spectra near the southern pole (Figs. 3.10 and 3.11). These spectra were noted for extremely weak CO absorption features, which imply little variation in the atmospheric temperature profile. The narrow absorption cores of these spectra (see Fig. 3.11) are indicative of the significantly cooler upper atmospheric temperatures found above $\sim$ 40 km.

Both previous observational data and atmospheric modeling support the presence of nearly isothermal temperature profiles near the poles for particular ranges of L_S. Analyses of Mariner 9 IRIS spectra from $L_S \sim 345°$ (Santee 1993, Santee and Crisp 1993) show that during late southern summer the northern mid- to high latitudes exhibited nearly isothermal temperature to at least 40 km, while the southern high latitudes showed a negative temperature gradient from the surface to roughly 15 to 20 km with isothermal regions above that. Temperature profiles from Mariner 9 IRIS spectra from mid-northern spring ($L_S \sim 44°$) were found to be roughly isothermal for southern mid- to high latitudes (Leovy 1982, based on data provided by B. Conrath and the Mariner 9 IRIS team).

Martian atmospheric thermal forcing and dynamics have been modeled extensively with the NASA Ames General Circulation Model (Pollack *et al.* 1990, Haberle *et al.* 1993, Pollack *et al.* 1993). For essentially any model dust opacity, the Ames GCM calculates nearly isothermal temperature structure for mid- to high latitudes in the fall/winter hemisphere. This compares very favorably with the observational evidence described above. A model run for relatively low opacity and northern mid-spring shows not only isothermal regions for the southern mid- to high latitudes but an additional roughly isothermal region from the surface to 25 km for northern latitudes above 70° (Haberle *et al.* 1993). The February 1993 results of this work are very similar for the southern high latitudes, exhibiting nearly isothermal behavior to 40 km. The northern high latitude solutions are less well matched to the GCM

results, with the February 1993 data indicating isothermal temperatures from 20 to 40 km, not from the surface to 20 km. These solution profiles do, however, compare very well to the Mariner 9 IRIS results of Santee and Crisp (1993) for southern (i.e., summer) hemisphere high latitudes for $L_S \sim 345°$.

Above 40 km the northern and equatorial temperature profiles are indistinguishable, but the southern profile is cooler by roughly 12 K. Again this is corroborated by both GCM modeling and observations. Both show that the coldest temperatures in the atmosphere occur over the fall/winter polar region. From Fig. 3.2 we see that the southern pole is in perpetual shadow for this L_S, while the northern pole receives essentially constant sunlight. Radiative warming of the surface and atmosphere in the spring/summer polar regions produce significantly warmer temperatures below 20 km relative to the fall/winter polar regions, which receive minimal solar insolation.

The complex latitudinal variation of the Martian atmospheric temperature profile with latitude is shown more fully in Fig. 3.20, where a contour plot of the temperature structure for 10:40 AM is presented. The figure extends from $-70°$ latitude to $+80°$ latitude, and clearly shows the striking variation of the temperature profile from the southern high latitudes through the warm tropics to the northern high latitudes. As with Fig. 3.18, caution is needed in interpreting fine scale variations in the plot due to the coarse resolution of the observations.

The warmest temperatures retrieved are in the lowest scale height and centered northward of the equator. This northward maximum is expected for two reasons. First, the sub-solar latitude at this time was roughly 15° N and northern low latitudes therefore receive the greatest direct insolation. Secondly, the topography of Mars is lower on average in the northern hemisphere. The negative lapse rate of the lower atmosphere (see Fig. 3.19 for example) means that on average the lower lying northern hemisphere will experience slightly warmer temperatures for a given temperature

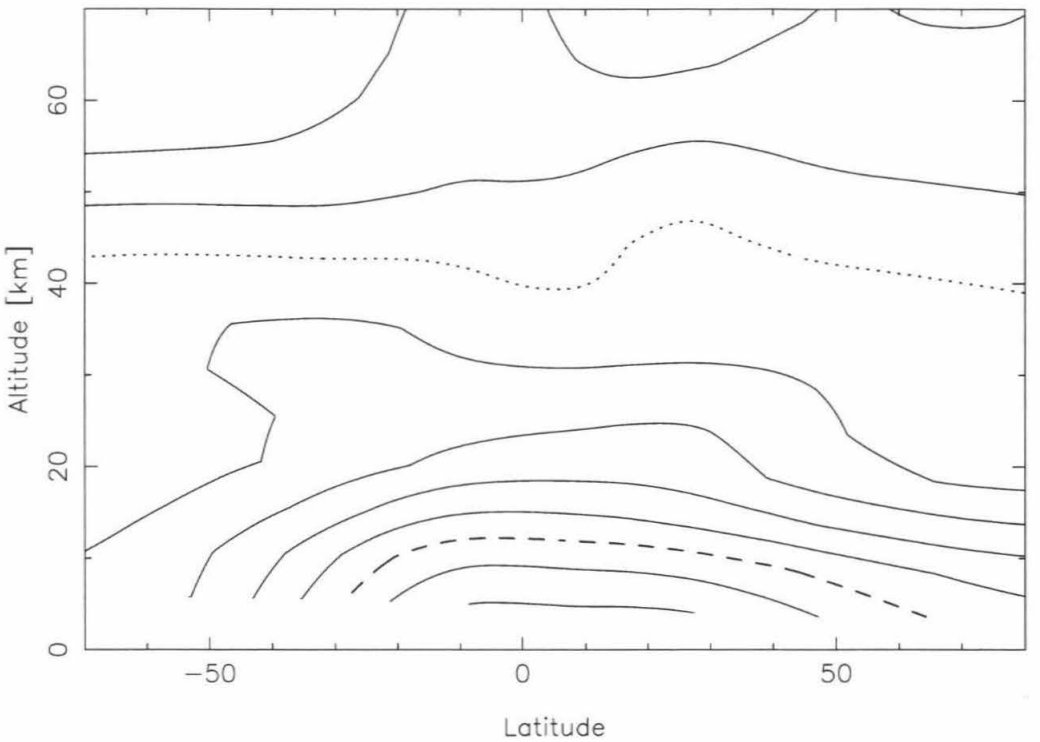

Figure 3.20. A contour plot of the retrieved temperature structure along the sub-earth local time (10:40 AM) as a function of latitude and altitude. Contours are spaced every 10 K, and the dotted and dashed lines correspond to 150 K and 200 K, respectively. Solutions have been truncated below ~5 km relative to the mean 6.1 mbar reference altitude.

profile referenced to the mean surface altitude.

The southern high latitudes are roughly isothermal to 40 km, with temperature variations less than 20 K for latitudes poleward of $\sim -55°$. In contrast, the northern high latitudes exhibit a falloff of temperature with altitude from the surface to about 20 km altitude. From roughly 40 to 60 km the atmosphere appears to be roughly uniform with latitude. The very coldest regions are above 60 km in the southern hemisphere.

Despite limited spatial resolution, these results show clearly that the latitudinal variation of temperature below 70 km in February 1993 was qualitatively similar

to the structure derived from Mariner 9 observations of CO_2 spectra and to detailed GCM results (Leovy 1982, Santee 1993, Santee and Crisp 1993, Haberle *et al.* 1993). The mean temperature, however, was significantly cooler than that found during the Viking and Mariner 9 eras, indicating significantly less dust in February 1993 and corroborating unpublished results from January 1993 CO measurements (Clancy *et al.* 1990, R. T. Clancy, personal communication, 1995). Hence it appears that the temperature structure versus latitude remains qualitatively the same under different dust loading conditions, but that the absolute temperatures vary. This result has been anticipated with the Ames GCM, which shows that the winter pole remains the coldest part of the atmosphere under a variety of dust opacity conditions (Haberle *et al.* 1993).

3.4. The Gradient Thermal Wind

Although the low spatial resolution prevents examination of the finer variations of the temperature field, these measurements provide the first resolved observations of the atmospheric temperature structure since the Viking era. The ability to retrieve the average atmospheric temperature from independent local time and latitude regions is of great importance for continued study of the Martian atmosphere and its response to solar forcing and dust loading.

Meridional profiles of temperature (i.e., as a function of latitude) are of particular interest because of the information they can provide on zonal winds (Zurek *et al.* 1992). On a global and regional scale temperature, wind, and surface pressure are closely related. Given observations of the temperature structure as a function of pressure (or altitude) the variation of the so-called balance (or thermal) winds can be computed. More precise details and derivations are available in review articles (e.g., Zurek *et al.* 1992) or textbooks (e.g., Houghton 1986 or Holton 1992).

For a purely zonal flow that is steady and frictionless the primitive equations

governing atmospheric motion on a rotating planet can be reduced to

$$\frac{u^2 \tan\phi}{a} + fu = -\frac{1}{a}\frac{\partial\Phi}{\partial\phi}, \tag{3.5}$$

where u is the mean eastward zonal wind, a is the mean planetary radius, ϕ is the latitude, f is the Coriolis parameter $2\Omega\sin\phi$, Ω is the angular rotation of the planet, and Φ is the geopotential:

$$\Phi = \int_0^z g\, dz, \tag{3.6}$$

with g the gravitational acceleration. Equation 3.5 is a differential form of the thermal wind equation. The zonal flow described in Eq. 3.5 provides a three-way balance between centrifugal, Coriolis, and meridional pressure gradient forces.

The derivative of the geopotential with respect to latitude is directly related to the meridional temperature structure. Converting to pressure coordinates, defining a reference level p_s, and using the hydrostatic equation the relative geopotential derivative can be described by

$$\left.\frac{\partial\Phi}{\partial\phi}\right|_p - \left.\frac{\partial\Phi}{\partial\phi}\right|_{p_s} = \int_{p_s}^{p} R\left(\frac{\partial T}{\partial\phi}\right)_{p'} \frac{dp'}{p'}. \tag{3.7}$$

Here R is the gas constant for the atmosphere. The reference level is often taken as the surface, but can be any level where the pressure and geopotential are known (or can be prescribed). If the surface is chosen as the reference level, it is usually assumed that the derivative of the geopotential at the surface is zero unless other data can be supplied. Note that this is equivalent to specifying that the zonal wind speed u is zero at the reference level. In this case the thermal wind equation becomes

$$\frac{u(p)^2 \tan\phi}{a} + fu(p) = -\frac{1}{a}\int_{p_s}^{p} R\left(\frac{\partial T}{\partial\phi}\right)_{p'} \frac{dp'}{p'}. \tag{3.8}$$

Equation 3.8 is the gradient thermal wind equation; it clearly shows the dependence of the mean zonal wind at pressure level p on the meridional temperature gradient. From it mean zonal winds can be deduced if the mean meridional temperature structure of

the atmosphere is known. The first term on the left hand side is due to centrifugal acceleration of air parcels when curvature of the surface is important, and in some cases it can be neglected (the resulting linear equation for $u(p)$ is then called the geostrophic thermal wind equation). However, for Mars neglect of this term may not always be valid (Santee 1993).

The gradient thermal wind equation requires that the average temperature structure be known. The thermal temperature profiles derived from the CO observations of February 1993 cover the observed disk of Mars, or most of the daylit hemisphere, with a small crescent of the pre-dawn nightside. This data set cannot provide the global mean meridional temperature structure for that time. However, the mean meridional temperature can be approximated by an average of the observations at each latitude. This average will be biased since most nightside local times are neglected. However, the dayside average can provide a rough estimate of the mean structure, especially above 20 km where diurnal variations are expected to be less than 20 K based on Mariner 9 IRIS measurements (Santee and Crisp 1993).

The average meridional structure of the atmosphere of Mars derived from the February 1993 observations of CO is shown in Fig. 3.21 as a function of pressure. Similar caution about interpreting the finer structure (as with Figs. 3.18 and 3.20) applies here as well. The structure is qualitatively similar to that shown in Fig. 3.20, but the temperatures at nearly all heights are roughly 10 K cooler. The roughly isothermal character at high southern latitudes is still evident, and the highest temperatures are not surprisingly still found in the lowest part of the atmosphere near the equator. Note, however, that above 0.3 mbar this reverses and a local temperature minimum occurs near the equator at most altitudes.

The meridional temperature structure shown in Fig. 3.21 was used to derive mean zonal circulation using the gradient thermal wind equation. The surface was

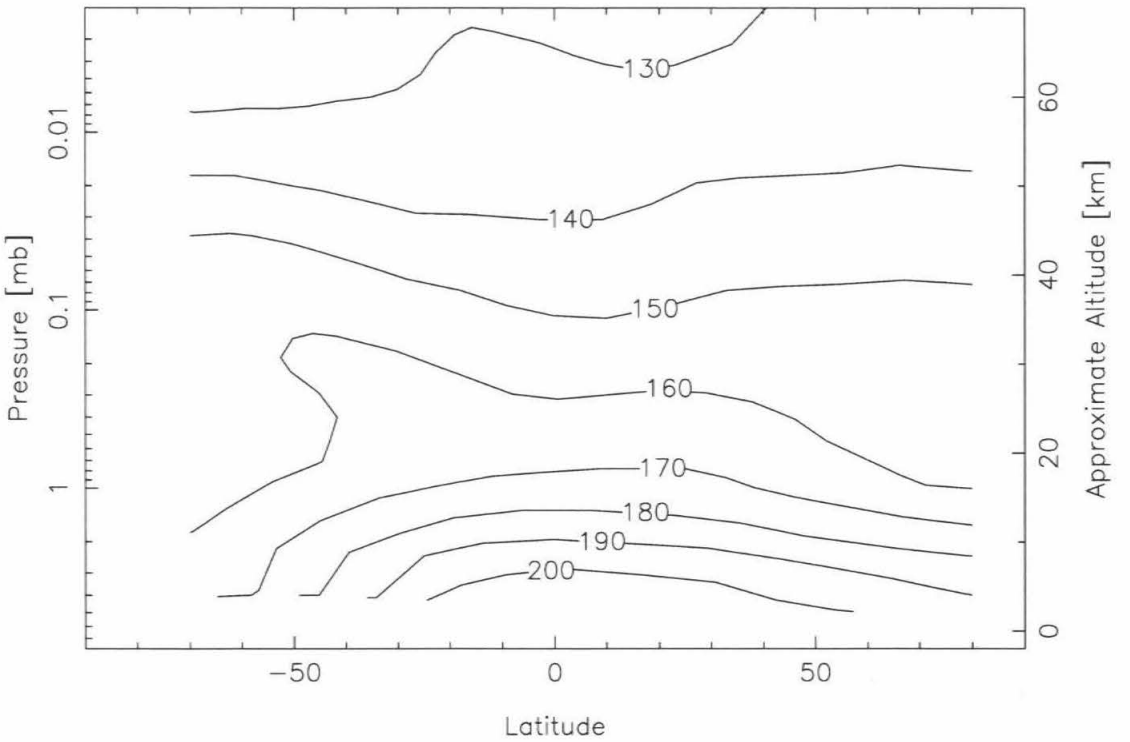

Figure 3.21. The average meridional temperature structure of the Martian atmosphere derived from the February 1993 interferometric observations of CO. The vertical coordinate is $\log_{10}$pressure, and approximate altitude relative to the 6.1 mbar reference level is given on the right axis.

chosen as the reference level and surface winds assumed to be zero. The resulting zonal winds are presented in Fig. 3.22 as a function of latitude and pressure. The wind field near the equator, where the Coriolis parameter approaches zero and zonal winds are not well constrained by the thermal wind equation, has been omitted.

One of the characteristics of the thermal wind equation is that zonal winds increase in strength with altitude in the presence of equator-to-pole temperature gradients. This can be seen in the derived wind field, where both the northern and southern hemispheres show the development of eastward jets. These jets are due to the temperature drop from the equator to the pole in each hemisphere. Below roughly 0.3 mbar (20 km) the temperature drop is steeper in the southern hemisphere, so the

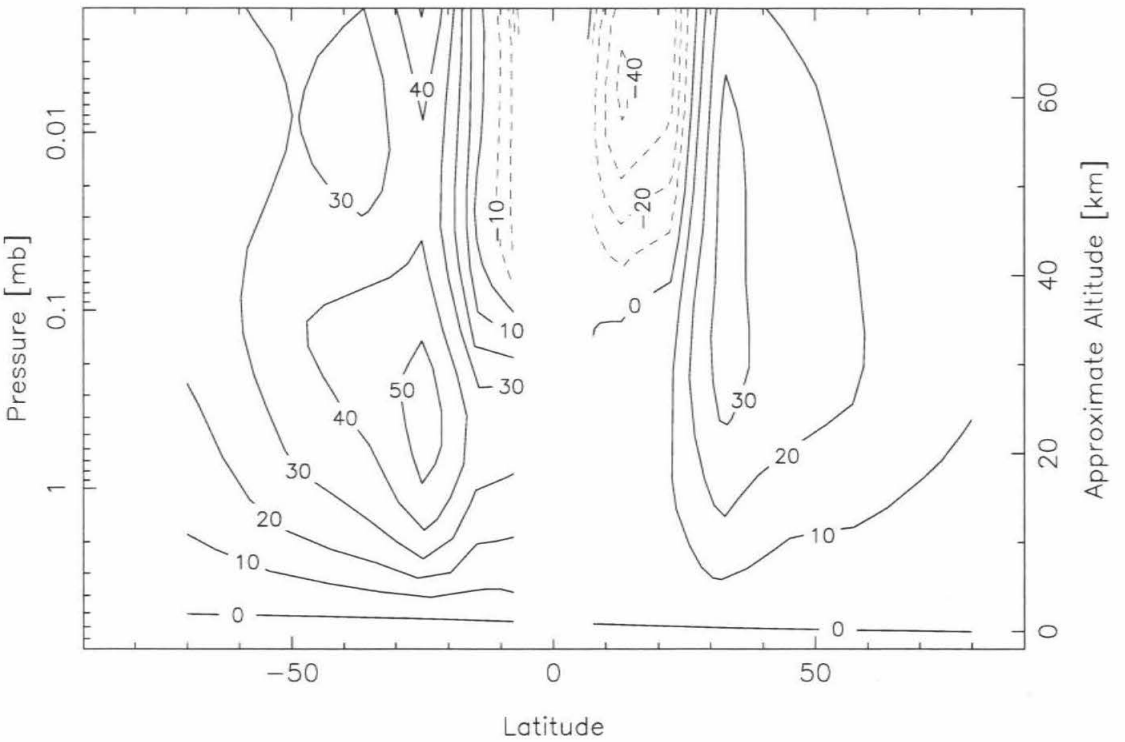

Figure 3.22. The mean zonal wind inferred from the temperature structure of Fig. 3.21. Velocities are in m s^{-1}, with positive (solid contours) indicating eastward winds and negative (dashed contours) indicating westward winds.

jet is stronger in the south. These eastward zonal winds persist at nearly all altitudes.

The southern jet reaches a maximum speed of greater than 50 m s^{-1} at roughly the 0.3 mbar level. Below 0.3 mbar there is a strong negative equator-to-pole gradient in temperature, allowing the jet to develop poleward of −15°. From about 0.3 to 0.01 mbar the temperature gradient becomes positive and zonal winds decrease in strength with altitude in this region. Above 0.01 mbar the gradient again switches sign and winds increase.

The northern jet reaches a maximum speed of greater than 30 m s^{-1} near 0.2 mbar. Below 0.2 mbar there is an equator-to-pole drop in temperature, similar but not as steep as that for southern latitudes, allowing the jet to develop poleward of

roughly 25° . Above that level the temperature gradient from equator-to-pole becomes slightly positive, and unlike in the south appears to remain so to above the altitude limit of the observations ($\sim$ 70 km). The northern jet therefore spans an extremely broad range in altitude with nearly constant velocity.

At northern low latitudes above 0.1 mbar a westward (retrograde) zonal jet develops, reaching a maximum velocity of $-40\,\mathrm{m\ s^{-1}}$ above 0.01 mbar. This jet is a response to the fairly steep positive equator-to-pole temperature gradient in this region. The southern low latitudes also hint at retrograde zonal flow above 0.1 mbar. However, the dependence of the zonal wind on $\cot\phi$ means that the inferred velocities are much more susceptible to small errors in the temperature gradient near the equator. For this reason the presence of retrograde zonal flow near the equator is only marginally certain.

There is observational evidence, however, that a retrograde zonal flow did exist at these altitudes. Measurements of the ^{12}CO $J(2-1)$ rotational transition were made with IRAM 30-m radiotelescope on December 29, 1992 – January 2, 1993, corresponding to $L_S = 19°$ (Lellouch *et al.* 1993, Gillet and Lellouch 1994). The antenna beam was 12.5″ at FWHM while Mars was roughly 15″, so Mars was slightly resolved. Doppler shifts of the CO absorption core were used to directly measure circulation from roughly 45-55 km in the atmosphere. Surprisingly, these measurements indicated strong retrograde zonal winds at nearly all latitudes ($\sim 120\,\mathrm{m\ s^{-1}}$ at the equator). From Fig. 3.22, the 45-55 km range corresponds well to the inferred retrograde zonal jet from the interferometric CO observations. However, the inferred jet is limited to low latitudes.

Assuming that the true mean zonal flow was roughly similar in early January and early February of 1992, there are two explanations that can reconcile the inferred thermal winds with the measured zonal winds. It is possible that the mea-

sured equator-to-pole temperature gradients of Fig. 3.21 are incorrect, perhaps due to neglect of nightside temperatures or faulty continuum scaling near the poles. If the mean meridional temperature structure at that time exhibited steep positive equator-to-pole gradients in each hemisphere above 0.5 mbar, the result would be global retrograde zonal winds at these altitudes. Alternatively, however, it is quite possible that a strong retrograde zonal flow at low northern latitudes could mask the presence of prograde (eastward) zonal winds at mid latitudes. For the IRAM measurements the sub-earth point was at roughly $+10°$ latitude, near the peak of the retrograde zonal flow in Fig. 3.22. Due to the large beam size of the IRAM measurements, only very marginal latitudinal resolution was allowed. If the retrograde zonal flow at low latitudes was very strong and the eastward jets weak, it is probable that the retrograde zonal flow would dominate the measurements, even those at mid-latitudes, effectively masking the eastward jets.

Zonal winds inferred from Mariner 9 IRIS observations of temperature for the same season are qualitatively the same as these new results based on CO temperature retrievals. Leovy (1982) calculated geostrophic winds based on the Mariner 9 results that show several of the features of Fig. 3.22, including eastward zonal jets near 0.3–0.5 bar in both the northern and southern hemispheres, with the southern jet being stronger. However, for the Mariner 9 observations the peak velocity of the southern jet is $120\,\mathrm{m\ s^{-1}}$ while the northern jet is much weaker at $30\,\mathrm{m\ s^{-1}}$. In addition, the jets in both hemispheres are centered further from the equator than those in Fig. 3.22, near $-50°$ and $+60°$.

Zonal winds inferred from the temperature calculations of the Ames Global Circulation Model for the same season are quite comparable to the Mariner 9 observations (Haberle 1993). For $L_S = 44°$ the GCM calculates eastward zonal jets at mid- to high latitudes in each hemisphere, with the southern jet approaching $100\,\mathrm{m\ s^{-1}}$ and

the northern jet being relatively weak ($\sim 30\,\mathrm{m\ s^{-1}}$). In addition, from approximately 1 to 0.1 mbar the northern low latitudes exhibit a retrograde zonal jet of roughly $-30\,\mathrm{m\ s^{-1}}$ maximum velocity.

The differences between the zonal wind field inferred from the 1993 CO temperature retrievals and the Mariner 9 observations and Ames GCM calculations are in part due to the much lower spatial resolution of the CO observations. However, the qualitative results of eastward zonal jets in each hemisphere are fairly robust since they depend on the mean equator-to-pole temperature gradient which is resolved by these measurements. However, the finer details of the wind map are probably in error. In particular, both the magnitude and location of peak zonal velocities are highly uncertain. Because the gradient thermal wind is directly related to the meridional temperature gradient, any smoothing or blurring of that gradient will alter the inferred zonal wind. We conclude that there are equator to pole gradients in each hemisphere evident in the data, and that the probable response of the Martian atmosphere was eastward zonal jets in the middle atmosphere at the time of the observations. Despite the apparent corroboration of the retrograde zonal flow observed at IRAM, at least at low latitudes, the identification of a retrograde zonal jet from the thermal data is considered uncertain.

3.5. Conclusions

Interferometric observations of the ^{12}CO $J(1-0)$ rotational transition were made with the Owens Valley Millimeter Array from February 6-13, 1993, during Martian northern mid-spring ($L_S = 37°$). The interferometric data allowed mapping of the CO emission-absorption feature with a spatial resolution of 4.2″ when Mars was 12.5″ in diameter. The spectra exhibit differences in both local time and latitude which were interpreted in terms of the local temperature structure of the surface and atmosphere.

The spectra were numerically inverted for localized profiles of temperature, using a thermal model of the Martian regolith (Rudy *et al.* 1987) to calibrate the continuum (i.e., surface) brightness temperature. For the inversions CO was assumed to be vertically well-mixed and globally uniform with a mixing ratio of 8×10^{-4}. The thermal structure revealed shows considerably variation with latitude, and some variation with local time. All retrieved temperature profiles are distinctly cooler (by roughly 20 K) than those observed during the Viking era (Seiff 1978). These colder temperatures match extremely well a mean temperature profile determined from whole disk CO observations roughly 20 days earlier (R. T. Clancy, personal communication, 1995). These colder temperatures are indicative of a Martian atmosphere which was nearly dust-free at the time of the observations (e.g., Clancy *et al.* 1990).

Temperature profiles retrieved from high southern latitudes are essentially isothermal from the surface to 40 km. Equatorial temperature profiles are warmest near the surface and compare well with radiative-convective models of thermal structure (Gierasch and Goody 1968, Pollack *et al.* 1979) below 30-40 km. High northern latitude profiles are cooler than equatorial profiles. The mean meridional temperature structure, while somewhat compromised by low latitudinal resolution, shows a remarkable degree of similarity with both observations (temperature retrieved from Mariner 9 IRIS spectra, Leovy 1982) and modeling (Ames General Circulation Model results for relatively clear conditions, Haberle *et al.* 1993).

The gradient thermal wind equation was used to calculate the mean zonal wind field from the retrieved mean meridional temperature structure. Observed negative equator-to-pole temperature gradients below 0.3 mbar lead to eastward (prograde) zonal jets at low to mid-latitudes in both the northern and southern hemisphere. The southern jet is stronger due to a steeper equator-to-pole gradient. While qualitatively

similar to thermal winds based on Mariner 9 IRIS spectra and those calculated by the Ames GCM, which both show a strong eastward zonal jet at southern latitudes and a weaker eastward jet at northern latitudes, the exact location and peak velocity of the jets compare poorly. This is probably due to the relatively low latitudinal resolution of the interferometric observations.

In addition, there is some indication of a westward (retrograde) zonal jet at low northern latitudes above 0.1 mbar. For low latitudes at least, this would appear to corroborate zonal retrograde winds directly observed in early January 1993 (Lellouch *et al.* 1993, Gillet and Lellouch 1994). However, the presence of this jet at such low latitudes could be due to small errors in the retrieved mean meridional temperature structure which were amplified by the Coriolis term in the gradient thermal wind equation. The inference of this retrograde zonal jet is therefore tentative.

This experiment has shown the feasibility of obtaining high-quality disk resolved CO spectra which can be used to address the thermal and dynamical structure of the Martian atmosphere from the surface to roughly 70 km. It marks the first resolved observations of atmospheric temperature since the Viking era, and while the low resolution prohibited a detailed analysis, did provide a measurement of temperature variations in both latitude and local time. Qualitatively, the latitudinal variations compare favorably with observations and models. However, higher resolution observations would be even more beneficial by allowing a finer description of the mean meridional temperature structure.

Continuous improvements in the Owens Valley Millimeter Array and other millimeter-wave facilities promise more accurate and detailed observations of the Martian atmosphere in coming years. In particular, the growth of the Owens Valley Millimeter Array to six antennas allows complete mapping in just one day, compared to the three days used for this experiment. The additional antennas also allow for better

constrained application of phase self-calibration. The opposition of Mars in March 1997 will provide an excellent opportunity to observe the northern hemisphere in greater detail, and to more clearly define the mean meridional temperature structure and zonal wind field.

Chapter 4

Venus: Temporal Variations of the Mesosphere.

The Venus atmosphere is comprised of three regimes: the massive troposphere with its strong retrograde zonal winds (surface to cloud tops), the thermosphere with a remarkable diurnal temperature difference which drives a classic axisymmetric sub-solar to anti-solar flow (above 120 km), and the mesosphere. The mesosphere is the least studied portion of the Venus atmosphere, but is a region of interest because of its role as the transition region between the primarily zonal tropospheric wind field and the sub-solar to anti-solar thermospheric wind field.

Millimeter CO lines offer an effective way to study the mesosphere of Venus. Over the last 15 years single dish observations have suggested that the mesosphere exhibits dramatic changes in structure and dynamics on timescales of a few years. Heterodyne measurements with an interferometer allow characterization of the CO distribution with unequaled spatial resolution, which in turn can be used to infer the circulation of the mesosphere. Expansion of millimeter arrays in recent years now allow for the complete mapping of Venus in a single track, allowing freedom to schedule several runs during an observing season and thus measure changes in the CO distribution on that timescale. This chapter details observations taken a month apart in late 1994 which show that the mesosphere experienced moderate changes in CO distribution over that time, with implications for variability of the mesospheric circulation.

ABSTRACT–Millimeter-wave heterodyne observations of the ^{12}CO $J(1-0)$ rotational transition from the mesosphere of Venus were made in early November and early December 1994 with the Owens Valley Radio Observatory Millimeter Array. The spatial resolution for each day was about 1000 km at the sub-earth point. The high

quality CO spectra were numerically inverted for profiles of the local CO mixing ratio from 80 to 105 km, assuming a Pioneer Venus mean temperature profile for the atmosphere. For each day the revealed CO distribution shows a nightside maximum centered at low latitudes and shifted from the anti-solar point toward the morning terminator. Both days show a clear latitudinal falloff in the CO abundance. In November the maximum was centered at roughly 2^h local time at 100 km, while in December the maximum was at roughly $4-4.5^h$ local time at 100 km. In addition, CO abundances were slightly higher in November. The changes in the CO distribution are examined in the context of the mesospheric circulation model of Clancy and Muhleman (1985b). The increased shift away from the anti-solar point and decreased CO abundance for the December observations both point toward increased zonal and/or decreased sub-solar to anti-solar circulation within the mesosphere during the month between observations.

4.1. Introduction

The atmosphere of Venus is conventionally divided into three regimes. The massive troposphere ranges from the surface to the cloud tops (roughly 70 km) and is the location of the poorly understood superrotating retrograde zonal winds. The thermosphere (above 120 km) is characterized by an extreme diurnal temperature difference (300 K to 120 K) which drives an axisymmetric sub-solar to anti-solar (SS-AS) flow. The mesosphere (70 to 120 km) has long been the least well-known of the three regions, because the extensive group of unmanned missions to Venus and most ground based observations for the most part have been sensitive to the troposphere of thermosphere, leaving the mesosphere relatively unmeasured.

This lack of information is unfortunate. The mesosphere is a transition region, where the global circulation switches from the extreme zonal superrotation of the troposphere to the SS-AS flow of the thermosphere. There are many unanswered

questions concerning the circulation within the mesosphere, including the relative levels of zonal, meridional, and SS-AS winds, how they extend into the mesosphere and are maintained, and the variability of the circulation.

Until recently, dynamical studies of the mesosphere have been done primarily through the use of circulation models, which generally assume cyclostrophic balance and rely on latitudinal temperature gradients measured by Pioneer Venus descent probes, the Pioneer Venus Orbiter Infrared Radiometer, and Pioneer Venus Orbiter radio occultations. Most models found that during the Pioneer Venus era there was a net positive poleward temperature gradient above 70 km, and a corresponding rapid decrease in the retrograde zonal winds above the cloud tops (e.g., Taylor *et al.* 1980). On the other hand, Pioneer Venus descent probe measurements of temperature showed little equator to pole gradient in the mesosphere, allowing zonal winds to remain above 100 m s^{-1} from the cloud tops to roughly 95 km (Seiff *et al.* 1980). In addition, radio occultation measurements show that the equator to pole temperature gradient has reversed on occasion and in principal this allows zonal winds in the mesosphere (see Kliore and Mullen 1988).

Direct detection of circulation within the mesosphere can be accomplished through measurements of Doppler shifts in the spectra of certain molecular species using very high resolution observations. This method dates back almost 20 years (Betz *et al.* 1976). However, only in the last 10 years have instrumental capabilities improved enough to make these measurements reliable. Infrared heterodyne measurements of CO_2 were obtained in 1985, 1986, and 1987 (Goldstein *et al.* 1991). The measurements sensed the 110±10 km region, and were best fit by a SS-AS flow with terminator velocities of 120 m s^{-1} and a superimposed zonal retrograde flow of 25 m s^{-1}. Very different results were found from millimeter interferometric measurements of Doppler shifts in CO rotational lines made in 1988 (Shah *et al.* 1991).

The observations were from the 99±12 km region, and were best fit by a strong 132 m s^{-1} zonal flow. An upper limit of 40 m s^{-1} on SS-AS circulation was also determined. Most recently, single dish observations of Doppler shifts in ^{12}CO $J(2-1)$ and ^{12}CO $J(1-0)$ rotational spectra were made in 1991 with the IRAM 30-m antenna (Lellouch *et al.* 1994) which found yet a third result for mesospheric winds. The group reported that the mesospheric circulation in 1991 was composed of a superposition of retrograde zonal and SS-AS flows of essentially equal strength which increased with altitude (40 m s^{-1} at 95 km and 90 m s^{-1} at 105 km).

These results describe important variability in mesospheric circulation, and suggest changes in the temperature structure of the mesosphere on similar timescales as well. In support of this are whole disk observations of several CO millimeter lines which allow the simultaneous retrieval of both the temperature and CO mixing ratio profiles (Clancy and Muhleman 1991). Spectra obtained near inferior conjunctions in 1982, 1985, 1986, 1988, 1990 were used to determine the average CO profile from 75–105 km and the average temperature profile from 85–100 km on the nightside of Venus. The resulting temperature profiles from 1982 and 1990 were in good agreement with Pioneer Venus observations from 1979, but the 1985, 1986, and to some extent the 1988 observations led to profiles that were 20–40 K warmer, similar to the anomalously warm profile returned by the Venera 10 probe in 1975 (Avdueskiy *et al.* 1983). In addition to temperature variability these observations charted extreme variations of the CO abundance during 1985 and particularly in 1986.

Millimeter observations of carbon monoxide offer unique access to the mesosphere because the formation of these rotational transitions occurs almost completely within the mesosphere. The lineshape characteristics of CO spectra contain information on the vertical distribution of CO, which in turn can provide additional insight to the dynamics of the mesosphere. Several past investigations have addressed the

horizontal and vertical distribution of CO. The first detection of a millimeter transition in a planetary atmosphere (CO $J(1-0)$, Kakar *et al.* 1975) showed that the CO mixing ratio increases with altitude in the Venus mesosphere. Diurnal variability was studied by Schloerb *et al.* (1980) and Wilson *et al.* (1981), who inferred from whole disk spectra taken at different phase angles that CO was more abundant on the nightside than the dayside above 95 km, and vice versa below 95 km.

A comprehensive study of all existing CO spectra of Venus available in 1985 was undertaken by Clancy and Muhleman (1985a,b). By careful analysis of spectra taken from a variety of phase angles they determined that CO exhibited a maximum, or bulge, on the nightside of Venus. The bulge is similar to nightside abundance maxima of H, He, O, and NO detected in the thermosphere (Niemann *et al.* 1980, Brinton *et al.* 1979, Stewart and Barth 1979, Mayr *et al.* 1980, Keating *et al.* 1980, Bougher *et al.* 1990). The thermospheric abundance maxima all show shifts of varying degree toward the morning terminator, which have been interpreted as due to 50–75 m s^{-1} retrograde zonal winds at 150 km (Mayr *et al.* 1980, Schubert *et al.* 1980). General circulation models, based on the original thermospheric models of Dickinson and Ridley (1975, 1977) have been improved to include zonal winds which do produce shifts in nightside abundance maxima (Bougher *et al.* 1988). The millimeter observations showed a similar shift in the mesospheric CO maximum. After testing photochemical-diffusive models, Clancy and Muhleman concluded that this shift was due to a 50 m s^{-1} retrograde zonal flow in the mesosphere up to 90 km.

With the development of millimeter interferometers it has become possible to map the CO lines, allowing measurements of the spatial variability of CO on Venus. Interferometric observations of CO were performed at the Owens Valley Radio Observatory (OVRO) Millimeter Array in 1986 (Muhleman *et al.* 1987, Gurwell *et al.* 1995) and 1988 (Shah *et al.* 1991, Shah 1992, Gurwell *et al.* 1995), and at the

Berkeley-Illinois-Maryland Array (BIMA) in 1987 (de Pater *et al.* 1987, 1991). The BIMA observations provided a qualitative confirmation of the day-night asymmetry above 95 km, but the spectra were of only modest signal-to-noise which did not permit inversion of the line. The OVRO data were of sufficient quality to allow numerical inversion for CO mixing ratio profiles, which showed dramatic variation of the CO abundance (Fig. 4.1). The 1986 results clearly showed a pronounced maximum in CO abundance above 90 km on the nightside of Venus which was shifted to roughly 3.5^{h} local time. In addition, the measurements characterized for the first time the latitudinal variation of the CO mixing ratio. The 1986 data showed a distinct falloff in abundance from equator to pole, while the 1988 observations showed little latitudinal variation.

Carbon monoxide is a photolysis product created on the dayside of Venus. The direct recombination of CO with O to form CO_2 is spin forbidden, and therefore proceeds slowly except in the lower atmosphere. The stability of the atmosphere therefore depends on efficient catalytic reactions involving hydroxyl and chlorine radicals to recycle CO and O back into CO_2 (e.g., Yung and DeMore 1982); these radicals are maintained only on the dayside. Thus, CO production and loss occur almost exclusively on the dayside of the planet. Observations of large nightside CO abundances (Clancy and Muhleman 1985a, 1991, Gurwell *et al.* 1995) indicate that carbon monoxide is transported from the dayside to the nightside. Therefore, the spatial distribution of CO has important implications for mesospheric circulation.

This chapter presents new interferometric observations of the ^{12}CO $J(1-0)$ rotational line from the mesosphere of Venus, obtained with the expanded OVRO Millimeter Array, from November 8 and December 9, 1994. Improvements in the OVRO Millimeter Array in the 6 years since the last interferometric maps of CO were obtained allow further assessment of the temporal and spatial variations of CO

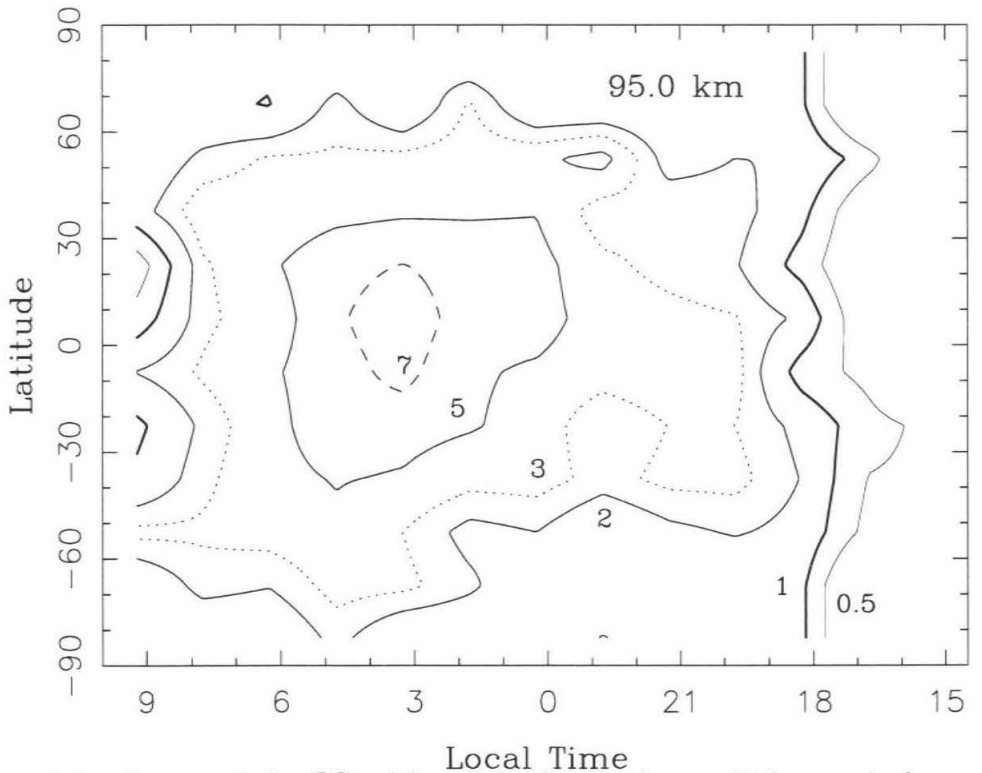

Figure 4.1. A map of the CO mixing ratio distribution at 95 km made from a synthesis of observations taken in 1986 and 1988 with the OVRO Millimeter Array (Gurwell *et al.* 1995). Contours are mixing ratio in units of 10^{-4}.

in the mesosphere and their relationship to mesospheric dynamics. Recent discoveries of hemispheric variability of the CO abundance in the deep atmosphere (Collard *et al.* 1993) added further impetus for obtaining high quality maps of the CO distribution in the mesosphere. The primary goal of these observations was to directly measure mesospheric winds near 100 km; unfortunately, the reduction of the wind data has proven to be extremely difficult and no results are available at this time. The secondary goal of these observations, which was achieved, was to investigate the spatial distribution of CO in the mesosphere in 1994, particularly to measure the location of the CO maximum, and to characterize changes in the distribution with time. While whole disk measurements have been made from conjunction to conjunction, these

TABLE 4.1

Parameters for the November 8, 1994 Observations of Venus

Reference Date		15.3^h 8 November
Right Ascension		$14^h\ 15^m$
Declination		$-18°\ 07'$
Geocentric Distance		0.27369 AU
Apparent Diameter		$60.97''$
Sub-earth	Latitude	$+5.4°$
	Local Time	12:50 AM
Sub-solar	Latitude	$+0.3°$
North Pole Position Angle		$19.6°$
Synthesized beam		$5.5''$
Resolution at sub-earth point		$\sim$1090 km

new observations offer for the first time independent maps of the CO distribution on the timescale of a month. The results show that the mesospheric CO abundance underwent moderate changes from November to December, 1994, reflecting changes in the mesospheric circulation on that timescale.

4.2. Millimeter Observations and Data Reduction

Observations of Venus in the ^{12}CO $J(1-0)$ rotational transition were obtained with the OVRO Millimeter Array on November 8, 1994 and again on December 9, 1994. The OVRO Millimeter Array has been expanded since the Mars observations of 1993, and currently consists of six 10.4-m diameter antennas, moveable to a suite of fixed stations along T-shaped railroad tracks. Each day's observations consisted of a roughly 7.5 hour track of Venus, plus further calibration observations made before Venus rose and after Venus set. Despite the unfavorable declination of Venus ($-18°$ in November and $-12°$ in December) the observations from each day were sufficient to allow mapping of the CO line with unprecedented spatial resolution and signal-to-

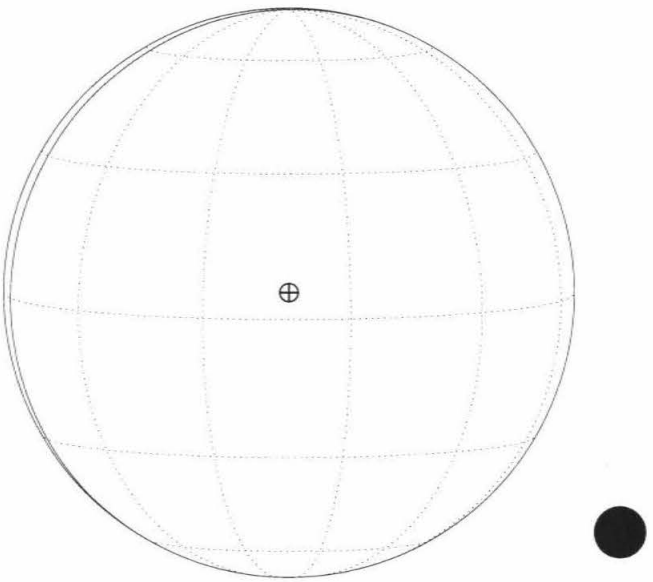

Figure 4.2. The aspect of Venus on November 8, 1994. The ⊕ symbol designates the sub-earth point. The solid line forming a slim crescent on the left marks the morning terminator; nearly all of the observed disk is in Venus night. The circle at lower right shows the size of the synthesized beam FWHM (5.5″) relative to Venus (60.97″).

noise.

Tables 4.1 and 4.2 list some important characteristics of the Venus observations for November 8 and December 9, respectively. Figures 4.2 and 4.3 show the aspect of Venus and the relative size of the synthesized beam for each date. On November 8, Venus had just past inferior conjunction and was very large (nearly 61″ in diameter). At that time the interferometer was in a relatively tight configuration allowing a synthesized beam of 5.5″ at FWHM, or roughly 1090 km at the sub-earth point. These observations were essentially limited to the nightside hemisphere (see Fig. 4.2). On December 9 Venus was approaching greatest western elongation, allowing a good

TABLE 4.2

Parameters for the December 9, 1994 Observations of Venus

Reference Date		14^h 9 December
Right Ascension		14^h 22.5^m
Declination		$-11°$ $45'$
Geocentric Distance		0.41700 AU
Apparent Diameter		$40.02''$
Sub-earth	Latitude	$-1.0°$
	Local Time	4:10 AM
Sub-solar	Latitude	$-1.8°$
North Pole Position Angle		$19.0°$
Synthesized beam		$3.1''$
Resolution at sub-earth point		~940 km

view of the morning terminator, and was $40''$ in diameter. The interferometer at this time was in an extended configuration, providing a synthesized beam of $3.1''$ at FWHM, or roughly 940 km at the sub-earth point. During each days track the size of Venus changed slightly, and it was therefore necessary to normalize the (u, v) spacings and observed visibility amplitudes to the reference times shown in Tables 4.1 and 4.2.

Superconductor-insulator-superconductor (SIS) receivers sensitive in the 80–116 GHz range were used to receive the microwave signal from Venus, detected for each antenna pair in two sidebands. The signals from each sideband were isolated through phase switching of the local oscillator (LO) reference signal. For observation of CO on Venus the upper sideband was centered on the ^{12}CO $J(1-0)$ transition frequency of 115.271204 GHz and receiver gains were optimized to favor this sideband as much as possible to improve signal-to-noise. The transition frequency reference was maintained in the Venus frame by computer control of the LO. The signal in the upper sideband was detected in two correlator systems: a wideband analog cross-

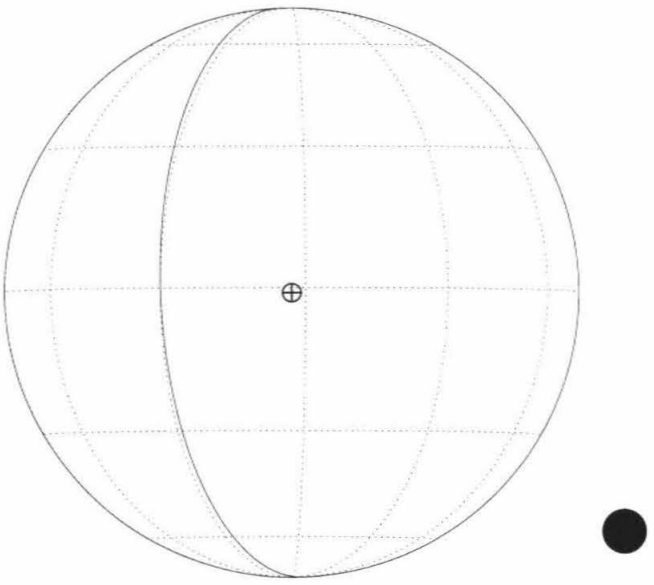

Figure 4.3. The aspect of Venus on December 9, 1994. The $\oplus$ symbol designates the sub-earth point. The solid line forming a crescent on the left marks the morning terminator; most of the observed disk is in Venus night. The circle at lower right shows the size of the synthesized beam FWHM (3.1″) relative to Venus (40.02″).

correlator ($\sim$1 GHz bandwidth) and a digital cross-correlator spectrometer. The digital spectrometer was configured to simultaneously measure the CO line at two spectral resolutions: 1 MHz (total effective bandwidth 120 MHz) and 62.5 kHz (total effective bandwidth 7.5 MHz). Each of the two bands were centered on the Venus CO transition frequency. Padin *et al.* (1991) provides further details on the OVRO interferometer and its capabilities.

The CO lineshape on Venus is usually confined within $\pm$50 MHz of the line center (e.g., Clancy and Muhleman 1991, Lellouch *et al.* 1994). Thus the 1 MHz resolution data allowed a measure of the Venus thermal continuum in the outer edges of

the passband while measuring the full line shape. The inner line core was measured at high resolution with the 62.5 kHz observations, providing CO weighting functions in the upper mesosphere. Instrumental and atmospheric variations affecting the observations of Venus were measured by observing standard sources as calibrators. Basic parameters such as antenna positions and delays on signal lines were determined by the OVRO staff before the observing runs in each month. These spectral line observations required careful calibration of the digital spectrometer passband, accomplished through observations of a very high signal-to-noise, internal noise source to measure channel to channel variations, followed by lengthy observations of 3C273 to correct for low order trends in the noise source spectrum. During each track, phase and amplitude gain variations were monitored with periodic observations of the quasi-stellar sources 1334-127 (both dates) and 1510-089 (December only). Due to the very large size of Venus relative to the typical OVRO antenna primary beam ($\sim 60''$), accurate pointing of the array elements was crucial; the pointing of the individual antennas was checked and updated roughly every hour from observations of 3C279.

Initial calibration was performed using MMA, the OVRO software package for reducing Millimeter Array data. This calibration included correction of phase and amplitude drifts with time, calibration of the spectrometer passbands, and setting the initial flux scale. The initial flux scale was set using observations of Uranus (a primary calibrator) to estimate the flux of 1334-127, placing the visibility measurements from all baselines on a common flux scale. The absolute flux scale for the (u, v) data was determined from a comparison of the observed continuum visibilities to a model of the Venus visibility function at 2.6 mm for the size and array configuration appropriate for each day of observation (including primary beam weighting).

The Venus (u, v) data were self-calibrated and mapped using the NRAO Astronomical Image Processing System (AIPS) software package. Phase self-calibration

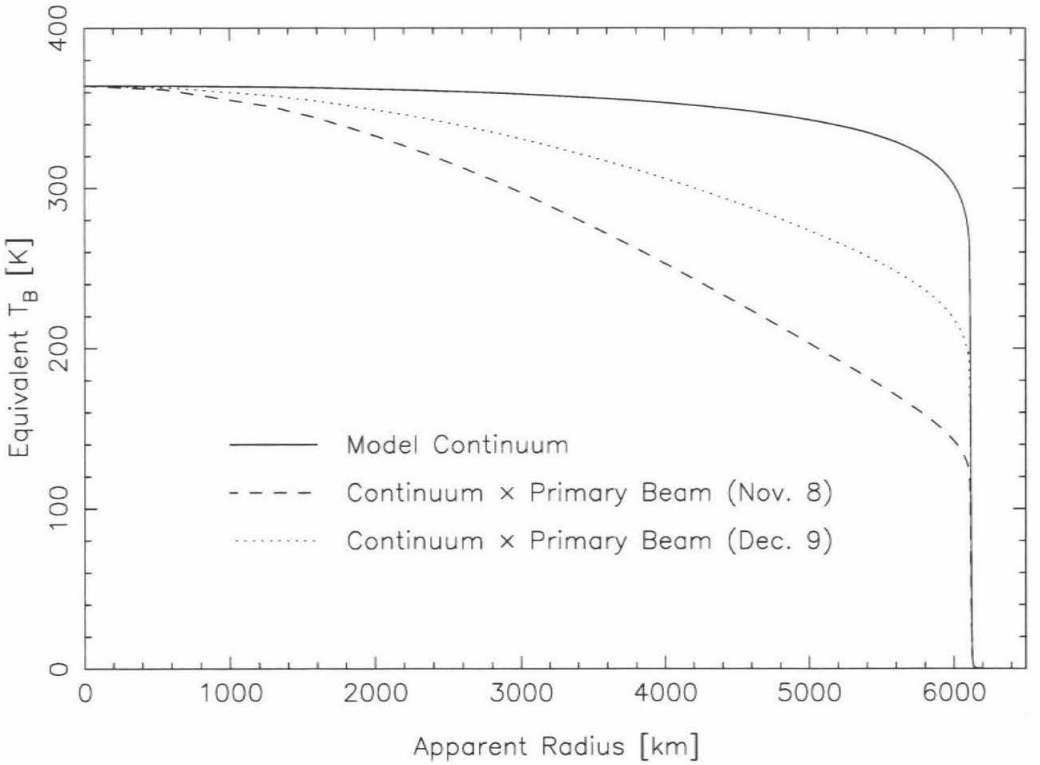

Figure 4.4. The radiative transfer model continuum intensity (units of Planck brightness temperature) as a function of apparent radius from the disk center, along with curves for the model continuum multiplied by a model primary beam weighting appropriate for the observations dates. The OVRO primary beam FWHM is 58±3″; in November Venus was 61″ in diameter and in December Venus was 40″ in diameter.

attempts to correct phase errors introduced by variations in the phase delay of the atmosphere, an antenna based phenomenon (see Chapter 1 for a discussion of phase self-calibration and its application). Self-calibration requires a strong source and a model of the source structure. For Venus both these requirements were easily satisfied. The basic model of the Venus disk was based on a radiative transfer model of the Venus atmosphere at 2.6 mm providing the continuum intensity (see Section 3.3). In addition, the primary beam weighting of the disk was included as it seriously affects the inferred brightness distribution (Fig. 4.4).

The real part of the phase self-calibrated continuum visibilities are presented

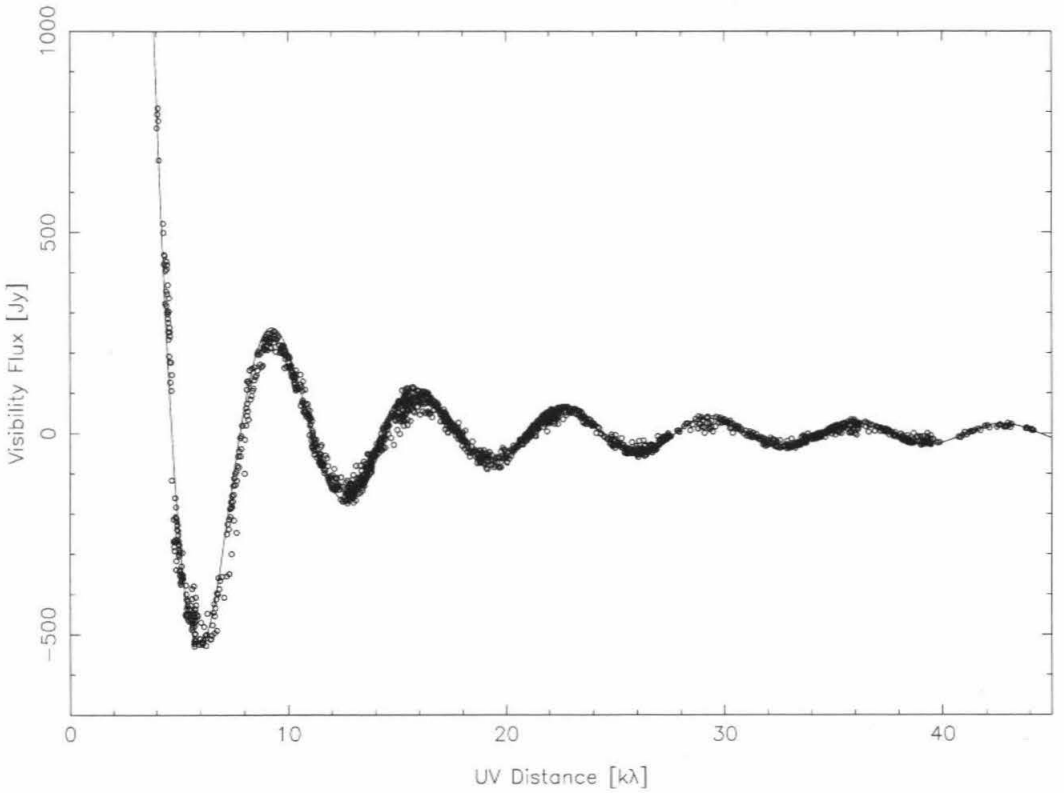

Figure 4.5. The real part of the continuum visibilities for November 8, 1994.

in Figs. 4.5 (November 8) and 4.6 (December 9). Model visibility functions are also plotted as solid lines. Note that these measurements are for all observed positiona angles of Venus. For the November 8 conditions the model whole disk (i.e., zero-spacing) flux including primary beam effects is 6870 Jy, and for the December 9 conditions the model whole disk flux is 3600 Jy, reflecting the smaller size of Venus at that time. Note that the visibility data compare remarkably well to the model visibility functions.

Maps of the sky brightness distribution are created through a process of numerical Fourier transformation of the visibility data into image space and subsequent deconvolution of the synthesized ("dirty") beam. The brightness in the maps are

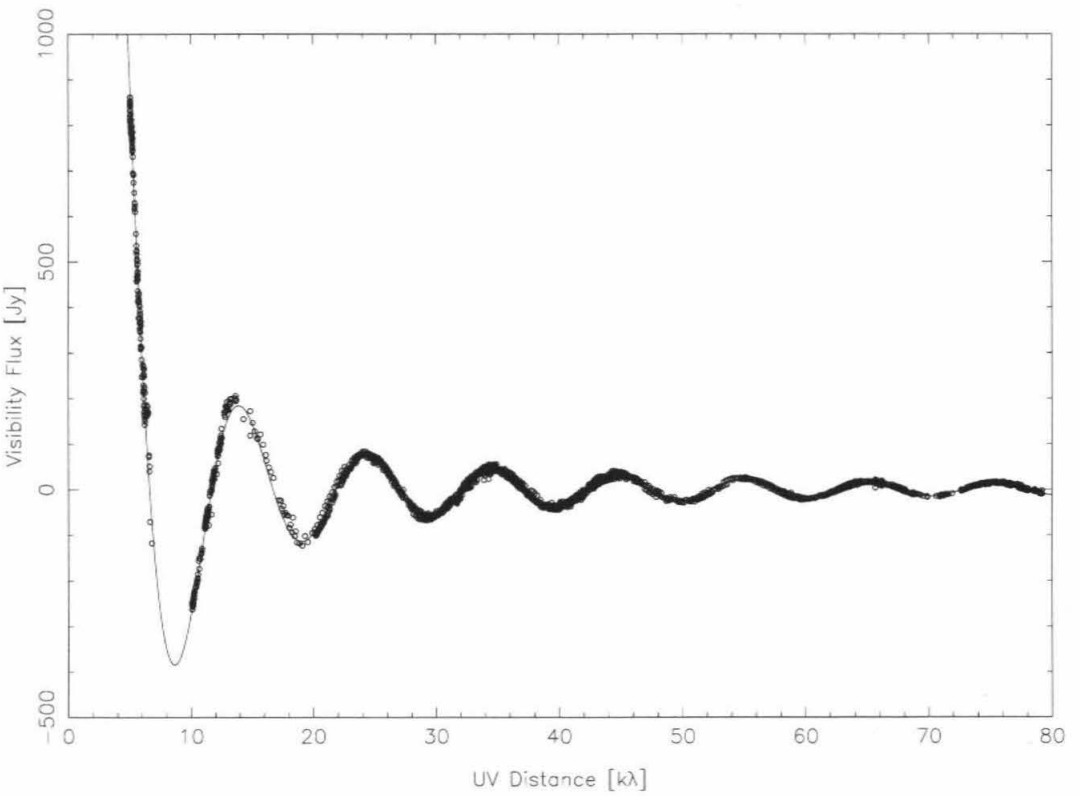

Figure 4.6. The real part of the continuum visibilities for December 8, 1994.

given in units of Jy/beam; the map value at point (x, y) is essentially the flux that would be measured with a single antenna with a beam FWHM equal to the clean beam FWHM centered at that point. A more detailed description of the mapping and deconvolution process is given in Chapter 1.

Maps of the 2.6 mm Venus continuum were produced from the phase self-calibrated visibility data shown above, and are presented in Figs. 4.7 and 4.8 for the November and December observations, respectively. Contours are spaced in 5% intervals of the peak flux in each map. The synthesized beam for the November 8 observations was 5.5″, while for the December 9 observations the synthesized beam was 3.1″. These maps have not been corrected for primary beam effects. The overall

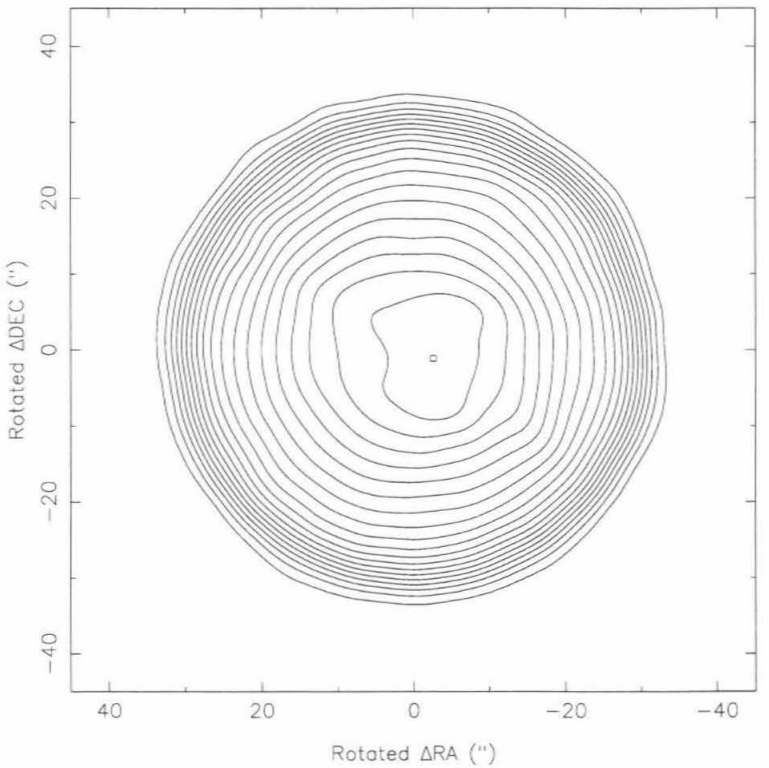

Figure 4.7. The continuum map derived from the visibilities measured on November 8, 1994. Contours are spaced every 5% of the map peak, or roughly 18 K.

differences between the maps are mostly due to the different size of Venus relative to the primary beam size for the two observing dates. Thus the December 9 disk appears to have a sharper edge than the November 8 disk.

The overall appearance of the maps are remarkable in that they deviate very little from the radiative transfer model (weighted by the primary beam) of the 2.6 mm continuum thermal emission. Small differences do exist but the general shape of each is that of a primary beam weighted disk, with minor deviations most probably due to observation and mapping errors. The beam average brightness temperature at the disk center in each map is ~360 K, so 5% contours correspond to 18 K steps in temperature. Maps of the difference between the derived maps and the model

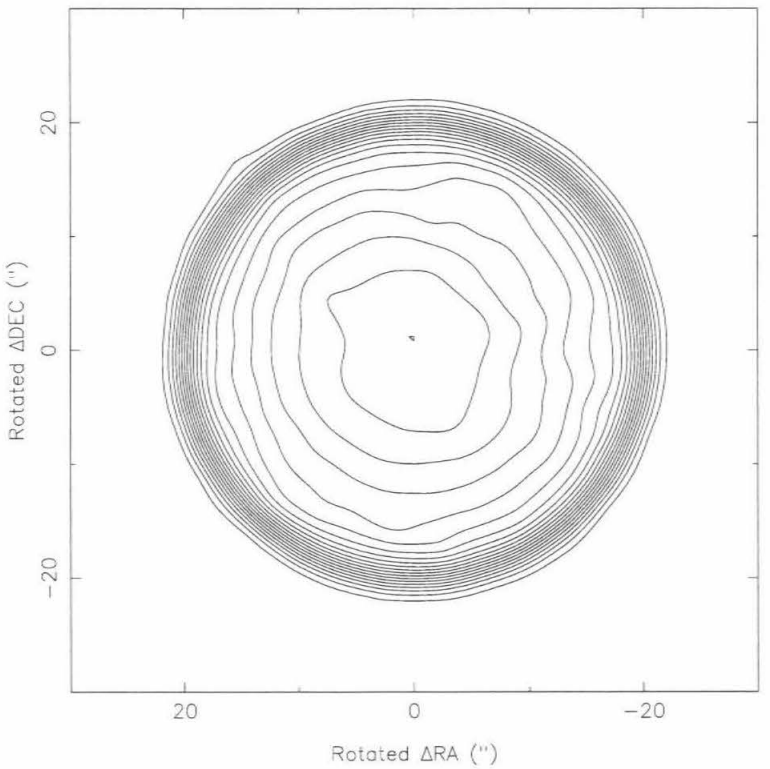

Figure 4.8. The continuum map derived from the visibilities measured on December 9, 1994. Contours are spaced every 5% of the map peak, or roughly 18 K.

maps show that deviations for each date are significantly less than 10 K for most of the observed disk. Maximum deviations are 18 K and 15 K for the November and December maps, respectively. These maximum differences occur near the disk edge, where the brightness falls off quickly with apparent radius and small errors can lead to larger brightness differences.

These continuum results stand in sharp contrast to interferometric observations of Venus from 1987 reported by de Pater *et al.* (1991). They found a 10% increase in the brightness temperature from day to night at 2.7 mm from observations made over two weeks with the BIMA interferometer (a three element array at that time). They speculated that the brightness temperature differences were due to

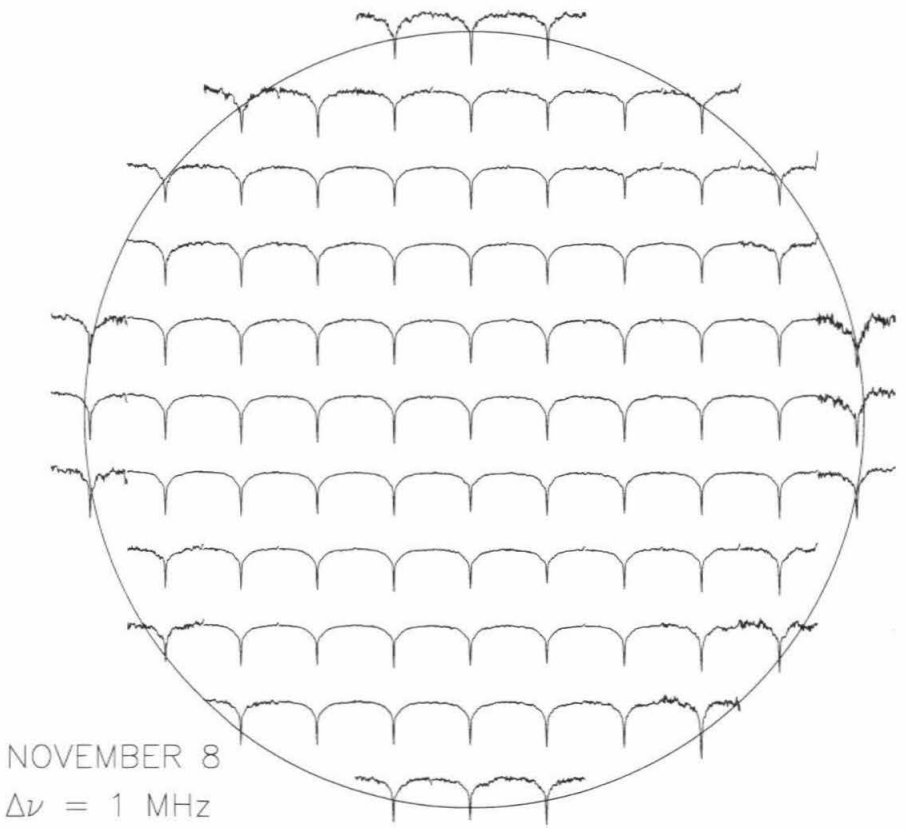

Figure 4.9. Line to continuum spectra at 1 MHz resolution for November 8, 1994. Spectra are plotted every 6″ on the 61″ disk.

an additional unknown diurnally varying opacity source which raises the level of unit optical depth to a higher (cooler) altitude on the dayside relative to the nightside. However, it is unclear from their work if the brightness variation is real or an artifact of phase errors in the visibility measurements. Since the major opacity source (see Section 3.3) at 2.7 mm is carbon dioxide, which should have essentially no diurnal variability in the deep atmosphere, it difficult to posit another opacity source which could realistically cause such a large brightness temperature variation in the contin-

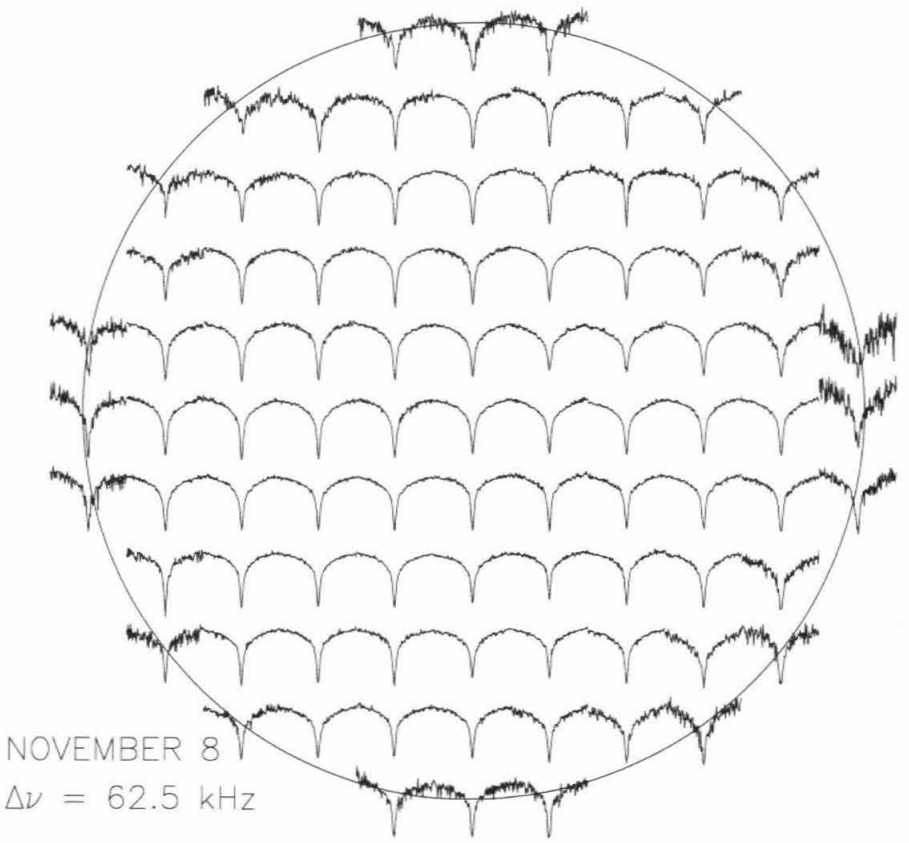

Figure 4.10. Line to continuum spectra at 62.5 kHz resolution for November 8, 1994. Spectra are plotted every 6″ on the 61″ disk.

uum. Additionally, any opacity source at these altitudes would be transported in the superrotation of the atmosphere with a 4-6 day period. That the continuum maps presented here show little variability is further evidence that the millimeter continuum on Venus is highly uniform and that the variations seen by de Pater *et al.* (1991) are more likely due to measurement errors in phase.

The phase corrections found from self-calibration of the continuum channel were applied to the spectral visibility data for each day of observation. The self-

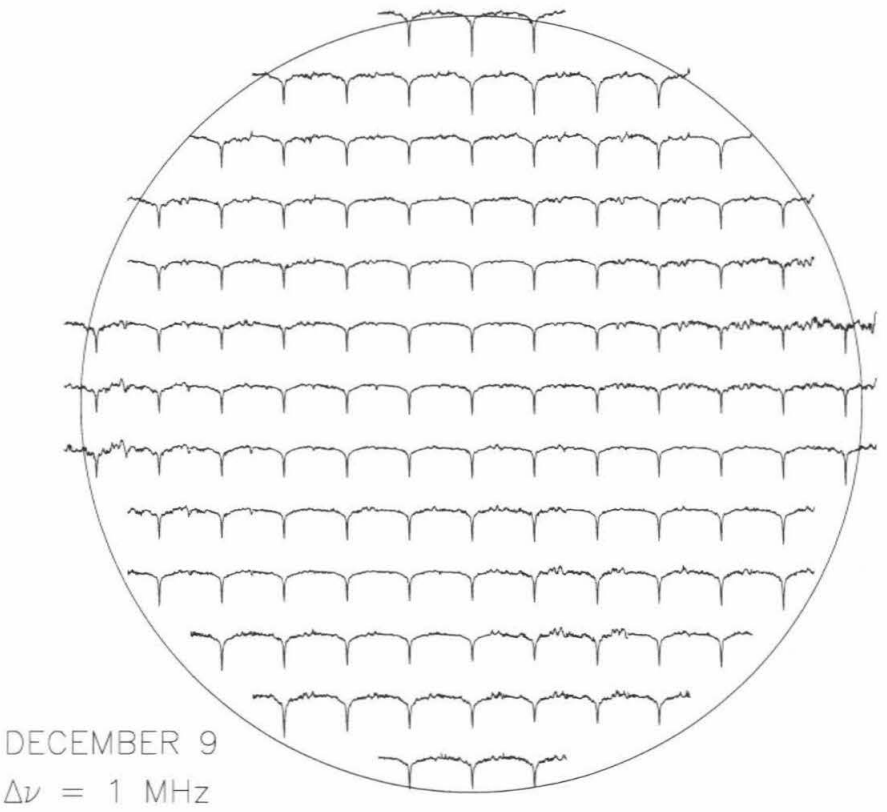

Figure 4.11. Line to continuum spectra at 1 MHz resolution for December 9, 1994. Spectra are plotted every 3.2″ on the 40″ disk.

calibrated data for each channel were then independently mapped and the effects of the dirty beam deconvolved in a manner similar to that used to map the continuum channel. The resulting data set is composed of two spectral image cubes, one for the 1 MHz resolution data and one for the 62.5 kHz data.

Representative line to continuum spectra for each day of observation are provided in Figs. 4.9–4.12. Figures 4.9 and 4.10 correspond to the observations of November 8, 1994, and spectra are plotted every 6″; the disk of Venus was 61″ in diameter

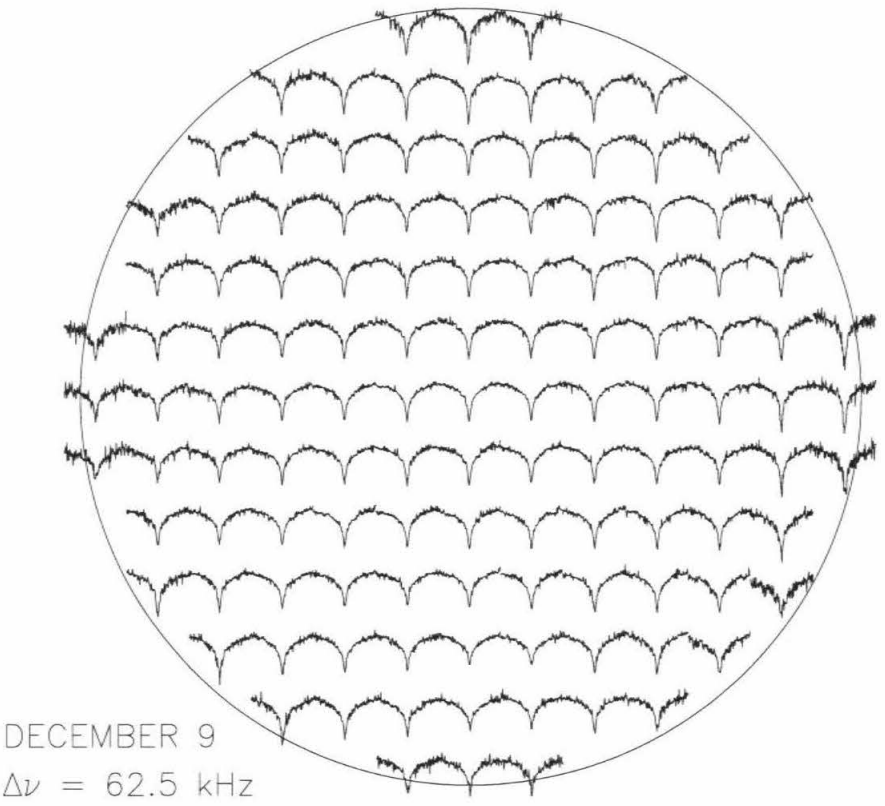

Figure 4.12. Line to continuum spectra at 62.5 kHz resolution for December 9, 1994. Spectra are plotted every 3.2″ on the 40″ disk.

and the synthesized beam was 5.5″ at FWHM for this date. Figures 4.11 and 4.12 correspond to the observations of December 9, 1994, and spectra are plotted every 3.2″; the disk of Venus at that time had a diameter of 40″ and the synthesized beam FWHM was 3.2″.

The spectra are fairly uniform, showing only marginal variation with position on the disk. Line depths are deepest along the limbs for both days, which is probably due to the longer path lengths associated with slanting ray paths in the atmosphere at

the limbs. An exception to this is the relatively shallow linedepths of morning (left) limb spectra seen in the 62.5 kHz spectra for December 9 (Fig. 4.12) when compared with the nightside (right) limb spectra. This last feature suggests that in the upper mesosphere (to which the CO line core is most sensitive) there was less CO on the dayside relative to the nightside on December 9.

4.3. Radiative Transfer Modeling

Radiative transfer near the ^{12}CO $J(1-0)$ transition in the atmosphere of Venus has been detailed in Gurwell *et al.* (1995), and Appendix A presents a discussion of the general radiative transfer method. Highlights of the radiative transfer model are presented below.

The basic parameters of the lower atmosphere are based on the radiative transfer model of Muhleman *et al.* (1979); the base of the atmosphere was adjusted to a mean Venus radius of 6051.5 km, with a surface pressure and temperature of 93.8 bar and 735 K, respectively. The radiative transfer model was comprised of a spherical atmosphere extending from 30 to 150 km above the surface, with layers of 1-5 km thickness. Basic temperature profiles above 85 km for the day and night atmospheres were smoothed versions of profiles found by Pioneer Venus descent probes, which introduced a temperature divergence above ~100 km (Seiff and Kirk 1982). These temperature profiles are plotted in Fig. 4.13.

Opacity due to carbon monoxide was modeled using the spectroscopic parameters of Pickett, Poynter and Cohen (1992). The CO – CO_2 collisional broadening coefficient for the CO $J(1-0)$ line was taken to be 3.3 GHz bar^{-1} at 300 K, with a temperature dependence of $T^{-0.75}$ (Varanasi 1975). The CO opacity for each model frequency and atmospheric layer was found by integrating the CO absorption coefficient times the Voigt lineshape (convolution of Doppler and collisional broadening) over the layer, as discussed in Clancy *et al.* (1983); a review is given in Appendix C.

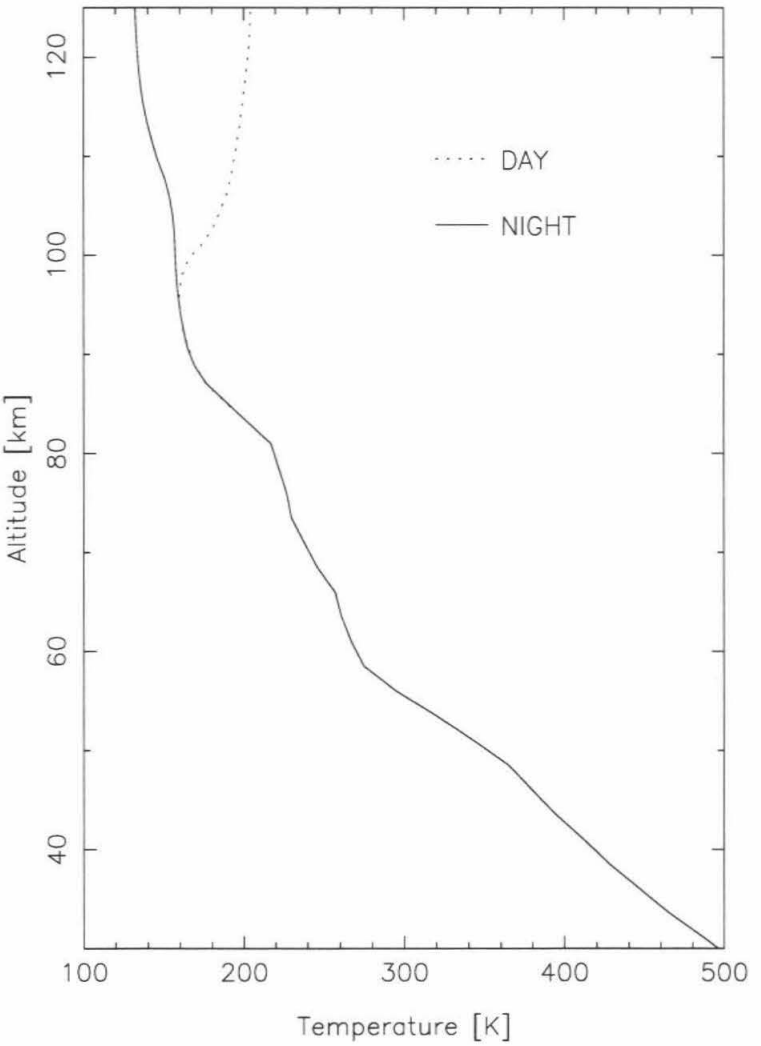

Figure 4.13. Day and night temperature profiles based on the radiative transfer model of Muhleman *et al.* 1979 (below 85 km) and on Pioneer Venus descent probe measurements (above 85 km). The profiles above 85 km have been smoothed to remove transient wave structure.

At millimeter wavelengths the lower atmosphere of Venus is completely opaque due to collisionally induced dipole absorption by CO_2 and pressure broadened rotational line absorption by SO_2. These form a continuum opacity with essentially no frequency dependence across the narrow spectral region of the CO line. These continuum opacity sources prevent the escape of millimeter radiation from below about

40 km in the atmosphere. The CO_2 absorption coefficient was calculated using the expression presented by Ho *et al.* (1966), based on high temperature and pressure laboratory measurements. The absorption due to SO_2 was calculated from the relation presented by Janssen and Poynter (1981), who modeled the entire rotational spectrum of sulfur dioxide in the Venus atmosphere. SO_2 was modeled as having a constant mixing ratio below 40 km (the nominal model used 185 ppm based on Pioneer Venus measurements; see Oyama *et al.* 1980), and falling off rapidly above that with a scale height of $\sim$2 km (Zasova *et al.* 1993).

The algorithm modeled the integrated flux at each frequency step measured by a gaussian beam of specified size and position on the disk of Venus (see Appendix D). This was accomplished by integrating the intensity along many raypaths ($\approx$ 100), including limb geometries. The actual number of raypaths depended on the size of the beam relative to Venus and its location. The primary beam weighting was then accounted for by multiplying these intensities by the primary beam function. The results were interpolated and integrated to give the spectrum in units of flux density per synthesized beam.

Figure 4.14 provides model area-normalized nadir weighting functions for several frequencies near the CO line center. The weighting functions were determined using a standard CO mixing ratio profile and the Venus nightside temperature profile from Fig. 4.14. The weighting functions each separate into two distinct peaks due to the absorption characteristics of the atmosphere. The lower altitude peaks (below 70 km) reflect the continuum absorption and emission by CO_2 and SO_2, while the higher altitude peaks are due to the resonant absorption of CO. Note that the relative size of the peaks is a strong function of frequency. As frequency offset is increased from the line center to the line wings, the contribution of cool mesospheric emission due to CO is lessened and the observed brightness becomes more and more dominated by

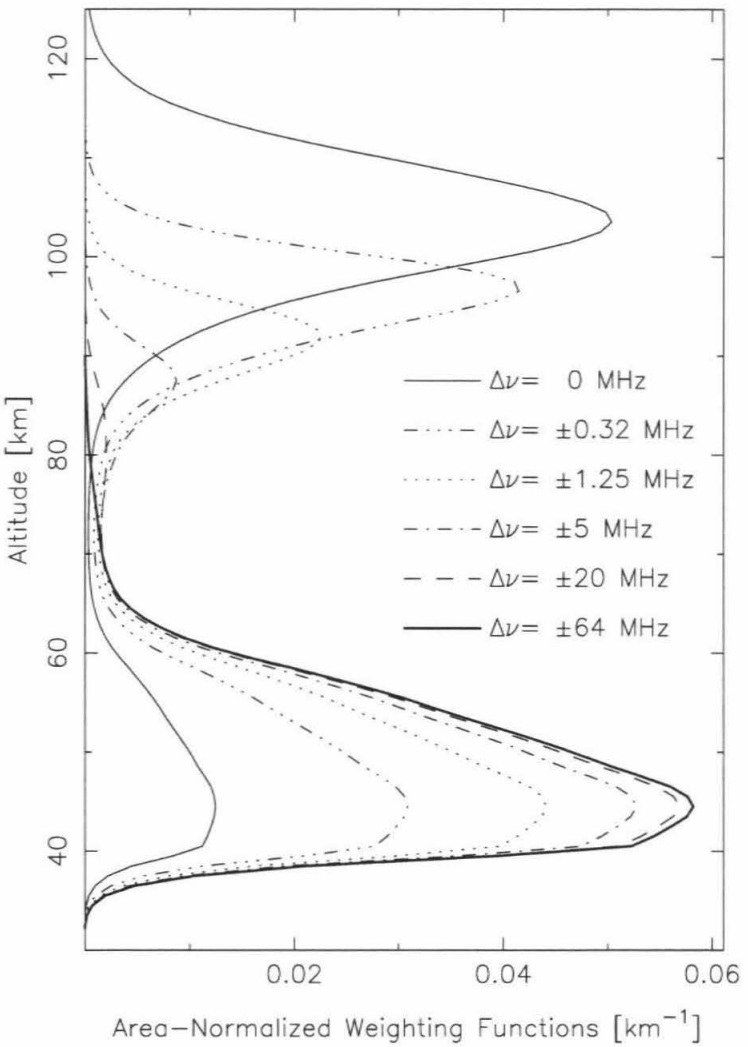

Figure 4.14. Weighting function profiles for the CO $J(1-0)$ line on Venus. Profiles are given as a function of frequency offset $\Delta\nu$ from the line center. The two distinct peaks are due to CO absorption (above 70 km) and the continuum opacity sources (below 70 km).

continuum emission from the warmer lower atmosphere.

As with the weighting functions on Mars, the peak of the weighting function due to CO changes with frequency. The peak altitudes range from about 80 km ($\Delta\nu = \pm 20$ MHz) to 104 km (line center) for a nadir raypath. The ^{12}CO $J(1-0)$ rotational transition can therefore be used to probe the vertical structure of the Venus

atmosphere from roughly 80 to 105 km. However, unlike Mars, the CO line on Venus is optically thin except in the very line center where the opacity is roughly unity. Optically thin lines are most sensitive to absorber abundance, with the temperature profile a less important factor (e.g., Clancy and Muhleman 1991, Lellouch *et al.* 1994). Therefore, the CO $J(1-0)$ line is useful for measuring the mixing ratio profile of CO in the mesosphere over this altitude range.

From Fig. 4.14, the contribution of the mesosphere to the brightness drops to an extremely small fraction just 20 MHz away from the line center. In the line wings the CO opacity is very small, and the sensitivity of the spectrum to CO changes becomes small as well. For this reason it is difficult to accurately determine the CO abundance below 80 km because it requires an extremely precise measurement of the lineshape relative to the continuum. Between 80 and 90 km the sensitivity of the lineshape to CO abundance increases, and is best between 90 and 100 km.

4.4. Spectral Line Inversion

The CO lines obtained from the interferometric observations were analyzed using a least-squares line inversion algorithm to quantify local CO mixing ratio profiles that best fit the observed spectra. Details of the least-squares inversion technique and its application to CO spectroscopy on Venus are given in Gurwell *et al.* (1995) and an overview is presented in Appendix F. In summary, to determine the best-fit CO profile for a given spectrum, a model spectrum is first calculated using a standard CO profile and assuming a local temperature profile. In addition, the analytic partial derivatives of the spectral flux with respect to changes in the CO mixing ratio profile (Appendix B) for each frequency channel are also calculated. The differences between the observed and calculated spectra are used along with the partial derivatives to estimate changes in the CO profile that will better fit the observations. Since the radiative transfer equation is nonlinear with respect to opacity it is necessary to

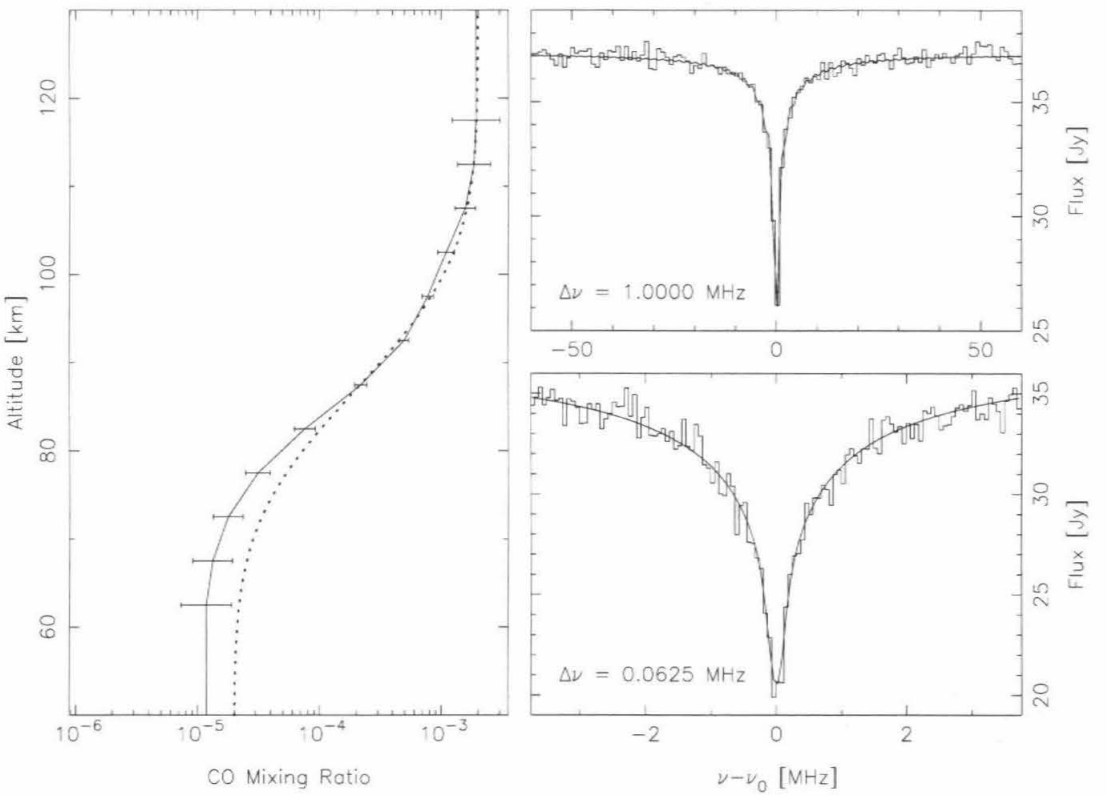

Figure 4.15. Solution CO mixing ratio profile (solid line with error bars) and best-fit spectra for that profile. Dotted line is the input profile used to create the noisy spectra.

iterate until a stable solution is reached.

An example of a numerical line inversion is given in Fig. 4.15. Model spectra at 1 MHz and 62.5 kHz with added noise typical of the observed spectra are shown along with the true input CO profile and the best fit solution profile. The solution profile was determined in 5 km steps from 60 to 120 km; the true vertical resolution is about 5 km as well. Error bars represent the formal error on the solution at each altitude determined from the covariance matrix of the final iteration.

The solution profile is very close to the input profile for all altitudes above 85 km. Below 85 km the solution diverges somewhat from the input profile, as expected due to the difficulty in accurately measuring the line wing relative to continuum in

the presence of noise. The formal errors are smallest in the altitude range of 85 to 100 km, and above 105 and below 80 km start to increase rapidly, showing that the maximum sensitivity of these measurements is in the 85 to 100 km region of the mesosphere.

In order to invert the observed lines for CO abundance profiles, the atmospheric temperature profile must be provided. There is no way to independently retrieve the temperature and CO profiles from the interferometric observations, because they contain measurements of just one transition. This is somewhat problematic, since long term observations of the Venus mesosphere have shown that on occasion the temperature profile at low to mid-latitudes can be 20–40 K warmer than that measured during the Pioneer Venus probe descents (Clancy and Muhleman 1991). In addition, there are possibly equator to pole gradients in the temperature structure of the mesosphere as well.

R. T. Clancy has made single dish observations of several transitions of CO in the Venus mesosphere in November and December, 1994, from which simultaneous disk average CO and temperature profiles can be constructed. These measurements are qualitatively similar to those made on several earlier observing runs and discussed in depth in Clancy and Muhleman (1991). Based on inspection of these measurements and comparison with observations obtained in other years, he has concluded that the low to mid-latitude average temperature profiles for these dates were consistent with the Pioneer Venus descent probe measurements (personal communication, 1995). The estimated error for these types of measurements is 10–15 K in the 85 to 105 km range (Clancy and Muhleman 1991). Hence it is reasonably certain that the average characteristics of the Venus mesosphere in late 1994, at least at low to mid-latitudes, was similar to that found by the Pioneer Venus descent probes.

Equator to pole temperature gradients are usually not much more than 15 K,

but have occasionally been greater (Seiff 1983). In addition, the gradient has from time to time switched sign (Kliore and Mullen 1988). There is no way to determine equator to pole gradients from these interferometric measurements or from the whole disk measurements of Clancy. For this reason, we have made the assumption for purposes of inversion of the spectral line data that no such gradients existed in November or December, 1994. However, since moderate gradients most probably did exist (i.e., supporting possible zonal winds through cyclostrophic balance, etc.) and the temperature measurements of Clancy have significant uncertainties, it is important to estimate errors associated with these assumptions about the temperature structure of the atmosphere.

An indication of the sensitivity of the spectral line inversion to temperature is shown in Fig. 4.16. A 1 MHz and 62.5 kHz pair of spectra from the disk center of the December 9 data were inverted assuming different temperature profiles in the Venus mesosphere. The solution profiles correspond to the Pioneer Venus night profile from Fig. 4.13 (solid line), a profile 15 K warmer than the PV night profile above 80 km (dashed line), and a profile 15 K cooler above 80 km (dotted line). The solutions all retain the same general structure. Maximum differences of ~30% occur above 105 km, and are on average less than 15% below 100 km. The region near 95 km seems to be particularly insensitive to temperature variations of this size. Note that the range of deviation due to temperature shown here is generally larger than the formal solution error estimates for altitudes above approximately 80 km. This means that the true errors of the inversion solutions are dominated by the uncertainties in the local temperature profile for each pixel location on the disk.

These results show that the inversions are relatively insensitive to variations of up to 15 K in the temperature structure of the mesosphere. Due to uncertainties in the actual local temperature profile as well as inversion uncertainties, the best

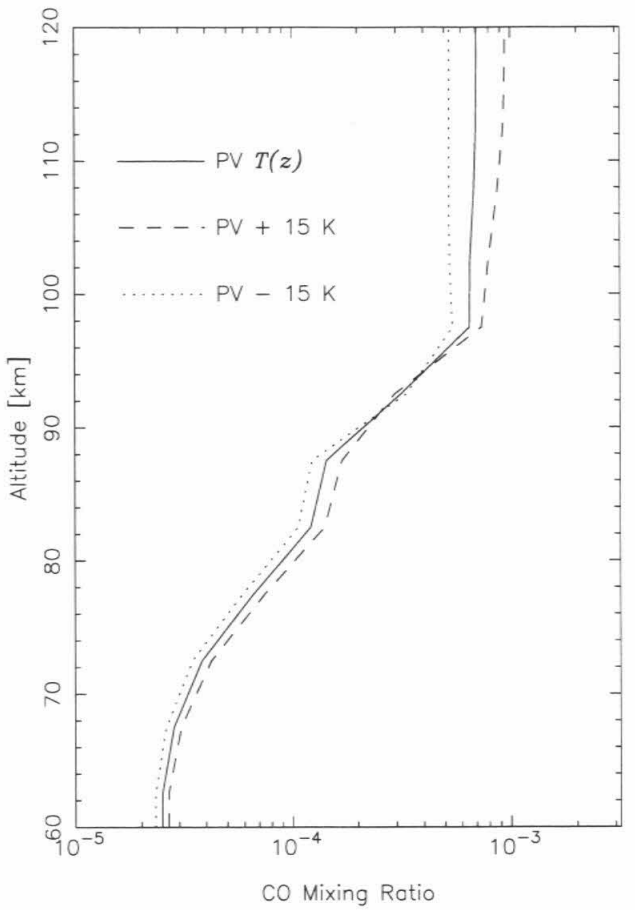

Figure 4.16. Solution CO mixing ratio profiles for an observed 1 MHz and 62.5 kHz pair of spectra from the December 9, 1994 data set. The solid line represents the solution obtained when using a night profile (Fig. 4.13) based on Pioneer Venus descent probe data (Seiff and Kirk 1982). The other solutions were obtained assuming profiles 15 K warmer (dashed line) and 15 K cooler (dotted line).

estimate for the accuracy of the inversion solutions discussed below is about 15-25% from 80 to 105 km. Above and below this range the CO solution profile is less well-constrained. This relative insensitivity to moderate variations in the temperature profile reflects the fact that the ^{12}CO $J(1-0)$ transition is optically thin (except in the line core). As mentioned above optically thin lines generally exhibit lessened sensitivity to temperature and increased sensitivity to abundance.

The observed 1 MHz and 62.5 kHz spectra in each map pixel for each date of

observation were inverted using the line inversion algorithm. For November essentially all pixels corresponded to locations on the nightside of Venus. In December a majority of pixels were on the nightside, but a significant fraction resided on the dayside of the morning limb. For the numerical line inversions the local temperature profile assumed was either the day or night profiles of Fig. 4.13, depending on the pixel location. Since the divergence of these profiles is limited to above $\sim$ 100 km, solutions for the CO mixing ratio at altitude less than 100 km are unaffected by this choice of temperature profile. Solutions do appreciably differ above 105 km due to this divergence. The effects of the assumed diurnal temperature variation on the retrieved CO profiles is therefore minimal in the range of maximum sensitivity (the 85 to 100 km region).

The numerical inversion of the observed spectral image cube led to another cube, this one of the distribution of CO in the mesosphere of Venus both horizontally and vertically. Although the horizontal dimensions of this cube are in sky coordinates (e.g., RA and DEC), the position of each pixel on the disk can be mapped to the appropriate local time and latitude for that location. The next two subsections present maps of the derived CO mixing ratio as a function of local time and latitude at altitudes of 90, 95, and 100 km. The altitudes were chosen because they are within the 85 to 100 km range and are spaced at the approximate vertical resolution of the observations. Therefore, these maps contain the most reliable information on the vertical and horizontal variation of the CO mixing ratio within the mesosphere. The maps represent solutions for well over 1000 pairs of spectra for each date.

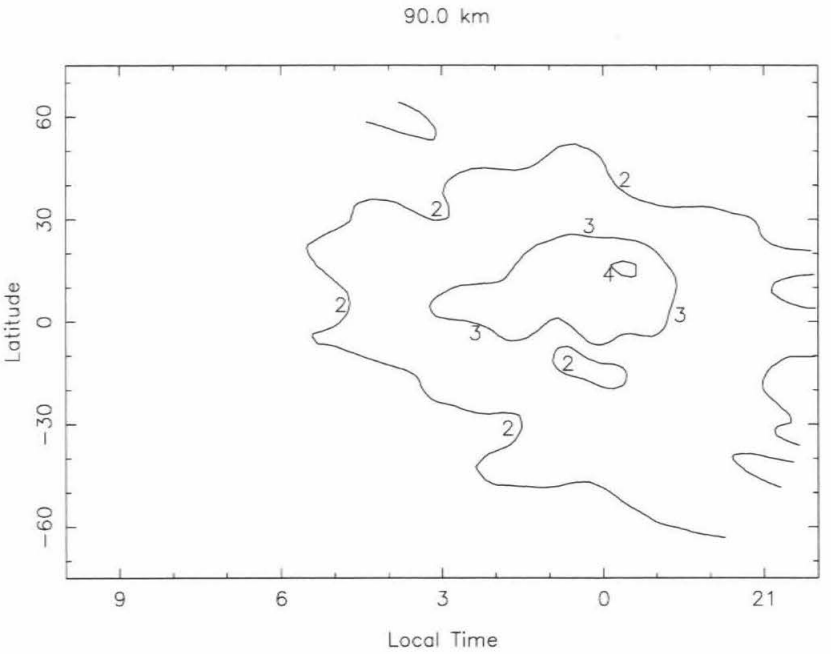

Figure 4.17. Map of the CO mixing ratio at 90 km altitude for November 8, 1994. Contour labels give the mixing ratio in 100 ppm.

4.4.1 Maps of the CO Mixing Ratio: November 8, 1994

Maps of the CO mixing ratio derived from the interferometric observations made on November 8, 1994, at altitudes of 90, 95, and 100 km are presented in Figs. 4.17, 4.18, and 4.19, respectively. These maps represent 1305 different solution profiles. Solutions were obtained every 1.5″, significantly finer than the synthesized beam size of 5.5″, in order to more fully fill the map in local time-latitude space. Map contours are in units of 100 ppm, and grey scale shows structure above 500 ppm (mixing ratio of 5×10^{-4}). CO exhibits a local maximum on the nightside of Venus at all three altitudes, with the peak CO mixing ratio increasing with altitude. The position of the maximum varies from near 0^h local time at 90 km to near 2^h at 100 km. The latitude of the maximum appears to be consistently near $+10°$.

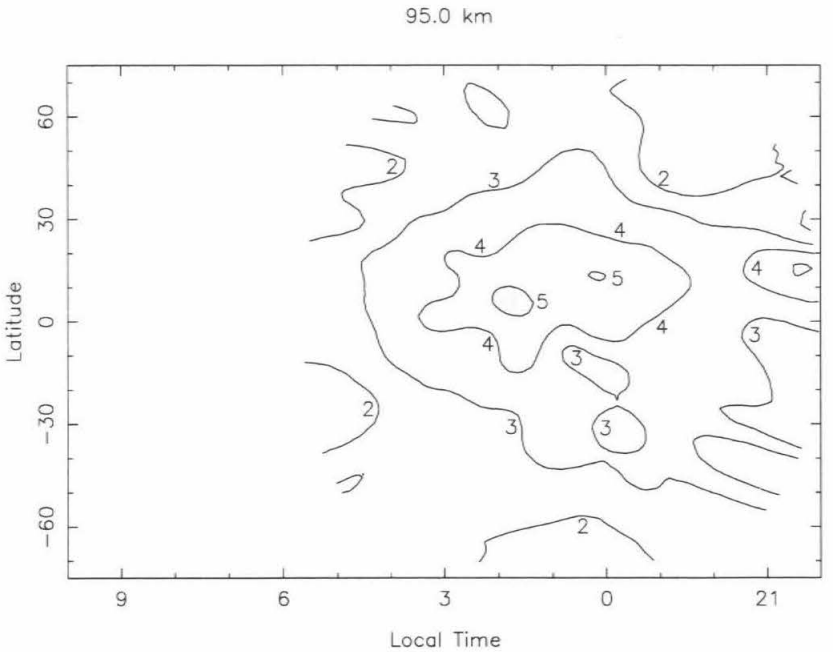

Figure 4.18. Map of the CO mixing ratio at 95 km altitude for November 8, 1994. Contour labels give the mixing ratio in 100 ppm.

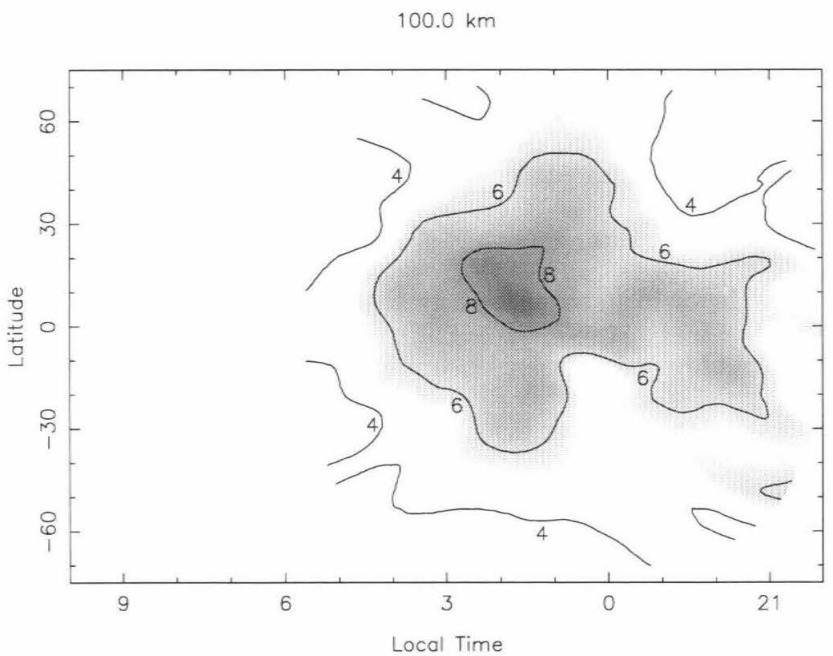

Figure 4.19. Map of the CO mixing ratio at 100 km altitude for November 8, 1994. Contour labels give the mixing ratio in 100 ppm.

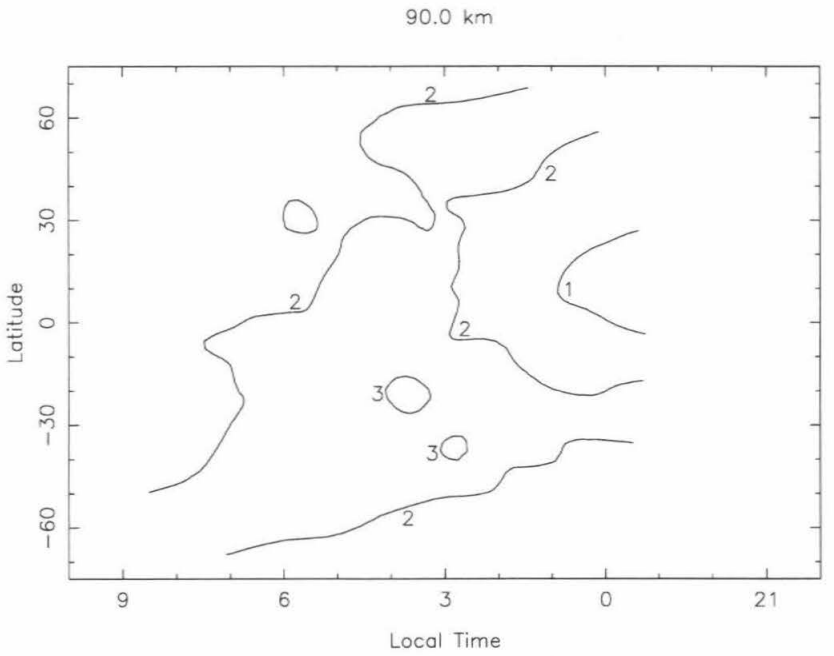

Figure 4.20. Map of the CO mixing ratio at 90 km altitude for December 9, 1994. Contour labels give the mixing ratio in 100 ppm.

4.4.2 Maps of the CO Mixing Ratio: December 9, 1994

Maps of the CO mixing ratio derived from the interferometric observations made on December 9, 1994, at altitudes of 90, 95, and 100 km are presented in Figs. 4.20, 4.21, and 4.22, respectively. These maps represent 1945 different solution profiles. Solutions were obtained every 0.8″, significantly finer than the synthesized beam size of 3.1″, in order to more fully fill the map in local time-latitude space. Map contours are in units of 100 ppm, and grey scale shows structure above 500 ppm (mixing ratio of 5×10^{-4}). CO exhibits a local maximum on the nightside of Venus at all three altitudes, with the peak CO mixing ratio increasing with altitude. The position of the maximum is near 4^{h} local time at each altitude, but the maximum latitude exhibits a slight northward variation, $-30°$ to $-10°$ from 90 to 100 km.

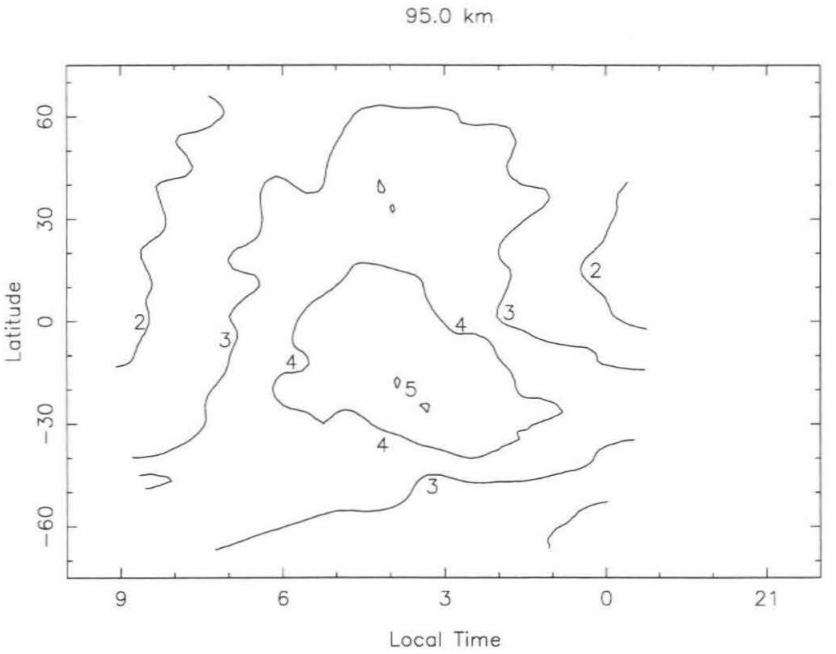

Figure 4.21. Map of the CO mixing ratio at 95 km altitude for December 9, 1994. Contour labels give the mixing ratio in 100 ppm.

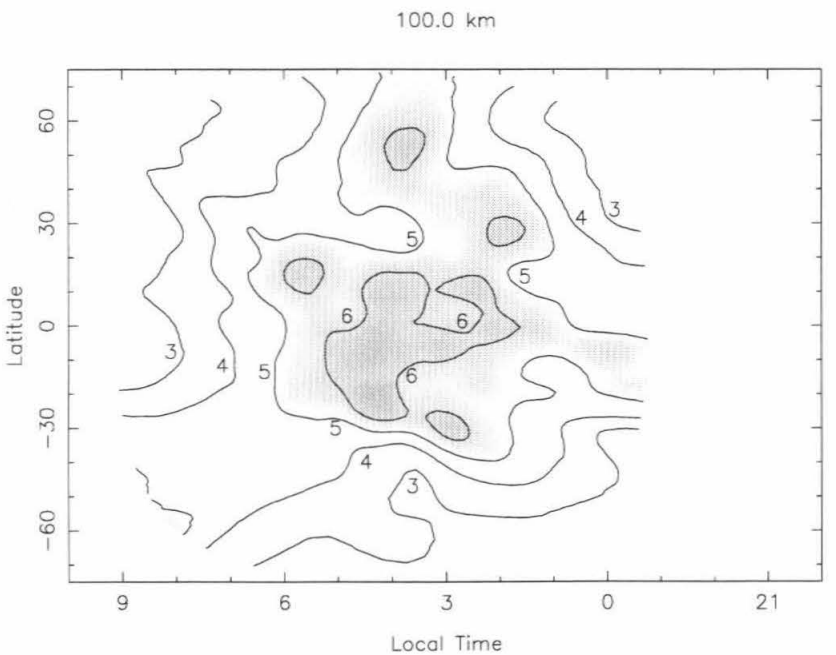

Figure 4.22. Map of the CO mixing ratio at 100 km altitude for December 9, 1994. Contour labels give the mixing ratio in 100 ppm.

4.5. The CO Distributions: Discussion

The distribution of carbon monoxide in the mesosphere of Venus shown in the previous section exhibits significant variation in local time, latitude, and particularly altitude. This section will explore the CO distribution for each date, and discuss the retrieved structure in terms of a qualitative model of mesospheric circulation. Variations between the two dates of observation are also seen, and lead to implications about changes in the mesospheric circulation between the two dates.

4.5.1 Current Results

CO Distribution on November 8, 1994.

All three of the maps of the CO distribution for November 8 show a clear maximum on the Venus nightside. In addition, a map at 85 km (not reproduced here) also shows a nightside maximum, although with lower contrast. The peak mixing ratio rises from about 4×10^{-4} at 90 km to 9.5×10^{-4} at 100 km, a factor of about two and one half. The contrast within each map (i.e., maximum over minimum CO mixing ratio) is also about this size, although the 100 km map exhibits a contrast of roughly 3.

The location of the maximum of the CO distribution shows some variability. At 90 km the CO peak appears to be centered near the antisolar point (0^h local time) and slightly in the northern hemisphere. This slight northward offset is also evident in the maps at 95 and 100 km. However, the peak mixing ratio appears to shift to about 2^h local time at these altitudes, most noticeably at 100 km.

CO Distribution on December 9, 1994.

As with the November results, the maps of the CO distribution for December show nightside maxima at all three altitudes. The peak mixing ratio rises from about 3×10^{-4} at 90 km to roughly 7×10^{-4} at 100 km, a factor of about two and one half. Contrasts within each map are between 2.5 and 3.

The location of the CO maximum has changed considerably from the November results. In the 90 to 100 km range the CO peak occurs near 4^h local time. The peak is also centered at low southern latitudes, and appears to advance northward slightly with altitude, from roughly $-30°$ at 90 km to $-10°$ at 100 km. In addition the map at 100 km has a much less distinct maximum, with a few pockets of high mixing ratios spread over a broader "bulge." Also, an extension of high mixing ratios spreads north to high latitudes between 3 and 4^h local time, and second extension appears to spread back toward the anti-solar point at low latitudes.

4.5.2 Comparison with Previous Observations

Relatively few resolved descriptions of the CO distribution from previous observations exist. The most extensive mapping comes from interferometric observations of Venus from 1986 and 1988 (Muhleman *et al.* 1987, Shah 1992, Gurwell *et al.* 1995). A map of a synthesis of these previous observations was provided in the introductory section (Fig. 4.1). These results showed that in 1986 an anomalously large CO maximum existed that was centered near 3.5^h local time. The peak of this bulge rose from 3×10^{-4} at 90 km to nearly 2×10^{-3} at 100 km. The contrast between high latitudes and the CO maximum approached 20-30, and diurnal differences may have been as large as 50-100. These 1986 results were independently confirmed through single dish observations of several CO rotational transitions (Clancy and Muhleman 1991). The 1988 results were of the evening terminator, and did not show but did not exclude the existence of a post-midnight maximum. The 1988 results did measure a remarkable increase in the CO mixing ratio by a factor of 5-8 across the evening terminator.

The only other mapping of the mesospheric CO distribution is from 1991 single dish observations of Venus made with the IRAM 30-m antenna (Lellouch *et al.* 1994). The large size of Venus at inferior conjunction ($\sim 60''$) allowed very modest resolution

of the planet (beam FWHM $\sim 12 - 13''$ at 230 GHz). These results showed a CO mixing ratio which increased regularly with altitude from 80 to 115 km, but at each altitude the CO distribution was found to be uniform in latitude and local time.

Clearly, the results of the November 8 and December 9, 1994 observations are different in several ways from previous observations. While the current observations do show nightside CO maxima, they are not nearly as large as the extreme "bulge" seen in the 1986 interferometric mapping. The 1994 maps show significant contrast between the peak mixing ratio and high latitude mixing ratios, which the 1991 IRAM measurements did not detect, but the contrasts are not nearly as large as in 1986. Neither of the maps show the evening terminator, so a direct comparison with the 1988 interferometric results is not possible.

These changes in the CO mixing ratio structure from different years suggests significant variation on timescales of a year or more in the processes controlling the CO distribution on the nightside of Venus. The only clear observation that is consistent with all single dish and interferometric observations is that CO is more abundant on the nightside relative to dayside in the upper mesosphere.

The reasons for the observed diurnal variation are not completely clear, but efforts have been made to address these observations with a qualitative model of the chemistry and dynamics of the mesosphere of Venus. Carbon monoxide is formed in the photodissociation of CO_2 and production is therefore limited to the dayside. That the nightside has the higher abundance implies that circulation and/or further chemistry play important roles in redistributing CO. Clancy and Muhleman (1985b) tested several chemical-dynamical models of the mesosphere of Venus, and determined that photochemistry and diffusion alone cannot explain the global CO distribution. They postulated that circulation in the mesosphere was the dominant force controlling the CO distribution. In their model, a sub-solar to anti-solar (SS-AS) flow permeates

the mesosphere, and a secondary zonal wind exists to varying altitudes as well.

In the absence of a zonal wind, the SS-AS flow transports CO produced on the dayside upward to the upper mesosphere and across the terminators to the nightside. Destruction of CO on the nightside is impeded by the lack of the radicals Cl and OH (the direct recombination of CO and O is spin forbidden and proceeds very slowly). The SS-AS flow converges at the antisolar point, i.e., 0^h local time at the equator, where downward subsidence occurs. A return flow is expected at lower altitudes. The result is the development of a CO maximum, or bulge, formed by the concentrating effects of the converging circulation and centered at the stagnation point of the flow (the anti-solar point).

The introduction of zonal retrograde wind to this model shifts the location of the stagnation point (and the CO maximum) from the anti-solar point towards the morning terminator. The SS-AS flow can be approximately modeled as a linear relation in solar zenith angle ($V_{SS-AS} = V_T[1 - |SZA/90 - 1|]$, with V_T the maximum terminator velocity of the flow), which provides a good fit to hydrodynamic models (Bougher *et al.* 1988, Lellouch *et al.* 1994). The shift in local time of the stagnation point in the presence of a secondary retrograde zonal flow of velocity V_Z is given roughly by $\Delta LT \approx 6^h \times V_Z/V_T$ (Lellouch *et al.* 1994). If the zonal wind exceeds the terminator velocity then the stagnation point disappears; in this case it is expected that a weak CO maximum could occur at the morning terminator. The presence of zonal winds, in addition to precipitating a shift in the CO maximum, should reduce diurnal contrasts by reducing the CO maximum.

In the context of this qualitative model, the previous observations suggest large scale variations in the global circulation of the mesosphere of Venus. The 1986 observations, with a maximum near 3.5^h, imply a zonal wind speed a little more than half of the SS-AS terminator speed from 90-100 km. The 1991 observations of

a nearly uniform CO distribution indicate zonal winds equal to or greater than the SS-AS terminator velocity.

Such long term variability in the mesospheric circulation has been measured directly using heterodyne techniques. Infrared measurements of CO_2 near 110 km were obtained in 1985, 1986, and 1987 (Goldstein *et al.* 1991). The measurements were best fit by a SS-AS flow with terminator velocities of 120 m s^{-1} and a superimposed zonal retrograde flow of 25 m s^{-1}. In contrast, millimeter interferometric measurements of Doppler shifts in CO rotational lines from near 99 km made in 1988 (Shah *et al.* 1991). The observations were best fit by a strong 132 m s^{-1} zonal flow. An upper limit of 40 m s^{-1} on SS-AS circulation was also determined. Most recently, single dish observations of Doppler shifts in CO rotational spectra were made in 1991 with the IRAM 30-m antenna (Lellouch *et al.* 1994) which found yet a third result for mesospheric winds. The mesospheric circulation in 1991 was apparently composed of a superposition of retrograde zonal and SS-AS flows of essentially equal strength which increased with altitude (40 m s^{-1} at 95 km and 90 m s^{-1} at 105 km).

Additional evidence for variable mesospheric and thermospheric zonal winds comes from airglow measurements of NO (e.g., Stewart and Barth 1979, Bougher *et al.* 1990) and O_2 (Allen *et al.* 1992, Bougher and Borucki 1994). The NO measurements are most sensitive to the 115-120 km region, and typically show a maximum intensity near the equator and shifted to roughly 2^h local time in time averaged maps, implying zonal winds of 40-60 m s^{-1}. Individual images, however, show a strong variability in the intensity and peak location of the NO airglow on timescales of an Earth day or less, suggesting highly variable thermospheric circulation from day to day (Bougher *et al.* 1990). The average zonal wind speeds are higher than those found by Goldstein *et al.* (1991), but are for a slightly higher altitude. Observations of O_2 visible nightglow and IR emission show intensity distributions which are also sensitive tracers of horizontal

winds, but in the altitude range of 90-130 km. The results show that in the time-averaged sense, the Venus upper mesospheric zonal winds are typically weak, less than 25 m s^{-1}, consistent with a small offset of peak intensities from local midnight. Occasionally, the upper mesosphere exhibits stronger zonal flow that can exceed 30-50 m s^{-1} and produce a peak offset to 3^h local time. Again, "snapshots" of the IR airglow show that the global wind system at these altitudes can vary greatly on the timescale of hours (Allen *et al.* 1992, Bougher and Borucki 1994).

The current data sets from November 8 and December 9, 1994 imply that zonal winds were significant at these times. The maps of the CO distribution from November 8 show that the CO maximum is large (mixing ratio nearly 1×10^{-3} at 100 km) and centered near 2^h local time, which suggests $V_T \approx 3V_Z$ at 95 and 100 km. Interestingly, the map at 90 km shows that the bulge is somewhat stretched in local time, with the peak near 0^h, suggesting that zonal winds were even lower at 90 km. The stretched appearance of the bulge (best seen in the contour of 3×10^{-4}) may be an indication of the zonal wind shear inferred between 90 and 95 km.

The December 9, 1994 results are somewhat different. The CO peak was centered near 4-4.5^h local time, which indicates zonal winds were stronger relative to the SS-AS terminator velocity, with $V_T \approx 1.4V_Z$ at that time. This inferred increase in the zonal winds relative to the SS-AS winds may also explain the slightly decreased CO mixing ratio maximum seen at 90 and 100 km between November and December. A decrease in the magnitude of the CO bulge is consistent with increasing zonal winds. However, these observed differences are small enough to be considered marginal and may only reflect minor errors in retrieval.

The direct measurements of mesospheric winds span the range of possible mesospheric circulations for a two-component (SS-AS and zonal winds) system. The observations of Goldstein *et al.* (1991) are of very strong SS-AS winds and very weak

zonal winds. The opposite endmember comes from the observations of Shah *et al.* (1991), where zonal winds were very strong and SS-AS flow was very weak. The IRAM measurements suggest a nearly exact balance of the two flows, and represents the "middle ground" between the other observations. These measurements suggest long term variability between extremes in the mesospheric circulation on yearly or longer timescales.

The results of this work, which show CO maxima on the nightside, are consistent with significant but secondary zonal winds. In this sense they reside somewhere between the wind fields measured by Goldstein *et al.* (1991) and Lellouch *et al.* (1994). What is most significant, however, is that the CO maximum from December 9, 1994 is shifted significantly more toward the morning terminator than the bulge seen in November 8, 1994. This suggests that zonal winds had increased and/or SS-AS winds had decreased significantly over the intervening month between observations. This is the first indication of variability in the CO distribution and inferred mesospheric circulation on this smaller timescale.

One of the unresolved issues that the qualitative model does not address is latitudinal variability of the CO maximum. Both the observations from November and December 1994 and the 1986 observations (Gurwell *et al.* 1995) show that at some altitudes the CO maximum is displaced from the equator. The reason for a north-south imbalance is not understood. The axisymmetric subsolar to antisolar circulation which transports CO from dayside to nightside is expected to converge on the equator, since the subsolar point is always very near the equator. We note that strong latitudinal asymmetries have been observed in observations of thermospheric ($z \geq 125$ km) oxygen (Alexander *et al.* 1993), the causes of which are still unknown. It is unclear if CO north-south mesospheric asymmetry is related to the higher altitude O asymmetry, but as more work is done on the Venus atmosphere it becomes

increasingly clear that the mesosphere and thermosphere are more coupled than previously considered, and that a common factor relating asymmetries may eventually be found. In addition, it has recently been reported that CO in the deep atmosphere exhibits hemispherical variability as well, with the northern hemisphere exhibiting more carbon monoxide than the southern hemisphere (Collard *et al.* 1993). These asymmetries are most probably tied to dynamics, but what is causing variations in the circulation is not known currently.

4.6. Conclusions

Interferometric observations of the ^{12}CO $J(1-0)$ rotational transition from the mesosphere of Venus were made on November 8, 1994 and December 9, 1994, with the Owens Valley Millimeter Array. The interferometric data achieved very high spatial resolution on the disk of Venus (approximately 1000 km at the sub-earth point) for each date. The fully mapped spectral data are of high signal to noise, and show little obvious variation with position on the disk beside deepening of the lines near the limbs.

The spectra were numerically inverted for local profiles of the CO mixing ratio over the altitude range of 85 to 105 km. Due to the single transition nature of the experiment, the temperature profile of the mesosphere could not be simultaneously determined as well, and instead a mean profile for the night and day mesosphere was adopted in order to allow inversion of the observed lines. The results show that for each date the CO distribution exhibited a maximum, or bulge, on the nightside of Venus centered at low latitudes and shifted toward the morning terminator.

In November, the CO distribution had a maximum near 0^h local time at 90 km and near 2^h local time at 95 and 100 km. The peak mixing ratio increased with altitude from roughly 4×10^{-4} at 90 km to 9.5×10^{-4} at 100 km, consistent with previous single dish and interferometric studies of CO. The peak also appeared

to center at +10° latitude. In December, the CO distribution was maximized near 4^h local time in the 90-100 km range. The peak mixing ratio also increased with altitude, from 3×10^{-4} at 90 km to 7×10^{-4} at 100 km. In contrast with the November observations, the peak appeared to center at −30° latitude (90 km) and advance northward to −10° at 100 km.

These results corroborate previous observations of a nightside CO maximum in the Venus mesosphere (Muhleman *et al.* 1987, Clancy and Muhleman 1991, Gurwell *et al.* 1995). In the context of the qualitative model presented by Clancy and Muhleman (1985a), these new interferometric observations are consistent with dominant sub-solar to anti-solar flow in the mesosphere with a significant but secondary superimposed zonal flow. Using an idealized parameterization of the SS-AS flow, the CO maxima for each date, which correspond to stagnation points in the mesospheric wind field, suggest SS-AS terminator winds which are roughly 3 and 1.4 times the zonal wind speed for November and December, respectively. These results suggest modest but significant changes in the relative strength of the zonal and/or SS-AS circulation within the mesosphere on timescales of a month or less.

Chapter 5

Millimeter Observations of Planetary Atmospheres: Conclusions.

5.1. Summary

This thesis has brought together three distinct observing programs of carbon monoxide in planetary atmospheres. The observations shared many of the same aspects, but each addressed a significant and specific set of questions about the atmospheres of these planets. I summarize the major findings of each chapter below.

Titan

Observations of the ^{12}CO $J(1-0)$ rotational line from Titan's stratosphere were obtained in October 1994 in an effort to measure the globally averaged abundance of CO. The obtained spectrum clearly shows a strong emission feature which is very consistent with a well-mixed vertical profile of CO, with a mixing ratio equal to that found for the troposphere through ground-based IR observations (Lutz *et al.* 1983). Numerical inversion of the line shape using an updated radiative transfer code was utilized to determine a best-fit stratospheric mixing ratio of $5 \pm 1 \times 10^{-5}$ from 60–200 km. This result confirms the original millimeter-wave detection of stratospheric CO by Muhleman *et al.* (1984) and is very consistent with the tropospheric IR results ($f_{CO} = 6^{\times}_{\div}3 \times 10^{-5}$), suggesting CO is well-mixed from the surface to at least 200 km. This measurement is clearly irreconcilable with the CO spectrum obtained by Marten *et al.* (1988), which set an upper limit on the stratospheric CO mixing ratio of 4×10^{-6}. Due to the very long chemical lifetime of CO, it is not possible that the abundance changed during the few years between observations. The ability to isolate the spectrum in each sideband with an interferometer, as well as the extremely careful analysis of the spectrum, makes this new result very robust.

Mars

Observations of the ^{12}CO $J(1-0)$ rotational line from Mars' atmosphere were obtained in February 1993 in an effort to measure the thermal structure of the atmosphere from 0-70 km. These interferometric observations yielded a spatial resolution of 4.2″ when Mars was 12.5″ in diameter, allowing us to modestly resolve the temperature structure as a function of local time, latitude, and altitude. The line to continuum spectra from the observations showed significant variability with local time and latitude.

The observed spectra were inverted numerically for local thermal profiles from 0 to 70 km, assuming a constant CO mixing ratio. The derived low latitude temperature was found to be approximately 20 K cooler than profiles from the Viking era. This profile is well-matched by cooler profiles determined from whole disk measurements of CO which suggest very little dust loading of the atmosphere at the time of the observations (Clancy *et al.* 1990). The revealed thermal structure shows strong variation with latitude, and the results of this analysis compare well with profiles derived from Mariner 9 IRIS observations (Leovy 1982, Santee and Crisp 1993) and to thermal structure calculated from the Mars General Circulation Model (Haberle *et al.* 1993).

The average thermal structure of the atmosphere as a function of latitude was used to infer mean zonal winds, using the gradient thermal wind equation. These wind results, while compromised by the relatively low spatial resolution of the observations, do qualitatively match inferred zonal winds from the Mariner 9 IRIS observations and calculated winds from the GCM modeling of the thermal structure.

Venus

Observations of the ^{12}CO $J(1-0)$ rotational line from the mesosphere of Venus were obtained on November 8, 1994 and again on December 9, 1994. The measure-

ments were made in an effort to monitor the distribution of CO in the mesosphere, which is known to exhibit variations on timescales of a year or longer. These observations achieved a spatial resolution of roughly 1000 km at the sub-earth point on each date.

The high quality spectra obtained were numerically inverted for local profiles of the CO mixing ratio in the altitude range of 85 to 105 km. A mean mesospheric temperature profile from Pioneer Venus descent probe measurements was assumed; possible variations of the mesospheric temperature are not a major source of error for the inversion process.

For each day the revealed CO distribution shows a nightside maximum centered at low latitudes and shifted from the anti-solar point toward the morning terminator. Both days clearly show a fall-off in the CO abundance from the equator toward high latitudes. In November the peak of the CO maximum was shifted to roughly 2^h local time above 95 km, while in December the shift was even larger, to roughly 4-4.5^h local time in the 90 to 100 km range. In addition, CO abundances were slightly higher in November.

The changes in the CO distribution between November and December, examined in the context of a qualitative model of the mesospheric circulation, suggests that zonal winds were significant for both periods, and that the ratio of the sub-solar to anti-solar terminator wind speed to the zonal wind speed decreased by a factor of roughly two over the month between observations. These measurements offer the first evidence for mesospheric variability from CO observations on this timescale.

5.2. Future Opportunities

The last two decades have seen an explosion in the technology that underlies all astronomical observations at millimeter wavelengths. It is certain that this trend will continue. Perhaps the place where innovation and expansion will be noticed the

most is in the continued improvement of the existing millimeter interferometers, such as at OVRO, and in the development of the Smithsonian Submillimeter Array (SMA) and the NRAO Millimeter Array (MMA).

For planetary observations in particular, the expansion of interferometers to many elements is particularly useful. First, the increased number of antennas allows for faster filling of the (u, v) plane, and allows mapping of sources in a single track or less. Second, the increased number of antennas allows for more accurate and constrained application of phase self-calibration. Since planets can be well-modeled, they provide excellent candidates for the use of self-calibration.

Millimeter spectroscopy of CO allows for ground-based long term monitoring of the planets. Venus and Mars are particularly well-suited due to the strong CO lines they exhibit. As space missions become less frequent and more limited in scope, the ability to measure and observe the thermal and dynamical structure of these planets becomes even more valuable, especially for detecting and quantifying long term variations in their states.

Appendix A: Radiative Transfer Development

This appendix is intended as an introduction to a general radiative transfer method I have used for modeling planetary atmospheres. The fundamental equation of radiative transfer relates the change in intensity I_ν along a particular ray path s to the local absorption coefficient k_ν and the local volume emission j_ν:

$$\frac{1}{k_\nu}\frac{dI_\nu}{ds} = -I_\nu + \frac{j_\nu}{k_\nu}. \tag{A.1}$$

In microwave radiative transfer atmospheres are assumed to be nonscattering and in local thermodynamic equilibrium (LTE). For these conditions the ratio j_ν/k_ν is equal to the Planck blackbody intensity B_ν for the local temperature T. At centimeter wavelengths it is possible to use the Rayleigh-Jeans approximation for the blackbody, which is strictly linear in T; at millimeter wavelengths however this approximation starts to break down, especially for the cold temperatures of the Mars upper atmosphere and for Titan. Equation A.1 is a linear first order differential equation with the solution (e.g., Chandrasekhar 1950):

$$I_\nu(s_0) = I_\nu(0)\epsilon^{-\int_0^{s_0} k_\nu ds} + \int_0^{s_0} k_\nu(s)B_\nu(T(s))\epsilon^{-\int_s^{s_0} k_\nu ds'} ds. \tag{A.2}$$

Equation A.2 can describe radiation from a stratified planetary atmosphere by setting $I_\nu(0)$ equal to the upward intensity at the surface along the ray path; a logical choice for this term is $\varepsilon B_\nu(T_0)$, where ε is the surface emissivity at frequency ν in the direction of the ray path and T_0 is the surface temperature. Carrying the integration to the top of the atmosphere and converting to the vertical coordinate z:

$$I_\nu(\infty) = \varepsilon B_\nu(T_0)\epsilon^{-\int_0^{\infty} k_\nu dz/\mu} + \int_0^{\infty} k_\nu(z)B_\nu(T(z))\epsilon^{-\int_z^{\infty} k_\nu dz'/\mu} dz/\mu \tag{A.3}$$

where $\mu \equiv dz/ds$. This equation neglects atmospheric radiation that is reflected off the surface into the ray path, which can be important for thin atmospheres (Mars and Triton are examples), and is not well formulated to accommodate limb sounds. A full treatment is given below.

The numerical calculation of I_ν over z is accomplished by integrating the absorption coefficient over altitude intervals Δz, holding parameters such as absorber volume mixing ratios and temperature constant through each of the layers. The result is a discrete form of the radiative transfer equation (e.g., Clancy *et al.* 1983):

$$I_\nu = \varepsilon B_\nu(T_0) e^{-\sum_{i=1}^{N} \Delta\tau_i/\mu_i} + \sum_{i=1}^{N} B_\nu(T_i)\left(1 - e^{-\Delta\tau_i/\mu_i}\right) e^{-\sum_{j=i+1}^{N} \Delta\tau_j/\mu_j} \qquad (A.4)$$

where T_i = temperature of layer i, N = number of layers, and $\Delta\tau_i = \int k_\nu(z)dz$ = opacity of layer i due to all absorbing species. For a plane parallel atmosphere the geometric factor μ_i is the cosine of the incidence angle; for a spherical shell atmosphere (see Fig. A.1)

$$\frac{1}{\mu_i} \equiv \frac{\Delta s_i}{\Delta z_i} = \left(\alpha_i^2 \cos^2\phi_i + 2\alpha_i + 1\right)^{1/2} - \alpha_i \cos\phi_i, \qquad (A.5)$$

where $\alpha_i = r_i/\Delta z_i$ and ϕ_i is the angle of the ray path from the local normal.

The intensity as described in Eq. A.4 can be thought of as the sum of a surface brightness (reduced by atmospheric absorption) plus a weighted average of the atmospheric profile of $B_\nu(T_i)$. The discrete weighting function describing the atmospheric contribution is

$$W_i = \left(1 - e^{-\Delta\tau_i/\mu_i}\right) e^{-\sum_{j=i+1}^{N} \Delta\tau_j/\mu_j} \qquad (A.6)$$

such that the atmospheric intensity term is simply

$$I_\nu(atmosphere) = \sum_{i=1}^{N} B_\nu(T_i) W_i. \qquad (A.7)$$

The structure of the weighting function shows where the majority of the observed radiation originates. W_i can be a strong function of frequency, especially near resonant transitions such as the rotational lines observable in the microwave spectrum. For this reason observations at different frequencies usually probe different regions of the planetary atmosphere.

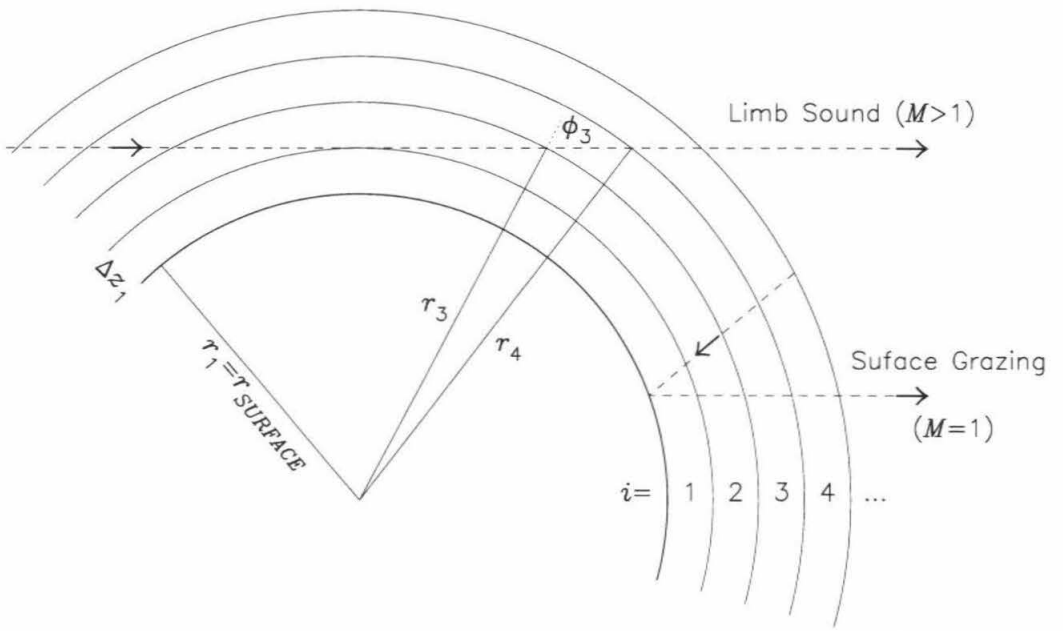

Figure A.1. Schematic representation of a spherical model atmosphere, showing the geometry of a surface intercepting ray path and a limb sound ray path.

Planetary surfaces are modeled as smooth isothermal dielectric spheres. The properties of smooth dielectric boundaries are well known; for circular polarization we take the scalar average of the Fresnel perpendicular and parallel reflectivities:

$$R = \frac{1}{2}\left(\frac{\sqrt{\frac{n_s^2}{n_a^2} - \sin^2\Theta} - \cos\Theta}{\sqrt{\frac{n_s^2}{n_a^2} - \sin^2\Theta} + \cos\Theta}\right)^2 + \frac{1}{2}\left(\frac{\sqrt{\frac{n_s^2}{n_a^2} - \sin^2\Theta} - \frac{n_s^2}{n_a^2}\cos\Theta}{\sqrt{\frac{n_s^2}{n_a^2} - \sin^2\Theta} + \frac{n_s^2}{n_a^2}\cos\Theta}\right)^2 \qquad \text{(A.8)}$$

where Θ is the incidence angle measured from normal, and n_s and n_a are the indices of refraction of the surface and the lower atmosphere, respectively. The surface emissivity ε is then $1 - R$. In nearly all cases n_a is essentially unity (the deep atmospheres of Venus and the giant planets are exceptions). The surface index of refraction is

given in terms of the dielectric constant ($n_s = \sqrt{\epsilon_s}$), assuming that the magnetic permeability is unity.

A general discrete radiative transfer equation which introduces reflected atmospheric emission for surface intercepting rays and accommodates limb sounding geometries is developed next. Figure A.1 is useful for understanding the somewhat complex notation. Taking $B_i = B_\nu(T_i)$:

$$\begin{aligned} I_\nu &= (1 - R_{M-1}) B_{M-1} e^{-\sum_M^N \Delta\tau_i/\mu_i} \\ &+ \sum_{i=M}^{N} B_i \left(1 - e^{-\Delta\tau_i/\mu_i}\right) e^{-\sum_{j=i+1}^N \Delta\tau_j/\mu_j} \\ &+ R_{M-1} \sum_{i=M}^{N} B_i \left(1 - e^{-\Delta\tau_i/\mu_i}\right) e^{-\left(\sum_{j=M}^N \Delta\tau_j/\mu_j + \sum_{j=M}^{i-1} \Delta\tau_j/\mu_j\right)}. \end{aligned} \tag{A.9}$$

Here M refers to the lowest atmospheric layer the ray passes through. For a ray that hits the surface $M = 1$; for a limb sound, the chosen ray must have a tangent point at the boundary of any two layers, and M is the index for the higher of these two layers. If $M = 1$, then R_{M-1} is the surface reflectivity from Eq. A.8; if $M > 1$, then $R_{M-1} = 1$.

For numerical convenience, define $\Delta\tau_{M-1} = -\ln R_{M-1}$, $B_{-i} = B_i$, $\Delta\tau_{-i} = \Delta\tau_i$, and $\mu_{-i} = \mu_i$. The optical depth is defined as

$$\tau_i = \begin{cases} \sum_{j=i+1}^{N} \Delta\tau_j/\mu_j & i \geq M-1 \\ \tau_{M-1} + \sum_{j=-i+1}^{-M} \Delta\tau_j/\mu_j & i \leq -M \end{cases} \tag{A.10}$$

and is essentially the sum of all the opacities "above" a layer to the top of the atmosphere along the path. Using this notation Eq. A.9 is transformed to

$$I_\nu = \sum_{i=M-1}^{N} B_i \left(1 - e^{-\Delta\tau_i/\mu_i}\right) e^{-\tau_i} + \sum_{i=-N}^{-M} B_i \left(1 - e^{-\Delta\tau_i/\mu_i}\right) e^{-\tau_i}. \tag{A.11}$$

Appendix B: Partial Derivatives of the Radiative Transfer Equation

For the numerical line inversion algorithms I developed, it is necessary to know the partial derivative of the radiative transfer equation with respect to the variable

to be solved for. The focus of inverting solitary lines falls into two categories: either estimating the atmospheric temperature profile using "known" absorber profiles, or estimating the abundance profile of an absorbing species using a "known" temperature profile. In either case the sensitivity of the observed intensity to changes in the profile is contained within the partial derivative. An earlier version of the following treatment is given in Gurwell *et al.* (1995).

•The Derivative with Respect to Temperature (Simple Form)

Temperature affects the observed intensity in two ways. First, the Planck blackbody intensity B is a function of temperature. Since even at millimeter wavelengths the Planck function is nearly linear with temperature, this has a nearly linear effect on the total intensity: by increasing the temperature within a layer you will have a nearly linear increase in the observed intensity. A more subtle effect, however, is that in general the absorption coefficient of absorbing species is also a function of temperature. In this case the effect can be very nonlinear.

In the Simple Form, I ignore the temperature dependence of the absorption coefficient of the absorbing species when determining the derivatives at each iterative step. Since temperature adjustments between iterations are usually small, this approximation is usually not serious. This will add more iterations to the inversion process, since the partial derivatives will not be strictly correct. For a particular layer k, the derivative of the Planck brightness with respect to the layer temperature is

$$\frac{dB_k}{dT_k} = \frac{B_k}{T_k}\frac{x_k}{1-e^{-x_k}} \tag{B.1}$$

where $x_k = h\nu/k_B T_k$. The derivative of I_ν with respect to B_k is easily found using Eq. A.11, and using the chain rule we form the derivative of the intensity with respect to the temperature within isothermal layer k:

$$\frac{\partial I_\nu}{\partial T_k}[\text{Simple Form}] = \frac{B_k}{T_k}\frac{x_k}{1-e^{-x_k}}\left(1-e^{-\Delta\tau_k/\mu_k}\right)\left(e^{-\tau_k}+e^{-\tau_{-k}}\right). \tag{B.2}$$

Note that this is only valid for $k \geq M$. Obviously, a limb sounding ray with a high tangent altitude is insensitive to the temperature of the lower atmosphere, and the derivative is zero.

•The Derivative with Respect to Opacity

The partial derivative of the total intensity with respect to the opacity within a layer is important for inversion of lines for species abundance. Usually, the absorption coefficient for a resonant line is directly proportional to the number density of the absorber and hence is also proportional to the volume mixing ratio of that species. In this case the derivative of the opacity $\Delta\tau_k$ for layer k with respect to the mixing ratio f_k^a of absorber a is

$$\frac{\partial \Delta\tau_k}{\partial f_k^a} = \frac{\Delta\tau_k^a}{f_k^a} \tag{B.3}$$

where $\Delta\tau_k^a$ is the opacity of layer k due only to species a. The difficult aspect is taking the derivative of Eq. A.11 with respect to the layer opacity. For compactness, I introduce the discrete function σ_m:

$$\sigma_m = \begin{cases} \sum_{i=m}^{N} B_i \left(1 - \epsilon^{-\Delta\tau_i/\mu_i}\right) \epsilon^{-\tau_i} & m \geq M-1 \\ \sigma_{M-1} + \sum_{i=m}^{-M} B_i \left(1 - \epsilon^{-\Delta\tau_i/\mu_i}\right) \epsilon^{-\tau_i} & m \leq -M. \end{cases} \tag{B.4}$$

This is very analogous to Eq. A.11; in fact, $I_\nu = \sigma_{-N}$. The complete partial derivative of Eq. A.11 with respect to the opacity within layer k is

$$\mu_k \frac{\partial I_\nu}{\partial \Delta\tau_k} = B_k \left(\epsilon^{-\tau_{k-1}} + \epsilon^{-\tau_{-k-1}}\right) + \sigma_k + \sigma_{-k} - 2I_\nu. \tag{B.5}$$

The full partial derivative with respect to the mixing ratio of species a in layer k is then obtained through the chain rule, using Eq. B.3 and Eq. B.5.

•The Derivative with Respect to Temperature (Full Form)

For full accuracy in the partial derivative of the intensity with respect to the temperature within layer k, it is necessary to include the temperature dependence of the absorption coefficient of the absorbing species within that layer. In general,

the temperature sensitivity of the absorption coefficient depends on the particular species and transition. I will not go into the details here, but assume that we can determine $\partial\Delta\tau_k/\partial T_k$. Then the full partial derivative of the intensity with respect to the temperature of layer k is

$$\frac{\partial I_\nu}{\partial T_k}[\text{Full Form}] = \frac{\partial I_\nu}{\partial T_k}[\text{Simple Form}] + \frac{\partial I_\nu}{\partial \Delta\tau_k}\frac{\partial \Delta\tau_k}{\partial T_k}. \tag{B.6}$$

Appendix C: Integration of Opacity over a Layer

For the discrete radiative transfer equation and its partial derivatives discussed in the preceding appendices it is necessary to know $\Delta\tau_i$, the opacity of (each) layer i. For the current work there are two different forms of absorption modeled: individual rotational resonant line absorption and induced dipole absorption. The model formulation for these absorption types are different and discussed below.

•Individual Lines

For the following section I am presenting a formulation for opacity first described in Clancy *et al.* (1983). For more information on lineshapes and absorption coefficients see Waters (1976) and references therein. To model the absorption due to individual lines, note that the absorption coefficient can be formulated as the product of a line strength per molecule $S(z)$ times the local absorber number density $N^a(z)$ times an area normalized lineshape $\eta(\nu, z)$. The line strength is generally dependent on the local temperature. The lineshape is generally dependent on the local temperature and pressure.

For individual lines absorption is distributed in frequency about the line center ν_0 due to Doppler (thermal motion) broadening and collisional (or pressure) broadening. The lineshape associated with pure Doppler broadening is gaussian, while for moderate pressures (less than a few bars) pure collisional broadening is well modeled as a Lorentzian. The Voigt function describes the lineshape when both Doppler and

collisional broadening are evident and is the convolution of the collisional Lorentzian with the Doppler gaussian lineshapes:

$$\eta(\nu, P(z)) = \int_{-\infty}^{\infty} \frac{1}{\pi} \frac{C_P P}{(\nu - \nu_0 - y)^2 + C_P^2 P^2} \times \frac{1}{C_D} \sqrt{\frac{\ln 2}{\pi}} e^{-\ln 2(y/C_D)^2} dy. \quad \text{(C.1)}$$

Here C_P=collisional broadening constant [Hz/dyne/cm^2], P=pressure [dyne/cm^2], and C_D=Doppler broadening constant= $3.851 \times 10^{-7} \nu_0 \sqrt{T/m_a}$ (m_a is the molecular weight of the absorbing species).

For the integration of the absorption coefficient over layer i we assume a constant temperature T_i, absorber mixing ratio f_i^a and local gravitational acceleration g_i, the ideal gas law, and an atmosphere in hydrostatic equilibrium:

$$N^a(z) = f_i^a \rho(z) A_0 / \overline{m} \quad \text{(C.2a)}$$

$$dP(z) = -\rho(z) g(z) dz, \quad \text{(C.2b)}$$

where $\overline{m}$ is the mean molecular weight within the layer and A_0 is Avagadro's number. The integration over the layer is then straightforward:

$$\begin{aligned}
\Delta\tau_i^a(\nu) &= \int_{z_i}^{z_i + \Delta z_i} S(z) N^a(z) \eta(\nu, z) dz \\
&= \frac{S_i f_i^a A_0}{g_i \overline{m}} \int_{P_T}^{P_B} \eta(\nu, P) dP \\
&= F_i \frac{\sqrt{\ln 2} C_P}{\pi^{3/2} C_D} \int_{-\infty}^{\infty} \int_{P_T}^{P_B} \frac{P}{(\nu - \nu_0 - y)^2 + C_P^2 P^2} e^{-\ln 2(y/C_D)^2} dP \, dy \\
&= \frac{F_i \sqrt{\ln 2}}{2\pi^{3/2} C_D C_P} \int_{-\infty}^{\infty} \ln \left[\frac{(\nu - \nu_0 - y)^2 + C_P^2 P_B^2}{(\nu - \nu_0 - y)^2 + C_P^2 P_T^2} \right] e^{-\ln 2(y/C_D)^2} dy \quad \text{(C.3)}
\end{aligned}$$

where $F_i = S_i f_i^a A_0 / g_i \overline{m}$, and P_B and P_T are the pressures at the bottom and top of the layer, respectively. The remaining integral is evaluated numerically. This rather complex formula is very useful because it allows for fairly thick atmospheric layers (where $\Delta P/P$ can be large).

•Collision Induced Dipole Absorption

The major species of most planetary atmospheres (N_2, CO_2, and H_2) have no permanent dipole moments, and therefore individual molecules of these species have no pure rotational lines. However, collisions between molecules can induce dipole moments, briefly allowing rotational transitions. The short duration of the interaction means that the broadening width is very large (on the order of 300 to 1000 GHz or more), such that all the transitions are blended into a "continuum" absorption. For more information on collision induced dipole absorption see Rosenkranz (1993) and references therein.

Unlike individual lines as discussed in the preceding section, induced dipole absorption involves collisions and is proportional to the product of the number densities (i.e., $\propto N_a^2$ for like molecules or $N_a N_b$ for unlike molecules). In the microwave region a general empirical formula for collision induced dipole absorption is

$$k_\nu = C_{a,b} f^a f^b \theta^x P^2 \nu^2 \tag{C.4}$$

with f^a and f^b the volume mixing ratios of species a and b, $C_{a,b}$ is a proportionality constant for the interaction of a and b, $\theta = 300/T$, and x is an empirically determined exponent for the temperature dependence.

Proceeding as in the previous section, we integrate the absorption coefficient over a layer by holding temperature and mixing ratios constant and assuming a hydrostatic atmosphere. The resulting layer opacity is

$$\Delta\tau_i(\nu) = C_{a,b} f_i^a f_b^b \theta_i^x H_i \left(\frac{P_B^2 - P_T^2}{2} \right) \nu^2 \tag{C.5}$$

where $H_i = RT_i/\overline{m}_i g_i$ is the local scale height of the atmosphere. Due to the P^2 dependence, induced dipole absorption is usually only important in high pressure regimes. Particular examples include the tropospheres of Titan ($N_2 - N_2$), Venus ($CO_2 - CO_2$) and the giant planets ($H_2 - H_2$ and H_2–He).

Appendix D: Beam Weighting–Convolution with a 2-D Gaussian

The final step in producing a cleaned map of the source from the observed visibilities is the convolution of the derived source structure with a clean beam. The clean beam is a circularly symmetric gaussian shape with a FWHM that approximates the "true" resolution, or width, of the dirty beam. This convolution means that the flux value at any pixel in the map is equal to the integral of the intensity of the entire sky weighted by a 2–D gaussian centered at that pixel. To directly compare model results with the maps, a similar convolution of the model intensities with a clean beam must be done.

The radiative transfer model assumes a spherically symmetric planetary atmosphere for purposes of calculating the intensity I_ν. Therefore, the calculated intensity depends only on the apparent radius r of the ray path from the disk center on the sky. Given enough radial steps, $I_\nu(r)$ can be approximated by a series of constant intensity annuli.

Figure D.1 presents the geometry for beam weighting. Consider a gaussian beam at apparent radius R from the disk center. The gaussian falloff from the beam center is shown by the dotted lines at 80, 60, 40, and 20% of the peak value. We wish to determine the beam weighted contribution of the average intensity $I_\nu(a,b)$ of the annulus bounded by r_a and r_b to the flux measured at R. A gaussian beam of half-width at half-maximum HWHM is described by the function

$$W(\rho) \;=\; \epsilon^{-\ln 2\ \rho^2/\mathrm{HWHM}^2}. \tag{D.1}$$

Using the law of cosines this becomes

$$W(r,\theta) \;=\; \epsilon^{-\ln 2\ (R^2+r^2-2Rr\cos\theta)/\mathrm{HWHM}^2}. \tag{D.2}$$

The contribution to the flux is then

$$F(r_a,r_b,R) \;=\; I_\nu(a,b)\int_0^{2\pi}\int_{r_a}^{r_b} W(r,\theta)\ r\ dr\ d\theta$$

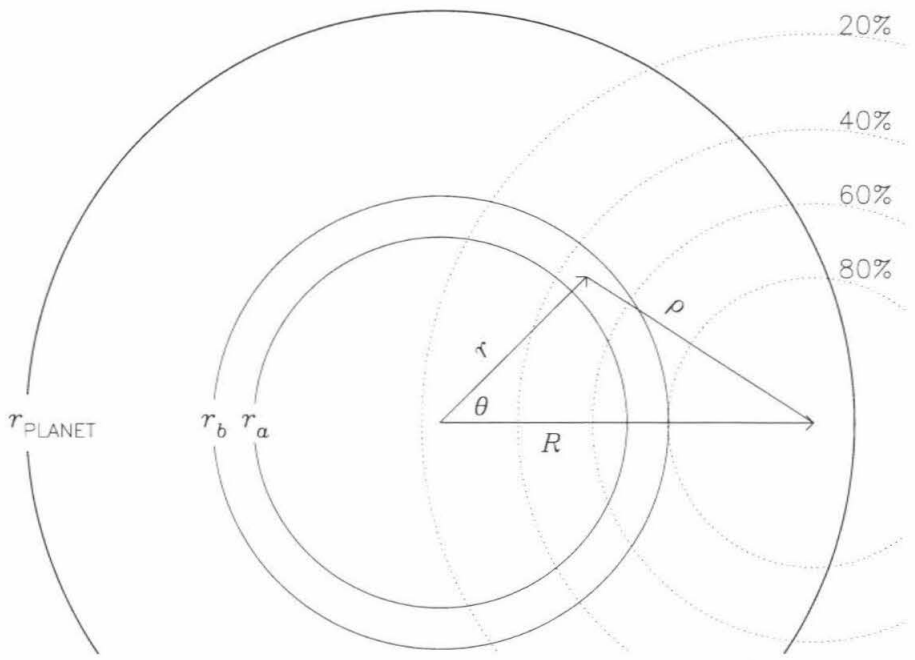

Figure D.1. Geometry associated with gaussian beam weighting.

$$= 2\pi I_\nu(a,b) \int_{r_a}^{r_b} r\epsilon^{-\ln 2\ (R^2+r^2)/\mathrm{HWHM}^2} I_0\left(\frac{2\ln 2\ Rr}{\mathrm{HWHM}^2}\right) dr \quad \text{(D.3)}$$

where $I_0(x)$ is the modified Bessel function of order zero (see Press *et al.* 1992, p. 229). The remaining integral can be solved numerically. The total flux measured at R is the sum of the contributions from all annuli. In practice, the calculated intensity changes only slowly in radius until near the planetary disk edge. Hence large steps can be utilized near the disk center and finer steps near the disk edge.

Appendix E: Channel Weighting–Convolution with Instrument Functions

Spectra can be measured directly in the frequency domain (filterbank spectrometers) or in the time domain and then converted to the frequency domain (correlator spectrometers). In either case, the effect is to convolve an instrument (or

channel) function with the "true" spectrum and sample the result at the channel locations in frequency space. Hence the spectral flux density measured in a channel is the average "true" spectrum weighted by the instrument function centered at that channel.

For a lineshape that is broad compared with the channel width, convolution has little impact (i.e., the smearing effect is limited). This is true for many applications. However, on occasion the lineshape will be narrow compared with the channel width and the convolution will produce a much broader feature, and depending on the instrument function may exhibit "ringing". Here I will discuss three simplified instrument functions, and the convolution of these functions with a canonical lineshape.

•Uniform Spectral Sampling

The simplest instrument function is a square or box channel in frequency space. This could be used as an approximation to the instrument function of a filterbank channel. The functional form in frequency is a channel of width $\Delta\nu$ and uniform height A:

$$W_B(\nu) = A \qquad \nu' - \Delta\nu/2 \leq \nu \leq \nu' + \Delta\nu/2. \tag{E.1}$$

The integral of $W_B(\nu)$ is normalized for $A = 1/\Delta\nu$. This is a "perfect" channel in the sense that it has no sidelobes in spectral space.

•Uniform Time Sampling

Instead of directly measuring the spectrum, it is possible to measure the correlation of the incoming signal as a function of time offset, or lag, t. The Fourier transform of this time correlation function for infinite t is the spectrum (e.g., Thompson *et al.* 1986). However, in practice t is limited to a certain range, equivalent to multiplying the true time correlation function by a window function. This window function alters the spectrum observed. Consider a uniformly sampled time window

from $-T/2$ to $T/2$ with uniform weight. This could be used as an approximation to the instrument function in the time domain for a digital correlator spectrometer. The Fourier transform of this window is the instrument function in the frequency domain:

$$W_U(\nu) = \int_{-T/2}^{T/2} e^{-i2\pi\nu t} dt = T\,\mathrm{sinc}(\pi\nu T) = \frac{1}{\Delta\nu}\mathrm{sinc}\left(\frac{\pi\nu}{\Delta\nu}\right). \qquad \text{(E.2)}$$

Note that the area under $W_U(\nu)$ is unity. The usual sample spacing (i.e., channel spacing) is $\Delta\nu = 1/T$, placing the peak of one sinc function at the first null of the adjacent sinc functions. The FWHM of the sinc function is $\sim 1.2/T$, wider than the channel spacing. The first sidelobe level is at -21.7% of the peak.

•Non-Uniform Time Sampling—Hanning Weighting

The large sidelobes of $W_U(\nu)$ are caused by the sharp drop in the sampling window at $\pm T/2$. As can be expected from Fourier theory the sidelobe levels can be reduced by smoothing the edges of the sampled time window by non-uniform weighting. Consider a time window that is tapered such that the sampling weight falls smoothly to zero at $\pm T/2$. The most widely used weighting is Hanning tapering:

$$f_H(t) = \frac{1}{2}\left[1 + \cos\left(\frac{2\pi t}{T}\right)\right] \qquad |t| \le T/2. \qquad \text{(E.3)}$$

The instrument function in the frequency domain is the Fourier transform of $f_H(t)$, which is the weighted sum of three sinc functions:

$$W_H(\nu) = \frac{1}{\Delta\nu}\mathrm{sinc}\left(\frac{2\pi\nu}{\Delta\nu}\right) + \frac{1}{2\Delta\nu}\left[\mathrm{sinc}\left(\frac{2\pi\nu}{\Delta\nu} - \pi\right) + \mathrm{sinc}\left(\frac{2\pi\nu}{\Delta\nu} + \pi\right)\right]. \qquad \text{(E.4)}$$

Again, this function is area-normalized. The FWHM for the Hanning functions is $\sim 2/T$ and equal to the sampling spacing $\Delta\nu$. The first sidelobe level is at only -2.7% of the peak. With Hanning weighting we get the expected results of much reduced sidelobes at the expense of lowered spectral resolution.

•Convolution with Instrument Functions

Model spectral lineshapes can often be approximated to high accuracy by the sum of a baseline, a slope and a Lorentzian lineshape or series of Lorentzian lineshapes. This is particularly true for planetary spectroscopy where the absorption coefficient lineshapes are dominated by collisional broadening (which is Lorentzian at moderate pressures, see Appendix C). Since it is a linear operation, the convolution of such a compound lineshape is equivalent to the sum of the convolutions of each member.

Convolution of a first order polynomial in ν (a baseline plus slope) with any even, area normalized instrument function (such as the three above) will have no effect on the polynomial. For the compound lineshape discussed above, therefore, we need general formulae for the convolution of a Lorentzian with applicable instrument functions.

Consider a Lorentzian lineshape $\eta(\nu)$ with a peak value A and FWHM of 2γ; γ may be termed the line broadening parameter, particularly when dealing with collisionally broadened lines. The approximate response of a spectrometer with normalized square (box) channels to this Lorentzian is

$$W_B(\nu) \otimes \eta(\nu) = \frac{A}{\Delta\nu} \int_{\nu-\Delta\nu/2}^{\nu+\Delta\nu/2} \frac{\gamma^2}{\gamma^2 + \nu'^2} d\nu'$$

$$= \frac{\gamma A}{\Delta\nu} \left[\tan^{-1}\left(\frac{\nu + \Delta\nu/2}{\gamma}\right) - \tan^{-1}\left(\frac{\nu + \Delta\nu/2}{\gamma}\right) \right]. \quad \text{(E.5)}$$

Here and below I am using the symbol $\otimes$ to denote the convolution of two functions. An equivalent expression, found through use of the convolution theorem (outlined below), is

$$W_B(\nu) \otimes \eta(\nu) = \gamma A \left[\tan^{-1}\left(\frac{\gamma\Delta\nu}{\gamma^2 + \nu^2 - (\Delta\nu/2)^2}\right) + s\pi \right] \quad \text{(E.6)}$$

where

$$s = \begin{cases} 0 & \text{if } \gamma^2 + \nu^2 - (\Delta\nu/2)^2 \geq 0 \\ 1 & \text{if } \gamma^2 + \nu^2 - (\Delta\nu/2)^2 < 0. \end{cases} \quad \text{(E.7)}$$

For the more complicated instrument functions, such as $W_U(\nu)$ and $W_H(\nu)$, we make fortunate use of the famous Convolution Theorem (e.g., Bracewell 1965); the Fourier transform of the convolution of two functions is equivalent to the product of the Fourier transforms of the functions:

$$\mathcal{F}\left[W_U(\nu) \otimes \eta(\nu)\right] \;=\; \mathcal{F}\left[W_U(\nu)\right] \times \mathcal{F}\left[\eta(\nu)\right]. \tag{E.8}$$

Therefore the convolution of two functions is the inverse Fourier transform of the product of the Fourier transforms of each function.

For the convolution of a Lorentzian with $W_U(\nu)$ we first recall that the Fourier transform of $W_U(\nu)$ is a uniformly sampled time window. The Fourier transform of a Lorentzian is an exponential function:

$$\mathcal{F}\left[\eta\left(\nu\right)\right] = A\int_{-\infty}^{\infty}\frac{\gamma^2}{\gamma^2+\nu^2}\,e^{-i2\pi\nu t}d\nu = 2\gamma^2 A\int_0^{\infty}\frac{\cos\left(2\pi\nu t\right)}{\gamma^2+\nu^2}d\nu = \pi\gamma A e^{-2\pi\gamma|t|}. \tag{E.9}$$

To find the convolution of the sinc with the Lorentzian, we take the inverse transform of the product of the above results, which is just the exponential limited to $|t| \leq 1/2\Delta\nu$:

$$\begin{aligned} W_U\left(\nu\right)\otimes\eta\left(\nu\right) \;&=\; \pi\gamma A\int_{-1/2\Delta\nu}^{1/2\Delta\nu} e^{-2\pi\gamma|t|}\;e^{+i2\pi\nu t}dt \\ &= 2\pi\gamma A\int_0^{1/2\Delta\nu} e^{-2\pi\gamma t}\cos\left(2\pi\nu t\right)dt \\ &= A\frac{\gamma^2}{\gamma^2+\nu^2}\left(1+\frac{e^{-\pi\gamma/\Delta\nu}}{\gamma}\left[\nu\,\sin\left(\frac{\pi\nu}{\Delta\nu}\right)\;-\;\gamma\,\cos\left(\frac{\pi\nu}{\Delta\nu}\right)\right]\right). \end{aligned} \tag{E.10}$$

In the limit that the Lorentzian is much broader than the sinc FWHM (i.e., $\pi\gamma/\Delta\nu \gg 1$) the convolution results in the initial Lorentzian as expected.

To determine the convolution of a Lorentzian with Hanning weighted channels we proceed in a similar manner. Here it is useful to introduce the function

$$\Xi(\alpha,\beta,z) \;\equiv\; \frac{\alpha^2}{\alpha^2+z^2}\left(1+\frac{e^{-\pi\alpha/\beta}}{\alpha}\left[z\,\sin\left(\frac{\pi z}{\beta}\right)\;-\;\alpha\,\cos\left(\frac{\pi z}{\beta}\right)\right]\right). \tag{E.11}$$

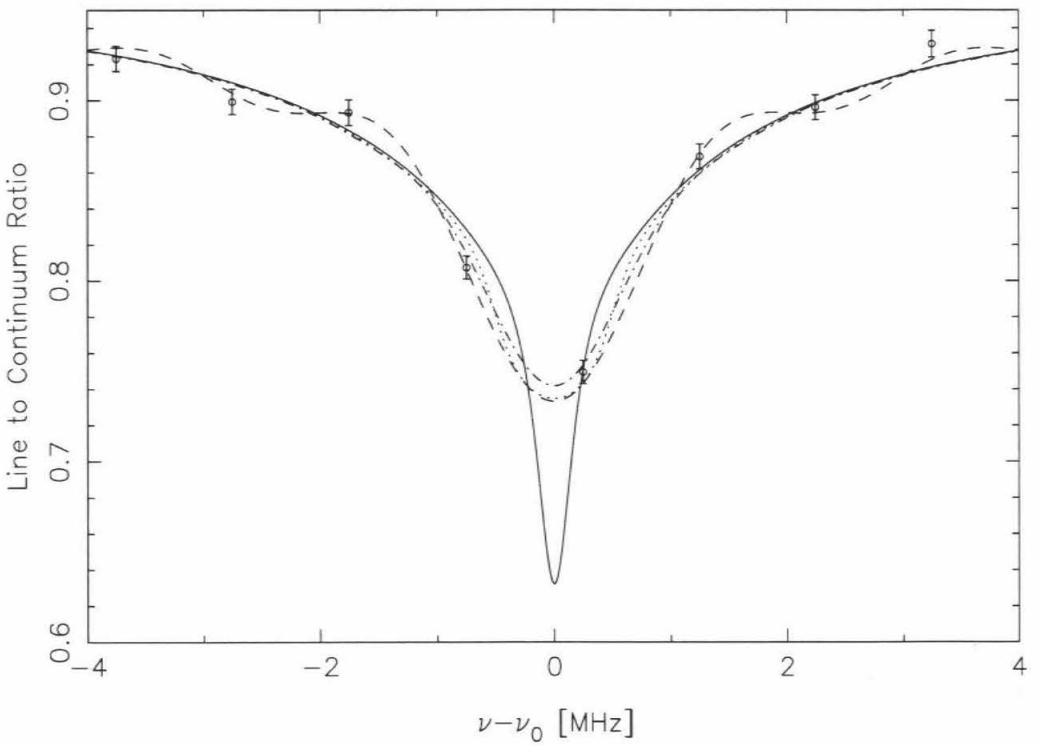

Figure E.1. Convolution of a spectral feature with box, sinc, and Hanning weighted instrument functions.

The convolution of sinc channel with a Lorentzian is then simply $A\Xi(\gamma, \Delta\nu, \nu)$. For Hanning weighted channels the convolution is

$$\begin{aligned} W_H(\nu) \otimes \eta(\nu) \; =& A\left[\frac{1}{2}\Xi\left(\gamma, \frac{\Delta\nu}{2}, \nu\right)\right. \\ &\left. + \frac{1}{4}\Xi\left(\gamma, \frac{\Delta\nu}{2}, \nu - \frac{\Delta\nu}{2}\right) \; + \; \frac{1}{4}\Xi\left(\gamma, \frac{\Delta\nu}{2}, \nu + \frac{\Delta\nu}{2}\right)\right]. \end{aligned} \tag{E.12}$$

The effects of instrument functions on the measured spectrum are particularly important for the observations of Venus reported in this work. Venus exhibits a particularly narrow line (compared to Mars, for example). A model spectral line similar to the line seen on Venus in late 1994 is presented as the solid line in Fig. E.1; the model consist of a baseline plus four Lorentzians of varying γ. Convolution of this spectrum with instrument functions of 1 MHz channel spacing are also presented: box

channels (dotted line), sinc channels (dashed line), and Hanning weighted channels (dot–dash line). The solid line is based upon measurements at 62.5 kHz resolution. Also plotted as points are the measured spectrum values at $\Delta\nu = 1$ MHz obtained simultaneously using sinc channels.

Appendix F: Line Inversion

The following is an extension of work presented in Gurwell *et al.* (1995) and Muhleman and Clancy (1993). The method used to invert spectra from the observations detailed in this work is a simple iterative constrained least-squares procedure. It can be configured to determine either an abundance profile or a temperature profile for a single observed spectrum, and for two or more spectral transitions which contain complimentary information (such ^{12}CO $J(1-0)$ and ^{12}CO $J(2-1)$ in the Venus mesosphere) can be used to determine both profiles simultaneously.

We proceed as follows. Using the geometry appropriate for the spectral line to be inverted, a model spectrum is calculated using an initial guess for the profile we wish to derive. The other profile (either temperature or mixing ratio) must be specified *a priori*. This model spectrum is subtracted from the observed spectrum, leaving a residual R_ν at each frequency. These residuals are considered to be due to differences between the model profile and the "true" profile to be retrieved, along with components of noise. Appropriate changes in the model profile will result in a model spectrum which provides a better fit to the observed data and therefore reduces the residuals.

For a stratified atmosphere, the intensity along a given raypath is described in Eq. A.11 (Appendix A). For the model atmosphere let the value of the parameter to be retrieved (either temperature or mixing ratio) in layer i be denoted by x_i; the continuous vertical profile is then approximated by the n discrete values of x which are constant within each layer. A linearized equation for each observed frequency of

the spectrum can be constructed of the form

$$R_\nu \;=\; I_\nu[obs] - I_\nu[mod] \;=\; \sum_{i=1}^{n} \frac{\partial I_\nu}{\partial x_i} \Delta x_i. \tag{F.1}$$

Here Δx_i is an estimate of the *change* in the parameter that is required to reduce the residual at that frequency to zero. The partial derivative of the discrete radiative transfer equation is presented in analytic form in Appendix B.

Obviously, the set of equations (one for each observed frequency) can be thought of in terms of a vector equation, where a vector of residuals is equal to an array of partial derivatives times a vector of best fit changes to the vector x:

$$\vec{R} \;=\; \mathbf{A}\vec{\Delta x}. \tag{F.2}$$

As long as the observed frequencies outnumber the model atmospheric layers, the system of equations is overdetermined and a least-squares minimization technique can be employed to find the best fit changes to the parameter x in each layer. Using basic matrix inversion theory,

$$\vec{\Delta x} \;=\; \left(\mathbf{A}^{\mathrm{T}}\mathbf{A}\right)^{-1}\mathbf{A}^{\mathrm{T}}\vec{R} \tag{F.3}$$

where $\mathbf{A}^{\mathrm{T}}$ is the transpose of $\mathbf{A}$.

The radiative transfer equation is very nonlinear with respect to either temperature or absorber abundance. This nonlinearity demands that any inversion of the sort presented above be iterative. An updated profile is determined from the previous profile and the best fit changes found from Eq. F.3, and a next generation model spectrum is then calculated. Residuals are then determined as outlined above, and the cycle is repeated until convergence to a best-fit solution profile is reached. Convergence may be defined in several ways, but for the current work it was defined as the point where the sum of the squares of the residuals from the current iteration differed from that of the previous iteration by no more than 1 part in 10^4, which is in

practice a very stringent convergence requirement, demanding several iterations on average to be satisfied.

The reduction of the radiative transfer equation into a set of linear equations can be highly ill-conditioned, and when observational noise is present the reduction is often mathematically improper (Chahine 1972). This becomes evident when spectra are directly inverted using Eq. F.3, particularly when the number of atmospheric layers is more than a small fraction of the number of observed frequencies. This problem can be qualitatively seen for the case where an atmospheric layer is not well sensed by the set of observed frequencies (i.e., the weighting functions for the observed line are small within that layer). The above matrix inversion technique becomes overly sensitive to noise in this case and the retrieved parameter profile can exhibit extreme fluctuations which do not represent the true atmospheric profile but do fit the observations.

The use of constraints in the inversion process can help overcome some of the inherent instability in the linearization of the radiative transfer equation. Constraints provide *a priori* information on the profile structure, and are implemented by adding equations of condition the the set of linearized residual equations. These equations of condition are often termed smoothness or continuity constraints.

For the work reported in this thesis, two continuity constraints were used depending on the particulars of the inversion. The equations of condition were either zeroth-order or first-order constraints on the smoothness of the profile. A zeroth-order constraint weights the solution profile to be a constant with altitude, or

$$x_i \approx x_{i+1} \pm \sigma, \tag{F.4}$$

where σ is some tolerance on deviation from the constraint. In an iterative matrix inversion procedure, the constraint is implemented through the addition of $n-1$ linear

equations of the form

$$\frac{x_i - x_{i+1}}{\sigma} = \frac{\Delta x_{i+1} - \Delta x_i}{\sigma}. \tag{F.5}$$

The value of the tolerance σ can in practice only be determined through trial and error. This constraint, when correctly weighted, allows for an accurate determination of the retrieved profile for the region of the atmosphere where weighting functions are significant. For regions that are not well-sensed by the observations the solution profile will tend toward a constant value.

A first-order constraint weights the first derivative of the profile with respect to altitude (i.e., its slope) to be a constant, or

$$\frac{x_{i+1} - x_i}{z_{i+1} - z_i} \approx \frac{x_i - x_{i-1}}{z_i - z_{i-1}} \pm \sigma. \tag{F.6}$$

Again, σ represents some tolerance (to be determined through trial and error). In an iterative matrix inversion procedure, the constraint is implemented through the addition of $n - 2$ linear equations of the form

$$\frac{x_{i+1} - 2x_i + x_{i-1}}{\sigma} = \frac{-\Delta x_{i+1} + 2\Delta x_i - \Delta x_{i-1}}{\sigma}, \tag{F.7}$$

where the assumption that the model atmosphere is comprised of uniformly thick layers has been made. Again, for a proper tolerance, this constraint will allow for an accurate determination of the profile in the region where weighting functions are significant.

References

ALEXANDER, M. J. 1992. A mechanism for the Venus thermospheric superrotation. *Geophys. Res. Lett.* **19**, 2207-2210.

ALEXANDER, M. J., A. I. F. STEWART, S. C. SOLOMON, AND S. W. BOUGHER 1993. Local time asymmetries in the Venus thermosphere. *J. Geophys. Res.* **98**, 10849-10871.

ALLEN, D., D. CRISP, AND V. MEADOWS 1992. Variable oxygen airglow on Venus as a probe of atmospheric dynamics. *Nature* **359**, 516-519.

AVDUESKIY, V. S., M. YA. MAROV, YU. N. KULIKOV, V. P. SHARI, A. YA. GORBACHEVSKIY, G. R. USPENSKIY, AND Z. P. CHEREMUKHINA 1983. Structure and parameters of the Venus atmosphere according to Venera probe data. in *Venus* , D. M. Hunten, L. Colin, T. M. Donahue, and V. I. Moroz, Eds., 681-765. University of Arizona Press, Tucson.

BARKER, E. S., 1972. Detection of molecular oxygen in the Martian atmosphere. *Nature* **238**, 447-448.

BARNES, J. R. 1990. Possible effects of breaking gravity waves on the circulation of the middle atmosphere of Mars. *J. Geophys. Res.* **95**, 1401-1421.

BERGE, G. L., D. O. MUHLEMAN, AND R. P. LINFIELD 1988. Very Large Array observations of Uranus at 2.0 cm. *Astron. J.* **96**, 388-395.

BETZ. A. L., M. A. JOHNSON, R. A. MCLAREN, AND E. C. SUTTON 1976. Heterodyne detection of CO_2 emission lines and wind velocities in the atmosphere of Venus. *Astrophys. J.* **208**, L141-L144.

BÉZARD, B., C. DE BERGH, B. FEGLEY, J.-P. MAILLARD, D. CRISP, T. OWEN, J. B. POLLACK, AND D. GRINSPOON 1993. The abundance of sulfur dioxide below the clouds of Venus. *Geophys. Res. Lett.* **20**, 1587-1590.

BORN, M., AND E. WOLF 1980. *Principles of Optics.* 6th ed. Pergamon Press, Oxford.

BOUGHER, S. W., R. E. DICKINSON, E. C. RIDLEY, R. G. ROBLE, A. F. NAGY, AND T. E. CRAVENS 1986. Venus mesosphere and thermosphere: II. Global circulation, temperature, and density variations. *Icarus* **68**, 284-312.

BOUGHER, S. W., R. E. DICKINSON, E. C. RIDLEY, AND R. G. ROBLE 1988. Venus mesosphere and thermosphere III. Three-dimensional general circulation with coupled dynamics and composition. *Icarus* **73**, 545-573.

BOUGHER, S. W., J. C. GERARD, A. I. STEWART, AND C. G. FESEN 1990. The Venus nitric oxide night airglow: Calculations based on the Venus thermospheric general circulation model. *J. Geophys. Res.* **95**, 6271-6285.

BOUGHER, S. W. AND W. J. BORUCKI 1994. Venus O_2 visible and IR nightglow: Implications for lower thermosphere dynamics and chemistry. *J. Geophys. Res.* **99**, 3759-3776.

BRACEWELL, R., 1965. *The Fourier Transform and Its Applications.* McGraw-Hill, New York.

BRINTON, H. C., H. A. TAYLOR, H. B. NIEMANN, AND H. G. MAYR 1979. Venus nighttime hydrogen bulge. *Bull. Amer. Astron. Soc.* **11**, 538.

CARLTON, N. P., AND W. A. TRAUB 1972. Detection of molecular oxygen on Mars. *Science* **177**, 988-992.

CHAHINE, M. T. 1972. A general relaxation method for inverse solution of the full radiative transfer equation. *J. Atmos. Sci.* **29**, 741-747.

CHANDRASEKHAR, S. 1950. *Radiative Transfer.* Oxford University Press.

CHASSEFIÈRE, D. AND M. CABANE 1991. Stratospheric depletion of CO on Titan. *Geophys. Res. Lett.* **18**, 467-470.

CLANCY, R. T., D. O. MUHLEMAN, AND B. M. JAKOSKY 1983. Variability of carbon monoxide in the Mars atmosphere. *Icarus* **55**, 282-301.

CLANCY, R. T., AND D. O. MUHLEMAN 1985a. Diurnal CO variations in the Venus mesosphere from CO microwave spectra. *Icarus* **64**, 157-182.

CLANCY, R. T., AND D. O. MUHLEMAN 1985b. Chemical-dynamical models of the Venus mesosphere based upon diurnal microwave CO variations. *Icarus* **64**, 183-204.

CLANCY, R. T., AND D. O. MUHLEMAN 1990. Corrections regarding the Lellouch *et al.* (1989) analysis of Mars atmospheric ^{12}CO and ^{13}CO spectra. *Icarus* **85**, 120-129.

CLANCY, R. T., D. O. MUHLEMAN, AND G. L. BERGE 1990. Global changes in the 0-70 km thermal structure of the Mars atmosphere derived from 1975 to 1989 microwave CO spectra. *J. Geophys. Res.* **95**, 14543-14554.

CLANCY, R. T., AND D. O. MUHLEMAN 1991. Long-term (1979-1990) changes in the thermal, dynamical and compositional structure of the Venus mesosphere as inferred from microwave spectral line observations of ^{12}CO, ^{13}CO, and $C^{18}O$. *Icarus* **89**, 129-146.

CLANCY, R. T., A. W. GROSSMAN, AND D. O. MUHLEMAN 1993. A cold, dry, cloudy, dust-free Mars atmosphere in the 1990's. *Bull. Amer. Astron. Soc.* **25**, 1060.

CLANCY, R. T., E. LELLOUCH, Y. N. BILLAWALA, B. J. SANDOR, AND D. J. RUDY 1994. Microwave observations of a 1994 Mars global dust storm. *Bull. Amer. Astron. Soc.* **26**, 1130.

COLLARD, A. D., F. W. TAYLOR, S. B. CALCUTT, R. W. CARLSON, L. W. KAMP, K. H. BAINES, TH. ENCRENAZ, P. DROSSART, E. LELLOUCH, AND B. BÉZARD 1993. Latitudinal distribution of carbon monoxide in the deep atmosphere of Venus. *Planet. Space Sci.* **41**, 487-494.

COLMONT, J. M. AND N. MONNANTEUIL 1986. Self, nitrogen and oxygen broadening of the 115 GHz line of carbon monoxide. *J. Quant. Spectrosc. Radiat. Transfer* **35**, 81-85.

CONNES, P. J. F. NOXON, W. A. TRAUB, AND N. P. CARLETON 1979. $O_2(^1\Delta)$ emission in the day and night airglow of Venus. *Astrophys. J.* **233**, L29-L32.

CORNWELL, T. J. 1989. The applications of closure phase to astronomical imaging. *Science* **245**, 263-269.

COURTIN, R. 1988. Pressure-induced absorption coefficients for radiative transfer calculations in Titan's atmosphere. *Icarus* **75**, 245-254.

DAGG, I. R., G. E. REESOR, AND J. L. URBANIAK 1975. Collision induced absorption in N_2, CO_2, and H_2 at 2.3 cm^{-1}. *Can. J. Phys.* **53**, 1764-1776.

DEL GENIO, A. D., W. ZHOU, AND T. P. EICHLER 1993. Equatorial superrotation in a slowly rotating GCM: implications for Titan and Venus. *Icarus* **101**, 1-17.

DE PATER, I., F. P. SCHLOERB, AND A. RANDOLPH 1987. High resolution obser-

vation of the J=1-0 CO line on Venus. *Bull. Amer. Astron. Soc.* **19(3)**, 846.

DE PATER, I.,, F. P. SCHLOERB, AND A. RANDOLPH 1991. Venus imaged with the Hat Creek Interferometer in the J=1-0 CO line. *Icarus* **30**, 282-298.

DICKINSON, R. E., AND E. C. RIDLEY 1975. A numerical model for the dynamics and composition of the Venusian thermosphere. *J. Atmos. Sci.* **32**, 1219-1231.

DICKINSON, R. E., AND E. C. RIDLEY 1977. Venus mesosphere and thermosphere temperature structure. II. Day-night variations. *Icarus* **30**, 163-178.

ELGERED, G. 1993. Tropospheric radio-path delay from ground-based microwave radiometry. In *Atmospheric Remote Sensing by Microwave Radiometry* , M. A. Janssen, ed., 497-533. Wiley & Sons, New York.

GIERASCH, P. J., AND R. M. GOODY 1968. A study of the thermal and dynamical structure of the Martian lower atmosphere. *Planet. Space Sci.* **16**, 615.

GILLET, V. AND E. LELLOUCH 1994. Does Mars' middle atmosphere really have a retrograde circulation near equinox?. *Bull. Amer. Astron. Soc.* **26**, 1130.

GOLDSTEIN, J. J., M. J. MUMMA, T. KOSTIUK, D. DEMING, F. ESPENAK, AND D. ZIPOY 1991. Absolute wind velocities in the lower thermosphere of Venus using infrared heterodyne spectroscopy. *Icarus* **94**, 45-63.

GOOD, J. C., AND F. P. SCHLOERB 1981. Martian CO abundance from the $J = 0 \rightarrow 1$ rotational transition: evidence for temporal variations. *Icarus* **47**, 166-172.

GROSSMAN, A. W. 1989. *Microwave Imaging of Saturn's Deep Atmosphere and Rings.* Ph.D. thesis, California Institute of Technology.

GURWELL, M. A., D. O. MUHLEMAN, K. PIERCE SHAH, G. L. BERGE, D. J. RUDY, AND A. W. GROSSMAN 1995. Observations of the CO bulge on Venus and implications for mesospheric winds. *Icarus* **115**, 141-158.

GURWELL, M. A., AND D. O. MUHLEMAN 1995. CO on Titan: Evidence for a well-mixed atmosphere. *Icarus*, in press.

HABERLE, R. M., J. B. POLLACK, J. R. BARNES, R. W. ZUREK, C. B. LEOVY, J. R. MURPHY, H. LEE, AND J. SCHAEFFER 1993. Mars atmospheric dynamics as simulated by the NASA Ames general circulation model 1. The zonal-mean circulation. *J. Geophys. Res.* **98**, 3093-3123.

Ho, W., I. A. Kaufman, and P. Thaddeus 1966. Laboratory measurement of microwave absorption in models of the atmosphere of Venus. *J. Geophys. Res.* **71**, 5091-5108.

Holton, J. R. 1992. *An Introduction to Dynamic Meteorology.* 3rd ed. Academic Press, New York.

Houghton, J. T. 1986. *The Physics of Atmospheres.* 2nd ed. Cambridge University Press, Cambridge.

Janssen, M. A. and R. L. Poynter 1981. The microwave absorption of SO_2 in the Venus atmosphere. *Icarus* **46**, 51-57.

Kakar, R. K., J. W. Waters, and W. J. Wilson 1975. Venus: microwave detection of carbon monoxide. *Science* **191**, 379-380.

Kakar, R. K., J. W. Waters, and W. J. Wilson 1977. Mars: microwave detection of carbon monoxide. *Science* **196**, 1090-1091.

Kawabata, K. D., D. L. Coffeen, J. E. Hansen, W. A. Lane, M. Sato, and L. D. Travis 1980. Cloud and haze properties from Pioneer Venus polarimetry. *J. Geophys. Res.* **85**, 8129-8140.

Keating, G. M., J. Y. Nicholson III, and L. R. Lake 1980. Venus upper atmosphere structure. *J. Geophys. Res.* **85**, 7941-7956.

Keating, G. M., and S. Bougher 1987. Neutral upper atmospheres of Venus and Mars. *Adv. Space Res.* **12**, (12)57-(12)71.

Keating, G. M., and N. C. Hsu 1993. The Venus atmospheric response to solar cycle variations. *Geophys. Res. Lett.* **20**, 2751-2754.

Kliore, A. J., and L. Mullen 1988. Solar cycle variability of upper atmosphere temperatures on Venus. *Eos Transactions* **69**, 1287.

Knollenberg, R. G., L. Travis, M. Tomasko, P. Smith, B. Ragent, L. Esposito, D. McCleese, J. Martonchik, and R. Beer 1980. The clouds of Venus: A synthesis report. *J. Geophys. Res.* **85**, 8059-8081.

Lellouch, E., M. Gèrin, F. Combes, S. Atreya, and T. Encrenaz 1989. Observations of the $J = 0 \rightarrow 1$ CO lines in the Mars atmosphere: radio detection of ^{13}CO and monitoring of ^{12}CO. *Icarus* **77**, 414-438.

LELLOUCH, E. 1990. Atmospheric models of Titan and Triton. *Ann. Geophysicae* **8**, 653-660.

LELLOUCH, E., G. PAUBERT, AND T. ENCRENAZ 1991. Mapping of CO millimeter-wave lines in Mars' atmosphere: the spatial variability of carbon monoxide on Mars. *Planet. Space Sci.* **39**, 219-224.

LELLOUCH, E., J. J. GOLDSTEIN, S. BOUGHER, B. THÉODERE, AND J. ROSENQVIST 1993. Mars' middle atmosphere circulation near equinox from microwave observations. *Bull. Amer. Astron. Soc.* **25**, 1060.

LELLOUCH, E., J. GOLDSTEIN, J. ROSENQVIST, S. BOUGHER, AND G. PAUBERT 1994. Global circulation, thermal structure, and carbon monoxide distribution in Venus' mesosphere in 1991. *Icarus* **110**, 315-339.

LEOVY, C. B. 1978. Martian meteorological variability. In *The Mars Reference Atmosphere* , A. Kliore, ed., 1-20, COSPAR, Innsbruk.

LEOVY, C. B. 1982. Martian meteorological variability. *Adv. Space Res.* **2**, 19-44.

LINDAL, G. F., G. E. WOOD, H. B. HOTZ, D. N. SWEETNAM, V. R. ESHLEMAN, AND G. L. TYLER 1983. The atmosphere of Titan: An analysis of the Voyager 1 radio occultation measurements. *Icarus* **53**, 348-363.

LUTZ, B. L., C. DE BERGH, AND T. OWEN 1983. Titan: Discovery of carbon monoxide in its atmosphere. *Science* **220**, 1374-1375.

MARTEN, A., D. GAUTIER, L. TANGUY, A. LECACHEUX, C. ROSOLEN, AND G. PAUBERT 1988. Abundance of carbon monoxide in the stratosphere of Titan from millimeter heterodyne observations. *Icarus* **76**, 558-562.

MAYR, H. G., I. HARRIS, H. B. NIEMANN, H. C. BRINTON, N. W. SPENCER, H. A. TAYLOR, JR., R. E. HARTLE, W. R. HOEGY, AND D. M. HUNTEN 1980. Dynamic properties of the thermosphere inferred from Pioneer Venus mass spectrometer measurements. *J. Geophys. Res.* **85**, 7841-7847.

MAYR, H. G., I. HARRIS, D. R. STEVENS-RAYBURN, H. B. NIEMANN, H. A. TAYLOR, JR., AND R. E. HARTLE 1985. On the diurnal variations in the temperature and composition: a three-dimensional model with superrotation. *Adv. Space Res.* **5**, 109-112.

MOREAU, D., L. W. ESPOSITO, AND G. BRASSEUR 1991. The chemical composition

of the dust-free Martian atmosphere: preliminary results of a two-dimensional model. *J. Geophys. Res.* **96**, 7933-7945.

MUHLEMAN, D. O., G. S. ORTON, AND G. L. BERGE 1979. A model of the Venus atmosphere from radio, radar and occultation observations. *Astrophys. J.* **234**, 734-745.

MUHLEMAN, D. O., G. L. BERGE, AND R. T. CLANCY 1984. Microwave measurements of carbon monoxide on Titan. *Science* **223**, 393-396.

MUHLEMAN, D. O., A. W. GROSSMAN, E. SMITH, AND G. L. BERGE 1987. *Synthetic aperture CO map of Venus.* 22nd General Assembly of URSI, Tel Aviv, Israel.

MUHLEMAN, D. O. AND G. L. BERGE 1991. Observations of Mars, Uranus, Neptune, Io, Europa, Ganymede, and Callisto at a wavelength of 2.66 mm. *Icarus* **92**, 263-272.

MUHLEMAN, D. O. AND R. T. CLANCY 1993. Retrieval of atmospheric parameters in planetary atmospheres from microwave spectroscopy. In *Atmospheric Remote Sensing by Microwave Radiometry* , M. A. Janssen, ed., 497-533. Wiley & Sons, New York.

NAIR, H., M. ALLEN, A. D. ANBAR, Y. L. YUNG, AND R. T. CLANCY 1994. A photochemical model of the Martian atmosphere. *Icarus* **111**, 124-150.

NEWMAN, M., AND C. LEOVY 1992. Maintenance of strong rotational winds in Venus' middle atmosphere by thermal tides. *Science* **257**, 647-650.

NIEMANN, H. B., W. T. KASPRZAK, A. E. HEDIN, D. M. HUNTEN, AND N. W. SPENCER 1980. Mass spectrometric measurements of the neutral gas composition of the thermosphere and exosphere of Venus. *J. Geophys. Res.* **85**, 7817-7827.

OYAMA, V. I., G. C. CARLE, F. WOELLER, J. B. POLLACK, R. T. REYNOLDS, AND R. A. CRAIG 1980. Pioneer Venus gas chromatography of the lower atmosphere of Venus. *J. Geophys. Res.* **85**, 7891-7902.

PADIN, S., S. L. SCOTT, D. P. WOODY, N. Z. SCOVILLE, T. V. SELING, R. P. FINCH, C. J. GIOVANINE, AND R. P. LAWRENCE 1991. The Owens Valley Millimeter Array. *Publ. Astron. Soc. Pacific* **103**, 461-467.

PEARSON, T. J. AND A. C. S. READHEAD 1984. Image-formation by self-calibration

in radio astronomy. *Ann. Rev. Astron. and Astrophys.* **22**, 97-130.

PERLEY, R. A., F. R. SCHWAB, AND A. H. BRIDLE, Eds. 1989. *Synthesis Imaging in Radio Astronomy.* Astronomical Society of the Pacific Conference Series, San Francisco, Vol. 6.

PICKETT, H. M., R. L. POYNTER, AND E. A. COHEN 1992. *Submillimeter, Millimeter and Microwave Spectral Line Catalog.* JPL Publication 80–23, Rev. 3.

POLLACK, J. B., D. S. COLBURN, F. M. FLASER, R. KAHN, C. E. CARLSTON, AND D. PIDEK 1979. Properties and effects of dust particles suspended in the Martian atmosphere. *J. Geophys. Res.* **84**, 2929-2946.

POLLACK, J. B., R. M. HABERLE, J. SCHAEFFER, AND H. LEE 1990. Simulations of the general circulation of the Martian atmosphere 1. Polar processes. *J. Geophys. Res.* **95**, 1447-1473.

POLLACK, J. B., R. M. HABERLE, J. R. MURPHY, J. SCHAEFFER, AND H. LEE 1993. Simulations of the general circulation of the Martian atmosphere 2. Seasonal pressure variations. *J. Geophys. Res.* **98**, 3149-3181.

PRESS, W. H., S. A. TEUKOLSKY, W. T. VETTERLING, AND B. P. FLANNERY 1992. *Numerical Recipes in FORTRAN.* 2nd edition, Cambridge University Press.

ROSENKRANZ, P. W. 1993. Absorption of microwaves by atmospheric gases. In *Atmospheric Remote Sensing by Microwave Radiometry*, M. A. Janssen, ed., 37-90. Wiley & Sons, New York.

RUDY, D. J. 1987. *Mars: High Resolution VLA Observations at Wavelengths of 2 and 6 cm and Derived Properties.* Ph.D. thesis, California Institute of Technology.

RUDY, D. J., D. O. MUHLEMAN, G. L. BERGE, B. M. JAKOSKY AND P. R. CHRISTENSEN 1987. Mars: VLA observations of the northern hemisphere and the north polar region at wavelengths of 2 and 6 cm. *Icarus* **71**, 159-177.

SAMUELSON, R. E., W. C. MAGUIRE, R. A. HANEL, V. G. KUNDE, D. E. JENNINGS, Y. L. YUNG, AND A. C. AIKIN 1983. CO_2 on Titan. *J. Geophys. Res.* **88**, 8709-8715.

SANTEE, M. 1993. *The Thermal Structure, Dust Loading, and Meridional Transport in the Martian Atmosphere During Late Southern Summer.* Ph.D. thesis, California Institute of Technology.

SANTEE, M., AND D. CRISP 1993. The thermal structure and dust loading of the Martian atmosphere during late southern summer: Mariner 9 revisited. *J. Geophys. Res.* **98**, 3261-3279.

SANTEE, M. L., AND D. CRISP 1995. Diagnostic calculations of the circulation in the Martian atmosphere. *J. Geophys. Res.* **100**, 5465-5484.

SCHLOERB, F. P., D. O. MUHLEMAN, AND G. L. BERGE 1979. An aperture synthesis study of Saturn and its rings at 3.71–cm wavelength. *Icarus* **39**, 232-250.

SCHLOERB, F. P., S. E. ROBINSON, AND W. M. IRVINE 1980. Observation of CO in the stratosphere of Venus via its J=0–1 rotational transition. *Icarus* **43**, 121-127.

SCHUBERT, G., C. COVEY, A. DEL GENIO, L. S. ELSON, G. KEATING, A. SEIFF, R. E. YOUNG, J. APT, C. C. COUNSELMAN III, A. J. KLIORE, S. S. LIMAYE, H. E. REVERCOMB, L, A. SROMOVSKY, V. E. SUOMI, F. TAYLOR, R. WOO, AND U. VON ZAHN 1980. Structure and circulation of the Venus atmosphere. *J. Geophys. Res. A* **85**, 8007-8025.

SCHUBERT, G. 1983. General circulation and the dynamical state of the Venus atmosphere. in *Venus* , D. M. Hunten, L. Colin, T. M. Donahue, and V. I. Moroz, Eds., 681-765. University of Arizona Press, Tucson.

SEIFF, A., AND D. B. KIRK 1977. Structure of the atmosphere of Mars in summer at mid-latitudes. *J. Geophys. Res.* **82**, 4364-4378.

SEIFF, A. 1978. Post-Viking models for the structure of the summer atmosphere of Mars. In *The Mars Reference Atmosphere* , A. Kliore, ed., 1-20, COSPAR, Innsbruk.

SEIFF A., D. B. KIRK, R. E. YOUNG, R. C. BLANCHARD, J. T. FINDLAY, G. M. KELLEY, AND S. C. SOMMER 1980. Measurements of the thermal structure and thermal contrasts in the atmosphere of Venus and related dynamical observations: Results from the Pioneer Venus probes. *J. Geophys. Res.* **85**, 7903-7933.

SEIFF, A., AND D. B. KIRK 1982. Structure of the Venus mesosphere and lower thermosphere from measurements during entry of the Pioneer Venus Probes. *Icarus* **49**, 49-70.

SEIFF, A. 1983. Thermal structure of the atmosphere of Venus. in *Venus* , D. M. Hunten, L. Colin, T. M. Donahue, and V. I. Moroz, Eds., 215-279. University of Arizona Press, Tucson.

SHAH, K., D. O. MUHLEMAN, AND G. L. BERGE 1991. Measurement of winds in Venus' upper mesosphere based on doppler shifts of the 2.6-mm ^{12}CO line. *Icarus* **93**, 96-121.

SHAH, K. 1992. *Interferometric Observations of the J(0,1) CO Line on Venus: Upper Mesospheric Winds and CO Abundance.* Ph.D. thesis, California Institute of Technology.

STEWART, A. I. F., AND C. A. BARTH 1979. Ultraviolet night airglow of Venus. *Science* **205**, 59-62.

STEWART, A. I. F., J.-C. GÉRARD, D. W. RUSCH, AND S. W. BOUGHER 1980. Morphology of the Venus ultraviolet night airglow. *J. Geophys. Res.* **85**, 7861-7870.

STROBEL, D. F., D. T. HALL, X. ZHU, AND M. E. SUMMERS 1993. Upper limit on Titan's atmospheric argon abundance. *Icarus* **103**, 333-336.

TAYLOR, F. W., R. BEER, M. T. CHAHINE, D. J. DINER, L. S. ELSON, R. D. HASKINS, D. J. MCCLEESE, J. V. MARTONCHIK, P. E. REICHLEY, S. P. BRADLEY, J. DEIDERFIELD, J. T. SCHOFIELD, C. B. FARMER, L. FROIDEVAUX, J. LEUNG, M. T. COFFEY, AND J. C. GILLE 1980. Structure and meteorology of the middle atmosphere of Venus: Infrared remote sensing from the Pioneer orbiter. *J. Geophys. Res.* **85**, 7963-8006.

TAYLOR, F. W., J. T. SCHOFIELD, AND P. J. VALDES 1985. Temperature structure and dynamics of the middle atmosphere of Venus. *Adv. Space Res.* **5**, 5-23.

THOMPSON, A. R., J. M. MORAN, AND G. W. SWENSON JR. 1986. *Interferometry and Synthesis in Radio Astronomy.* 1st ed. Wiley & Sons, New York.

TRAUGER, J., AND J. LUNINE 1983. Spectroscopy of molecular oxygen in the atmospheres of Venus and Mars. *Icarus* **55**, 272-281.

VARANASI, P. 1975. Measurement of line widths of CO of planetary interest at low temperatures. *J. Quant. Spectrosc. Radiat. Transfer* **15**, 191-196.

WATERS, J. W. 1976. Absorption and emission by atmospheric gases. In *Methods of*

Experimental Physics **12**, Astrophysics Part B., 142-176. Academic Press, New York.

WILSON, W. J., M. J. KLEIN, R. K. KAKAR, S. GULKIS, E. T. OLSEN, AND P. T. P. HO 1981. Venus. I. Carbon monoxide distribution and molecular-line searches. *Icarus* **45**, 624-637.

WU, S. S. C. 1979. Photogrammetric portrayal of Mars topography. *J. Geophys. Res.* **84**, 7955-7959.

YUNG, Y. L., AND W. B. DEMORE 1982. Photochemistry of the stratosphere of Venus: Implications for atmospheric evolution. *Icarus* **51**, 624-637.

YUNG, Y. L., M. ALLEN, AND J. P. PINTO 1984. Photochemistry of the atmosphere of Titan: Comparison between model and observations. *Astrophys. J. Suppl. Ser.* **55**, 465-506.

ZASOVA, L. V., V. I. MOROZ, L. W. ESPOSITO, AND C. Y. NA 1993. SO_2 in the middle atmosphere of Venus: IR measurements from Venera-15 and comparison to UV data. *Icarus* **105**, 92-109.

ZUREK, R. W., J. R. BARNES, R. M. HABERLE, J. B. POLLACK, J. E. TILLMAN, AND C. B. LEOVY 1992. Dynamics of the atmosphere of Mars. in *Mars* , H. H. Keiffer, B. M. Jakosky, C. W. Snyder, and M. S. Matthews, Eds., 835-933. University of Arizona Press, Tucson.